IACMI/R009-2022/7.6

Material Characterization for Large Scale Additive Manufacturing (AM)

Authors:

Eduardo Barocio,

Vasudha Kapre,

Pasita Pibulchinda,

Miguel Ramirez,

Alan Franc,

Jason Susnjara

Date: 5/5/2022

Final Technical Report

PA16-0349-7.6-01

Approved for Public Release.
Distribution is Unlimited.

THE COMPOSITES INSTITUTE

U.S. DEPARTMENT OF ENERGY

DOCUMENT AVAILABILITY

Reports produced after January 1, 1996, are generally available free via US Department of Energy (DOE) SciTech Connect.

Website http://www.osti.gov/scitech/

Reports produced before January 1, 1996, may be purchased by members of the public from the following source:

National Technical Information Service
5285 Port Royal Road

Springfield, VA 22161

Telephone 703-605-6000 (1-800-553-6847)

TDD 703-487-4639

Fax 703-605-6900

E-mail info@ntis.gov

Website http://www.ntis.gov/help/ordermethods.aspx

The information, data, or work presented herein was funded in part by the Office of Energy Efficiency and Renewable Energy (EERE), U.S. Department of Energy, under Award DE-EE0006926

Project acknowledgement by authors (if any).

Material Characterization for Large Scale Additive Manufacturing (AM)

Principal Investigator: Eduardo Barocio (Purdue), Alan Franc (Techmer)

Organization: Purdue University, Techmer

Address: 1105 Challenger Av. Suite 100. West Lafayette. IN 47906.

Phone: 765-479-5500

Email: ebarocio@purdue.edu

Co-authors: Alan Franc (Techmer), Vasudha Kapre (Purdue), Pasita Pibulchinda (Purdue), Miguel Ramirez (Purdue), Jason Susnjara (Thermwood).

Date Published: (May, 2022)

Prepared by:

Institute for Advanced Composites Manufacturing Innovation

Knoxville, TN 37932

Managed by Collaborative Composite Solutions, Inc.

For the

U.S. DEPARTMENT OF ENERGY

Under contract DE- EE0006926

Project Period:

(06/2019 – 11/2021)

Approved For Public Release

TABLE OF CONTENTS

1. LISTS

1.1 LIST OF ACRONYMS

EDAM – Extrusion deposition additive manufacturing

PPS – Polyphenylene sulfide

PSU – Polysulfone

PESU – Polyethersulfone

CF – Carbon fiber

CF-PPS – 50% by weight of carbon fiber reinforced Polyphenylene sulfide

CF- PSU – 25% by weight of carbon fiber reinforced Polysulfone

CF- PESU – 25% by weight of carbon fiber reinforced Polyethersulfone

WLF – Williams-Landel-Ferry

1.2 List of Figures

1.3 List of Tables

2. EXECUTIVE SUMMARY

The objective of this project was to enable prediction of residual stresses and warpage for extrusion deposition additive manufacturing (EDAM) fabricated carbon fiber thermoplastic matrix parts with three different materials systems produced by Techmer. The materials selected include Polyphenylene sulfide reinforced with 50% by weight of carbon fiber (CF-PPS), Polyethersulfone reinforced with 25% by weight of carbon fiber (CF-PESU), Polysulfone reinforced with 25% by weight of carbon fiber (CF-PSU). ADDITIVE3D© [1,2], a physics-based simulation workflow for EDAM, provided the simulation capabilities required for this project.

Simulation predictions were validated against measurements carried out during and after the printing process carried out in the CAMRI [3] and LSAM [4] systems . Predictions for temperature, degree of crystallinity and deformation were carried out for the three material systems and two different geometries. Predictions for temperature were correlated very well with the experimental measurements for the two geometries printed using the three-material systems. The crystallinity level was verified for CF-PPS. The predictions for part deformation were in good agreement with the experimental measurements. In the best-case, predictions were within 8% of the maximum displacement observed in the 3-direction whereas predictions were within 14% for the worst-case.

The adoption of this technology in commercial large-scale EDAM production processes would dramatically reduce the costs associated with producing articles by that process. Many thousands of dollars in materials, energy, and machine time could be saved by utilizing this simulation technology to develop articles rather than iterative printings to arrive at the optimal or correct design. The avoidance of a single failed print has the possibility of saving tens of thousands of dollars involved in the cost of material, machine and operators' time.

3. INTRODUCTION

The Extrusion Deposition Additive Manufacturing (EDAM) process has enabled fabricating three-dimensional geometry in the scale of meters. This manufacturing process carried out with fiber-reinforced polymers can produce tooling or molds required in conventional composite manufacturing processes, namely autoclave, compression molding, stamping, etc. Nevertheless, the anisotropy of the printed fiber reinforced polymers and the highly non-isothermal conditions developed throughout the process give rise to internal stresses. Warpage of the printed geometry or delamination are consequences of the internal stresses. Hence, analysis tools are required to aid the design for additive manufacturing and by which issues such as warpage can be mitigated.

The objective of this project is to enable prediction of residual stresses and warpage with three

different materials systems produced by Techmer. The materials selected include Polyphenylene sulfide reinforced with 50% by weight of carbon fiber (CF-PPS), Polyethersulfone reinforced with 25% by weight of carbon fiber (CF-PESU), Polysulfone reinforced and 25% by weight of carbon fiber (CF-PSU). ADDITIVE3D©, a physics-based simulation workflow for EDAM, provided the simulation capabilities required for this project [1,2]. Digital material cards required to simulate the printing process with ADDITIVE3D© were generated for each material following the experimental and virtual methods summarized in the following sections.

Part deformation and temperature history predicted with ADDITIVE3D© were validated against experimental measurements carried out for geometries printed in the LSAM system at Thermwood® and in the Composites Additive Manufacturing Research Instrument (CAMRI) at Purdue. Process simulations with CF-PSU and CF-PPS were validated with experiments carried out in the CAMRI machine whereas predictions made with the CF-PESU was validated with experiments carried in the LSAM. The validation of simulation predictions for the LSAM was limited to only one material due to the limited access to a LSAM system at the time of conducting the experimental work in this program.

The technology being developed consists of a complete system to model and predict the performance of thermoplastic composites in large scale EDAM production processes and various end use applications. The current state of large-scale EDAM involves significant trial and error in design of AM parts. There are part deformations and dimensional changes inherent in the process. These deformations and dimensional changes are largely not entirely predictable by common observations. This results in part often requiring multiple productions with slight modifications to each iteration to ultimately achieve the correct part dimensions and geometry. This trial-and-error process is highly inefficient and time and raw material consuming. The developed technology revolutionizes this process by eliminating the necessity of the iterative process by modeling and predicting the deformations and dimensional changes and thus allowing modifications to be conducted digitally before anything is printed. This technology will significantly accelerate the adoption of large-scale EDAM which has been relatively slow largely due to the unpredictability and uncertainty associated with the additive manufactured parts. A demonstrated ability to additive manufacture dimensionally correct, structurally strong, and tough parts will be invaluable to the adoption of the technology. Large scale pellet fed EDAM is of significant interest to aerospace OEM manufacturers and suppliers to produce tools such as composite curing tools and assembly jigs and fixtures. These applications require precise dimensions and geometries at either ambient temperature (assembly jigs) or elevated temperatures (composite curing tools). The developed technology provides a technical solution to efficiently design, manufacture, and utilize these tools and fixtures.

4. BACKGROUND

The polymeric materials utilized in large scale EDAM processes are typically discontinuous fiber reinforced thermoplastics with different additives and modifiers to optimize processability and end use performance. The fiber reinforcement provides numerous performance advantages over un-reinforced thermoplastics (such as improved strength and modulus in the print direction and reduced warpage and dimensional changes), but also greatly complicates the modeling of such systems. The properties of such composites are very anisotropic and are heavily dependent on the localized fiber orientation throughout the part. As such, accurate prediction of performance in the additive manufacturing process and end use applications requires a rigorous analysis system to predict and account for these very localized variations.

The EDAM process starts with pelletized feedstock material that is melted and transported in a polymer extruder and subsequently deposited on a layer-by-layer basis. While the addition of carbon fibers (CF) to a polymeric matrix enhances the elastic and thermoelastic properties parallel to the printing direction, the tensile strength transverse to the printed bead can be less than the unreinforced polymeric material. Further, the flow-induced fiber orientation also controls the thermal, mechanical, thermoelastic and thermoviscoelastic properties of the printed material. Depending on the process conditions, fibers can be dominantly oriented parallel to the printing direction, thereby enhancing properties such as thermal conductivity, coefficient of thermal expansion, elastic modulus, etc. in this direction [5]. The anisotropic properties of the printed composite and the non-isothermal nature of this process lead to residual stresses that can manifest as warpage during and after the manufacturing process of a geometry.

ADDITIVE3D© addresses the lack of predictive capability encompassing the numerous and complex physical phenomena in the EDAM process [1,2]. Figure 1 illustrates the sequentially coupled thermomechanical analysis carried out in ADDITIVE3D© to predict the temperature history, residual stresses, and deformation that develop during and after the printing process of a part. Phenomena including anisotropic heat transfer, anisotropic thermoviscoelasticity, anisotropic shrinkage, polymer crystallization and melting, fusion bonding, convective and radiative heat transfer mechanisms develop concurrently during the EDAM process. Further, the performance of the as-printed part can be investigated using ADDITIVE3D© considering effects of manufacturing such as local fiber orientation and residual stresses.

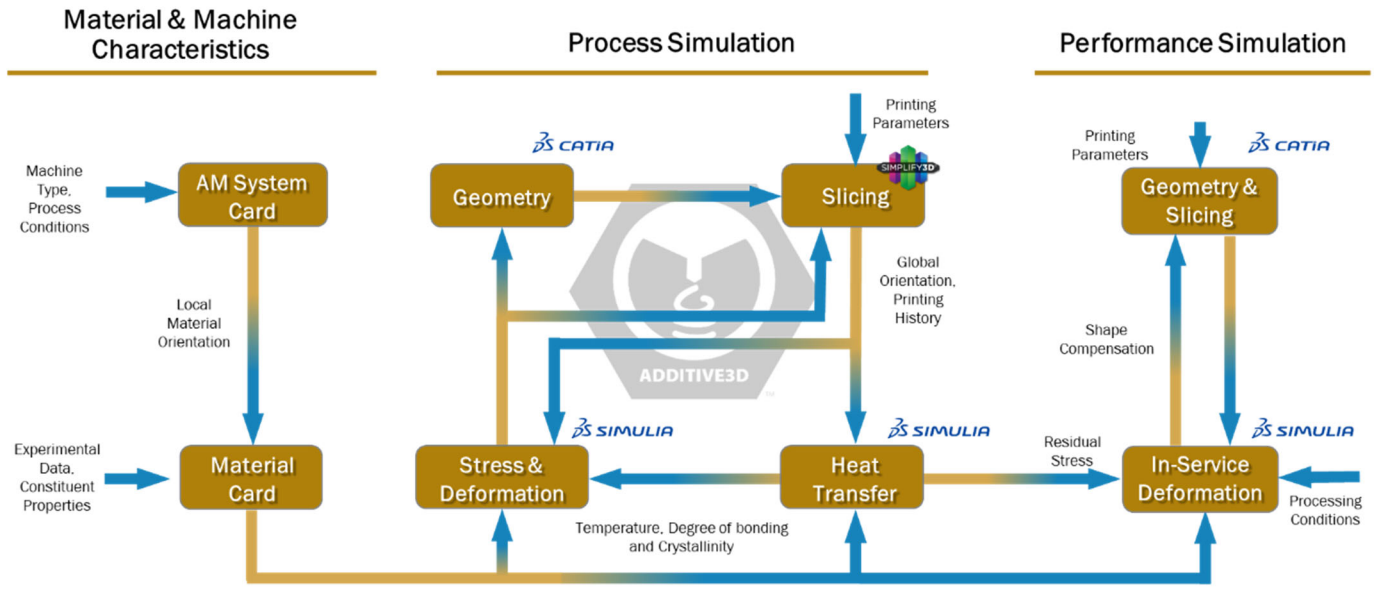

Figure 1. Flowchart of process and performance simulation in ADDITIVE3D©.

Figure 2 shows the scales considered in the EDAM process simulations. The transient EDAM process is modeled with effective properties homogenized at the scale of the printed bead in ADDITIVE3D©, thereby allowing to capture the anisotropy that results not only from the printing material but also from the printing pattern. A description of the phenomena in the EDAM process captured in the sequentially coupled thermomechanical analysis is outlined in the following section, however further details can be found elsewhere [1–3,6,7].

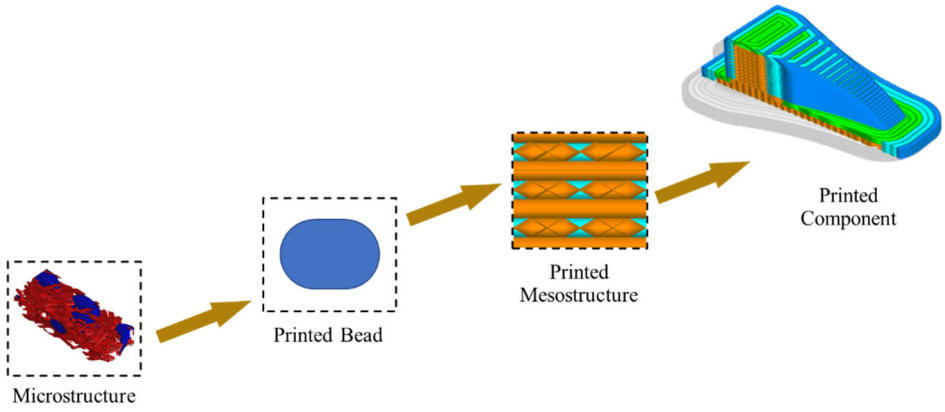

Figure 2. Length scales considered in EDAM process simulations.

Heat Transfer Analysis

Predicting the evolution of temperature in the EDAM process is of paramount importance because the properties of the polymer in the composite material are strongly influenced by temperature.

Furthermore, the temperature history controls the evolution of shrinkage and stiffness of the material. The three primary heat transfer mechanisms, namely conduction, convection, and radiation, participate in the EDAM process. Figure 3 summarizes the heat transfer mechanisms captured in ADDITIVE3D©.

The deposition process starts with the delivery of material in the molten state at the exit of the extrusion nozzle. The material is then deposited on the top of the substrate represented either by the build plate or by previously deposited material. The temperature difference between a newly deposited bead and the substrate leads to heat conduction governed by the thermal conductivity that depends on the orientation of the fibers within the bead. Temperature-dependent orthotropic heat conduction is considered in ADDITIVE3D©.

Diverse mechanisms are used in the EDAM process for compacting the extrudate during the material deposition process. Compacting the extrudate aids wetting the substrate with the molten material and closing the gap between adjacent beads. The surface of compaction mechanisms such as tampers, rollers, or smearing plates is generally actively cooled to prevent the material from sticking to the surface that is in contact with the molten material. Thermal energy is removed from the extrudate through the compacter due to heat conduction resulting from the temperature difference between the surface of the compacter and the molten material. The heat removed during compaction is captured in ADDITIVE3D© by representing the compacter as an ellipsoidal heat flow distribution that moves along with the deposition nozzle [3]. Thus, approximating the heat removed due to contact of the molten material with the relatively cooler surface of the compaction mechanism. The heat removed can be estimated from the heat carried with the fluid used for cooling the compacter.

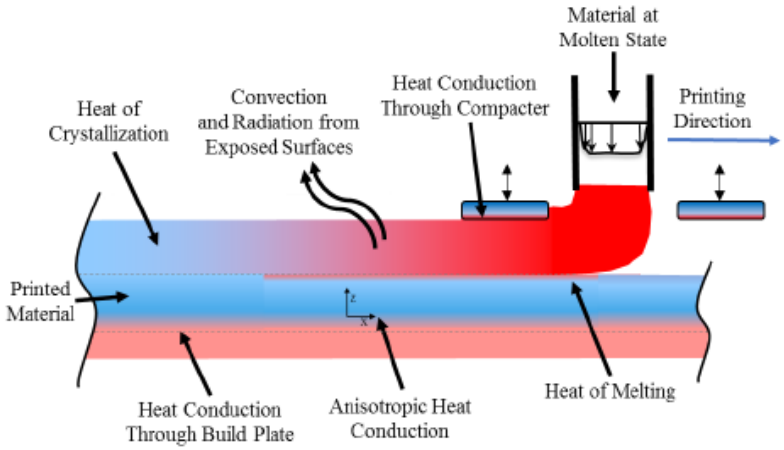

Figure 3. Heat transfer mechanisms captured in ADDITIVE3D©

In the case of printing with semi-crystalline polymers, the crystallization process of the polymer

releases thermal energy (exothermic process), which affects the temperature history. Similarly, the melting of polymer crystals that can occur upon deposition of molten material requires thermal energy. Melting and crystallization kinetics are strongly coupled with temperature in ADDITIVE3D© [3,7]. As a result, changes in the temperature history affect the crystallization history and vice versa. Figure 4 shows an example of the temperature and crystallization fields predicted with ADDITIVE3D© during the printing process of an air inlet duct geometry.

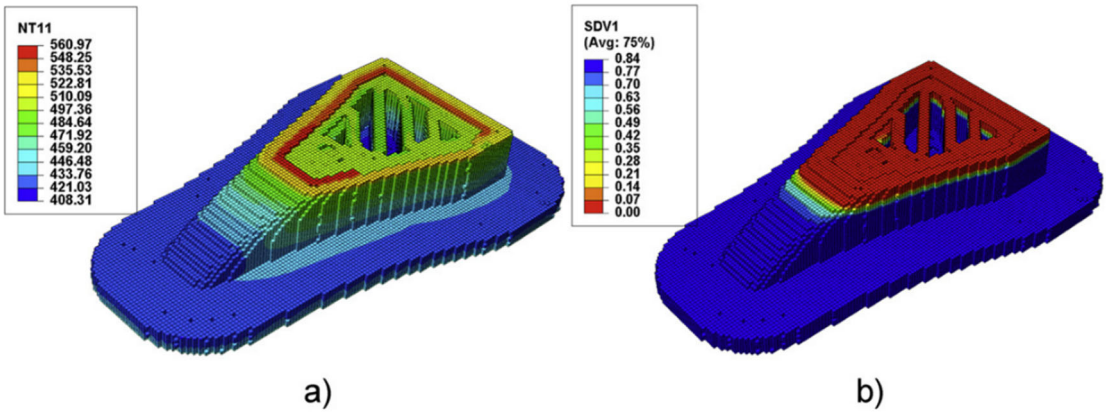

Figure 4. Simulation of the printing process of an air inlet duct geometry with ADDITIVE3D©. A) Prediction of temperature. B) Prediction of crystallinity.

Two additional mechanisms of heat transfer develop at the exposed surfaces of the deposited material. On the one hand, convection arises due to heat conduction from the hot surface of the printed material to the air surrounding the part, which in turn gives rise to local changes in air density. Buoyancy driven flow arises from these changes in density, thereby giving rise to a hydrodynamic and a thermal boundary that acts together to remove thermal energy from the surface through the movement of air. Since the convection heat transfer is highly geometry dependent, ADDITIVE3D© treats different geometric features conditions by using a set of correlation equations [3]. Finally, radiation from exposed surfaces plays an important role, especially at elevated temperatures since its contribution scales with the fourth power of the temperature at the surface. Unlike convection, radiation does not require a medium to occur since it develops from the infrared emission.

Predictions of temperature carried out with ADDITIVE3D© have been validated experimentally [1–3,6]. Figure 5 shows the Finite Element (FE) mesh of the geometry of a stringer tool used for validating the temperature predictions. An arrow in Figure 5 indicates the flat face in the geometry monitored with a thermal camera during the printing process of the part.

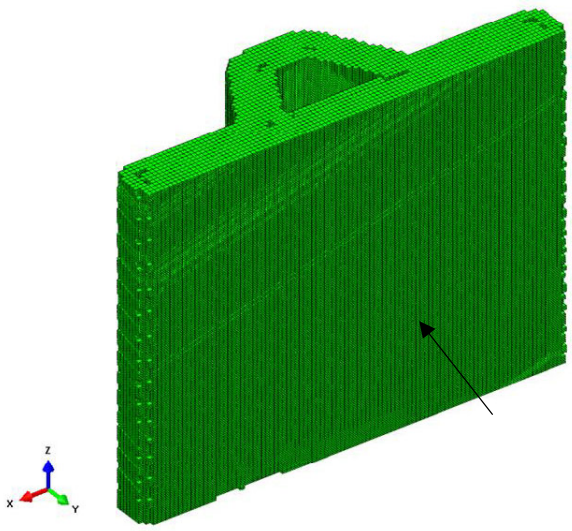

Figure 5. Finite element mesh of the geometry of a stringer tool. Arrow indicates face monitored with thermal camera during validation experiment.

Figure 6 compares the temperature field captured experimentally with the temperature field predicted with ADDITIVE3D© at the same time in the printing process. The temperature field predicted with ADDITIVE3D© is in great agreement with the experimental observations. These results were obtained utilizing material properties characterized at the scale of the bead and with the ambient radiation temperature being the only parameter calibrated.

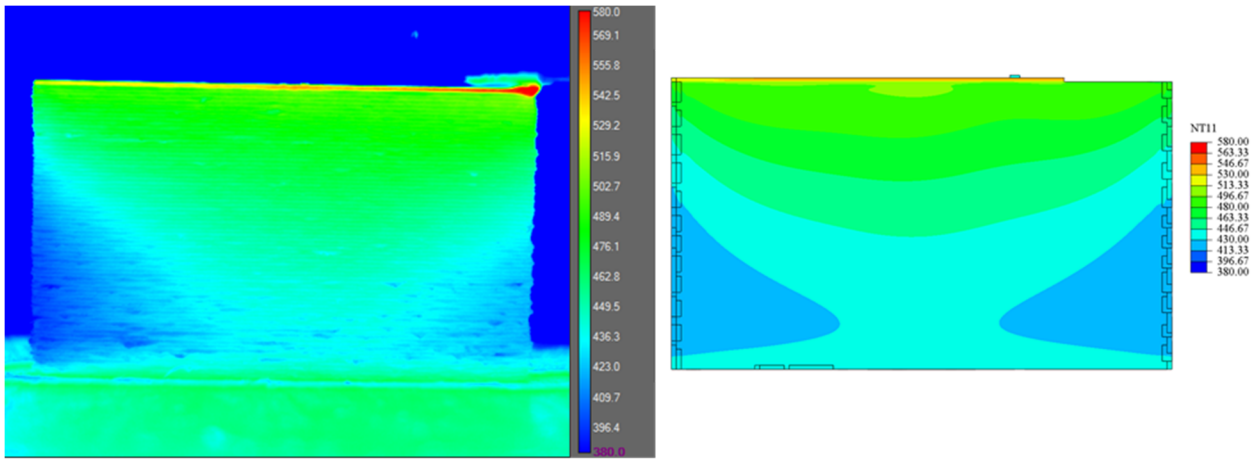

Figure 6. Temperature fields. A) Measured experimentally. B) Predicted with ADDITIVE3D©.

Stress And Deformation Analysis

The stress and deformation analysis utilizes the temperature and crystallinity predicted in the heat

transfer analysis. Internal stresses arise primarily from restraining the anisotropic shrinkage of the printed material and from temperature gradients. For example, when a new bead is deposited onto a printed substrate, which is already at a lower temperature, the printed substrate is wetted with the molten material of the newly deposited bead. As the material in the newly deposited bead begins to cool down, shrinkage is restrained by the previous bead, thereby resulting in tensile stresses in the newly deposited bead and compressive stresses in the printed substrate.

The total shrinkage of a semi-crystalline thermoplastic polymer is composed of both the thermomechanical shrinkage and the crystallization shrinkage. The thermomechanical shrinkage is governed by the coefficients of thermal expansion, which is dependent on temperature and anisotropy due to the orientation of fibers within the bead [8]. The crystallization shrinkage depends on the degree of crystallinity that forms during the cooling process and the related densification of the matrix material. Thermomechanical and crystallization shrinkage are captured in ADDITIVE3D©.

The mechanical behavior of the printed material is also anisotropic and evolves as a function of temperature and time. As the material cools down from the deposition temperature, the material undergoes multiple transitions wherein significant changes in stiffness occur. For instance, fiber-reinforced semi-crystalline polymers transition from a viscoelastic-fluid like behavior to a viscoelastic-solid like behavior upon crystallization. An additional change in the relaxation behavior occurs at the glass transition temperature of the polymer. Capturing the thermoviscoelastic behavior of the fiber-reinforced polymer is paramount to predict residual stresses and deformation. ADDITIVE3D© utilizes an orthotropic thermoviscoelastic material formulation for describing the evolution of stiffness with temperature and time for fiber reinforced amorphous and semi-crystalline polymers [7,9].

An example of a geometry utilized for validating prediction of deformation made with ADDITIVE3D© is shown in Figure 7. The square plate was printed with four layers: the first two oriented at 0° and the last two oriented at 90°. The deformation of the plate is governed by the residual stresses developed due to temperature gradients and the anisotropy of the printed material. A comparison of the deformation measured experimentally with a laser scanner and the deformation predicted with ADDITIVE3D© was carried out.

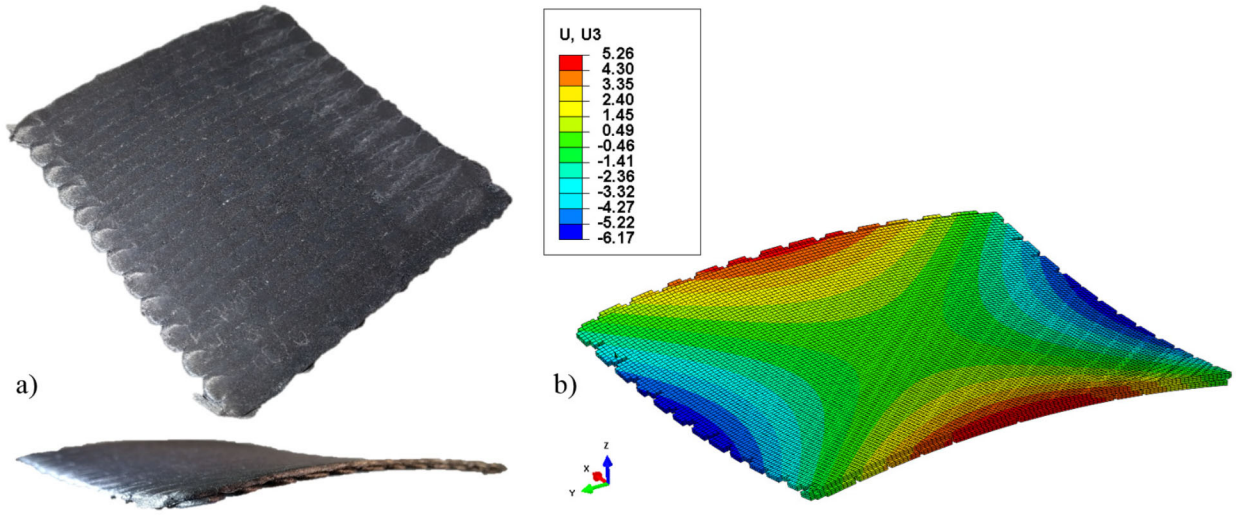

Figure 7. Validation utilizing cross-ply plate. A) Anticlastic deformation developed at the end of the printing process. B) Anticlastic deformation predicted with ADDITIVE3D© at the end of the printing process.

The deformation along lines located in the middle of the plane and in the X-direction and Y-direction was extracted from experimental measurements and from predictions made with ADDITIVE3D©. Figure 8 compares the deformation in the X and Y directions. The great agreement between the predicted and measured deformations serve to validate the predictions made with ADDITIVE3D©.

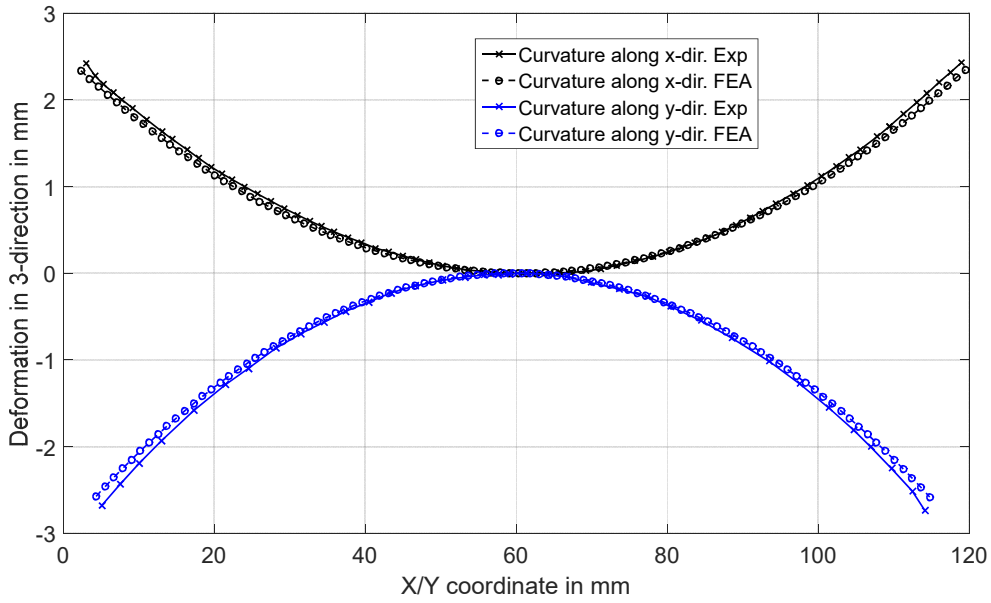

Figure 8. Comparison of deformation measured experimentally and predicted with ADDITIVE3D© for the cross-ply printed plate.

Characterization of Printed Materials

The generation of digital material cards involves extensive experimental and virtual characterization of the printed material for a set of fixed printing conditions, namely nozzle dimensions, bead-to-nozzle area ratio, and bead aspect ratio. Table 1 lists the material properties characterized for each material system, relevant ASTM standards, and type of method used to characterize the material properties.

Table 1. Summary of material properties and descriptors required for generating digital material cards.

Material Property	Relevant Standard	Method
Glass Transition Temperature	ASTM D7028	Experimental
Fiber Orientation Distribution		Virtual
Fiber Length Distribution		Experimental
Elastic Properties (9 components)	ASTM D3039 ASTM D5379	Experimental / Virtual
Coefficient of Thermal Expansion (3 directions)	ASTM E831	Experimental
Crystallization Kinetics and Melting		Experimental
Thermoviscoelastic Behavior (9 Prony series)	ASTM D5023	Experimental / Virtual
Thermal Conductivity (3 directions)	ASTM E1461	Experimental
Heat Capacity	ASTM E1269	Experimental

Experimental Methods

This section presents an overview of the experimental methods listed in Table 1 and results of the experimental characterization are presented for each material in the following sections

Glass Transition Temperature

The glass transition temperature T_g defines the transition from the "glassy" state to a rubbery state in amorphous polymer which at the molecular scale is related to the recovery of flexibility of the

polymer chains. The T_g is dependent upon the physical property measured, the type of measuring apparatus, and the experimental parameters used. Typical methods for measuring T_g include Dynamic Mechanical Analyzer (DMA) and Differential Scanning Calorimetry (DSC). The method adopted herein was DMA and was conducted according to the ASTM D7028 standard [10] which recommends a heating rate of $5\ ° \frac{C}{min}$ and an oscillation frequency of 1 Hz. A DMA model Q800 from TA Instruments© equipped with a dual cantilever fixture was employed in the characterization of the T_g of the printed materials. Figure 9 shows the specimen and the dual cantilever fixture in the DMA.

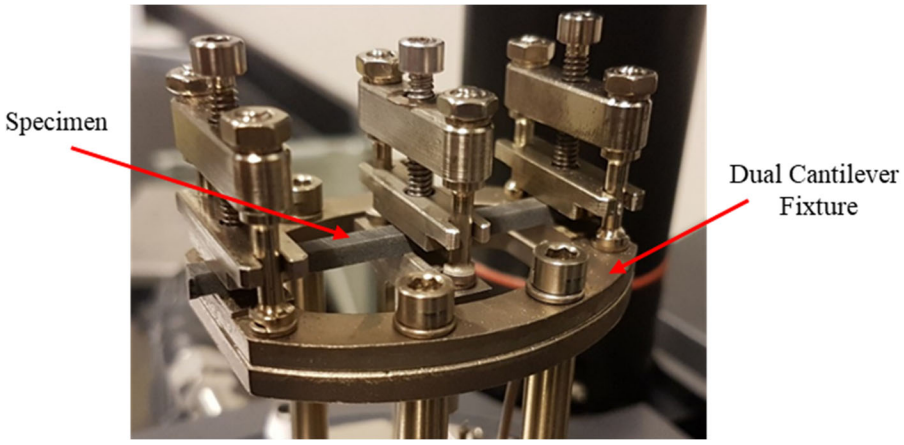

Figure 9. Experimental setup for measuring T_g via Dynamic Mechanical Analysis.

The T_g is determined from the point where a significant drop in storage modulus, E' begins which is determined from the intersection of two tangent lines. The first tangent line is constructed at temperatures before the transition whereas the second tangent line is constructed at the inflection point to approximately the midpoint of the storage modulus drop [10]. Figure 10 shows an example of the storage and loss moduli characterized through DMA and the intersection between tangent lines that defines the T_g (indicated as $188.1\ °C$).

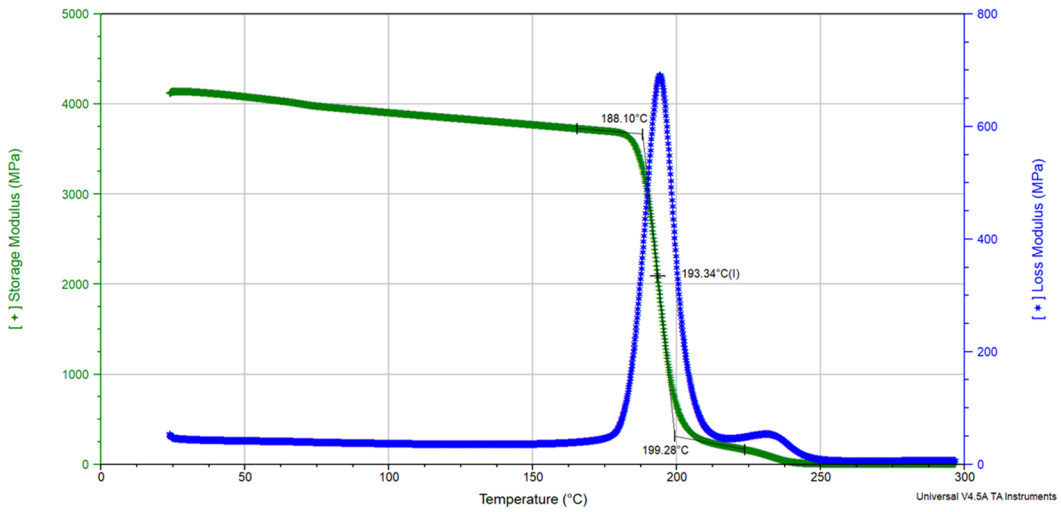

Figure 10. Determination of T_g from storage modulus characterized with DMA.

Fiber Length Distribution

The fiber length distribution is microstructural descriptor required for the virtual characterization of the printed material through micromechanics techniques. The fiber length in compounded materials can vary from the pellet to the extrudate that exits the printing nozzle due to fiber attrition caused by fiber to fiber interactions as well as by interactions of the fibers with the processing equipment [11]. Therefore, the fiber length is measured from pieces of material printed with a specific EDAM system. The following steps were followed to characterize the fiber length distribution. First, a sample of printed material is pyrolyzed at a temperature of around $700\ °C$ and for four hours. Second, the residue of the pyrolysis process containing fibers predominantly is collected and deposited on the surface of a glass slide. Subsequently, the fibers are dispersed on the surface of the glass slide with the aid of a drop of silicon oil. Third, a glass cover is placed on top of the glass slide and the glass slide is scanned under a microscope. Figure 11 shows schematically the setup described above for measuring the fiber length distribution. A mosaic of images was collected with a LEICA® DMI 5000 M optical microscope equipped with a motorized sample station. A single image is constructed from the mosaic of images and around 1000 fibers are measured with the aid of the software ImageJ. To avoid biasing the fiber length measurements, regions of interest wherein all the fibers are measured are randomly selected.

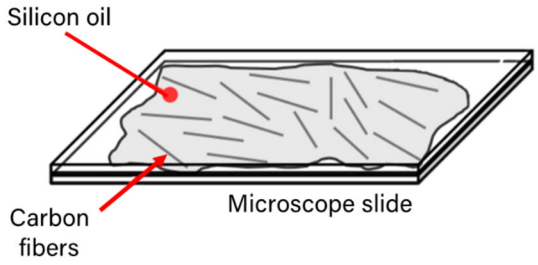

Figure 11. Schematic representation of the setup used for characterizing the fiber length distribution.

Tensile Properties

The in-plane tensile properties were characterized according to the D638 ASTM Standard Test Method for Tensile Properties of Polymer Matrix Composite Materials [12] . A Mechanical Test System (MTS) load frame with a 98 kN capacity was used to perform the corresponding experiments. To perform a test, the MTS frames are calibrated to fit the specimen height and establish the zero-displacement position. Then, a specimen is clamped to the top frame through a couple of hydraulic wedge grips. Care is taken to make the specimen is vertical in the frame. The gripping zone of the specimen is a crucial aspect to consider while performing a tensile test. The corresponding gripping zones borders (the zone where the material is clamped) are 1" away from the end of the specimen which corresponds to a distance of 6.6 mm away from the transition of the dog bone-shaped coupons.

A stereo camera Digital Image Correlation (DIC) system is used to capture photographs of the specimen during testing at a rate of 4 Hertz (each 250 milliseconds). The DIC was performed using a two-camera setup (5-megapixel cameras/17 mm lenses) with the VICSnap and VIC 3D software from Correlated solutions. The specimen is illuminated using set of lights to better focus the speckled pattern on the specimen and care is taken not to overexpose the region of interest. The DIC setup is calibrated to better adjust the focus, aperture, and exposure. Hydraulic friction wedges were used to grip the ends of the specimen.

Once the DIC systems is calibrated and the specimen mounted, the MTS lower load frame is programmed to move downwards at a displacement rate of 1 millimeter per minute, while the upper frame remains static. This induces a tension state on the specimen, and the load experienced is recorded by the load cell located in the upper frame. After the sample failure, the load and displacement analog data is stored along with the captures from the DIC to be further analyzed. Finally, the broken sample is taken out of the frames, the load frame is set to the zero-displacement position, and a new sample is placed ready to be tested. The test setup is shown in Figure 12.

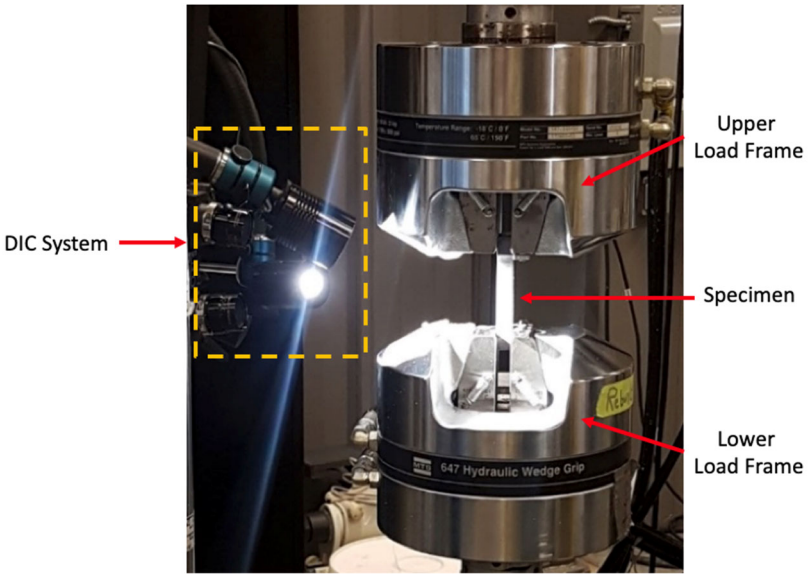

Figure 12. Experimental setup for the tensile test.

The experimental outputs from the tensile test are the load, displacement and images of the specimen during the experiment. From these data collected, it is possible to determine two mechanical properties of the material under testing, the Modulus of Elasticity (E) (a.k.a. Young's Modulus) in the load direction, and the Poisson's Ratio (ν) of the plane exposed to the DIC system. In order to compute these two mechanical properties, it is essential to extract the strain field evolution from the pictures captured with the DIC system.

A stress-strain plot can be obtained from the data. The stress is computed by dividing the force captured with the load cell over the cross-sectional area of the specimen under analysis. The strain is obtained from the data reduction process using the pictures taken with the DIC system. It is important to mention that the stress and the strain plotted are in the load direction. The Young's Modulus can be obtained from the slope of the linear portion of the stress-strain plot obtained

Further, the Poisson's ratio can be computed as shown in Equation (1)

$$\nu = -\frac{\Delta\epsilon_t}{\Delta\epsilon_l} \tag{1}$$

Where, ϵ_t is the strain transverse to the load direction, and ϵ_l is the strain in the load direction. To extract the strains from the test, a region of interest (ROI) is selected on the specimen surface. During the data reduction process, it was noticed that the ROI used considerably influences the Poisson's ratio calculation. A brief analysis was carried out considered two different ROIs of the same tensile test. The first ROI was set to considered almost all of the specimen surface exposed

to the camera, as shown in Figure 13-a). On the other hand, the second ROI was set to be just at the middle portion of the specimen, about one width distance apart from the gripping transitions, as shown in Figure 13-b). In order to get consistent results, it is essential to making sure the ROI selected represents a mean value for uncertainty (σ) below 0.008. This value indicates how accurate the strain computations are from the true value and can be modified by selecting different subset sizes or different ROIs.

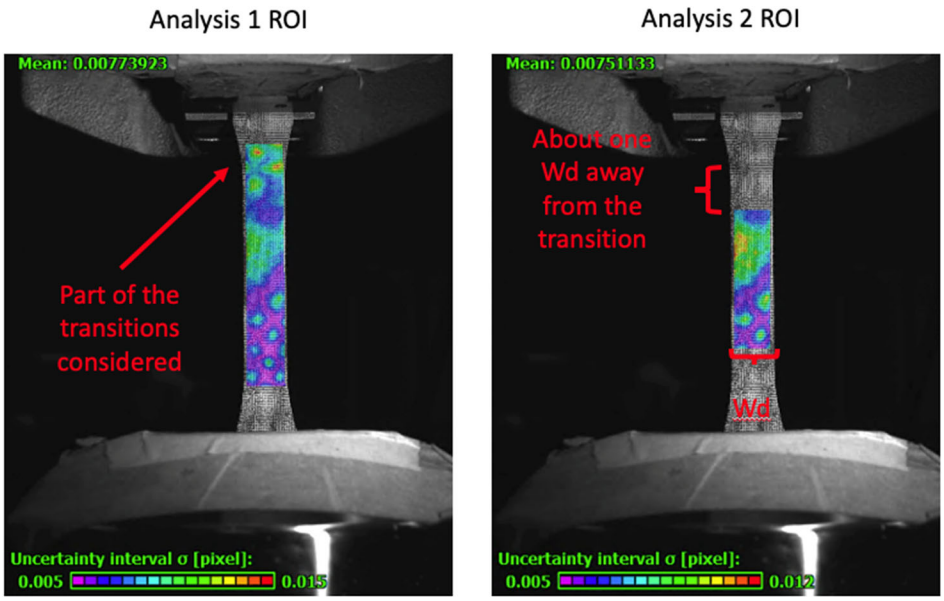

Figure 13. a) ROI considering the whole surface of the specimen. b) ROI considering only the middle portion of the coupon.

From this simple analysis, was determined that the Poisson's ratio computation is sensitive to the ROI selected. Inspection of the strain fields shown in Figure 14, reveals the non-uniformity of the transverse strains around the transition areas (compared with the center of the specimen). These lateral strains, if considered, can create bias on the Poisson's ratio computation; therefore, this ROI is not ideal for analysis, and the ROI that contains only the middle portion of the specimen is a better option. Also, it is important to point that due to the heterogeneous nature of the composite material, some non-uniformity in the strain field is expected.

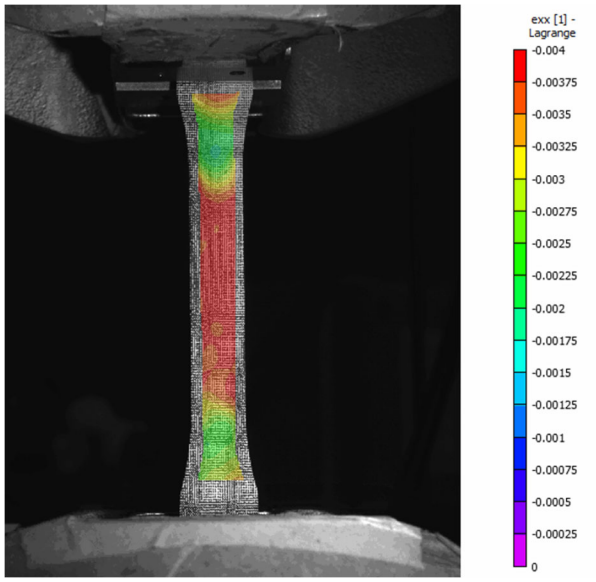

Figure 14. Strain field developed in a dog bone-shaped coupon under a tensile test.

Shear Properties

The in-plane shear properties are characterized according to the D5379 Standard Test Method for Shear Properties of Composite Materials by the V-Notched Beam Method [13]. Following this standard procedure, it is possible to obtain the shear properties of a material by loading a V-notch coupon under asymmetric flexure conditions. The specimen needs to be placed on a special fixture by aligning the central notch along the loading line using a reference tool incorporated in the fixture. The fixture was mounted on an MTS load frame with a 5-kips capacity that is in charge of compressing the two halves of the fixture while a load cell monitors the force developed. The illustration of the Iosipescu fixture from Wyoming Test Fixture Inc. is shown in Figure 15. The specimens were loaded at a rate of 1 millimeter per minute, while the load values were recorded by the 5 kilo-Newtons loadcell.

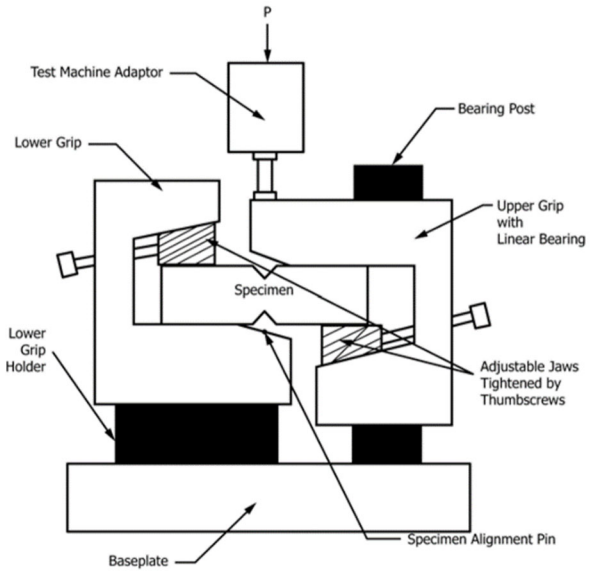

Figure 15. Iosipescu shear fixture.

Similar to the tensile test, a DIC system is used to capture pictures of the specimen under testing at rate of four images per second (4 Hz.). The focus, aperture, and exposure of the cameras need to be calibrated to adjust to the light environment. A set of pictures of the calibration instrument around the area where the specimens will be located are taken in order to calibrate the Vic-3D software. Once the DIC is calibrated and setup, a sample is mounted and tested. After that, the sample is removed, the frames are set to the zero-displacement positions and a new sample is tested. The experimental setup for the shear test is shown in Figure 16.

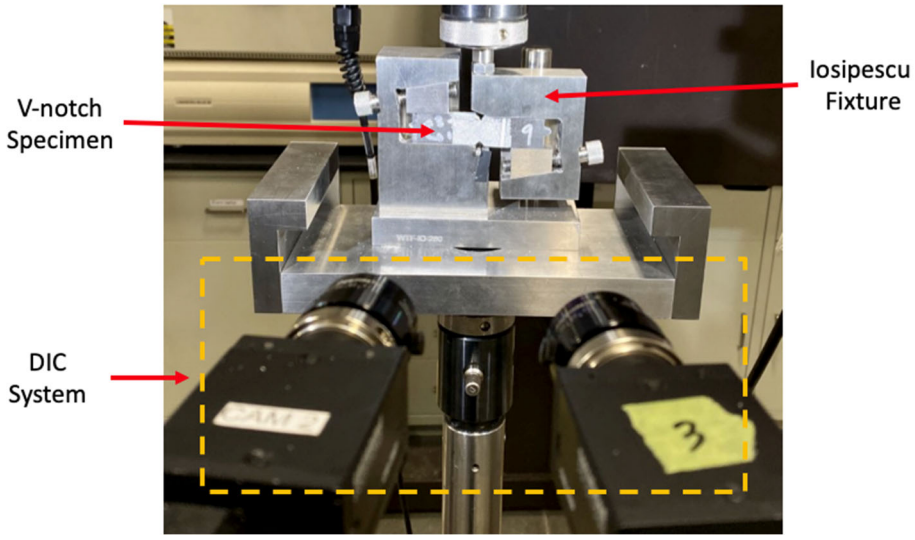

Figure 16. Iosipescu shear test experimental setup.

The experimental outputs from the shear test are the load, displacement, and images of the specimen change during the experiment. From the data collected it is possible to determine the shear modulus (G) in the sample plane exposed to the DIC system. In order to compute the value of the shear modulus, it is crucial to obtain the shear strain field evolution from the pictures captured with the DIC system.

A stress-strain plot can be obtained from the data. The stress is computed by dividing the force captured with the load cell over the cross-sectional area of the specimen at the notch location. The strain is obtained from the data reduction process using the pictures taken with the DIC system. The shear modulus can be obtained from the slope of the linear portion of the shear stress-shear strain plot obtained. To reduce to strain data, the pictures taken with the DIC system are uploaded to the Vic-3D software. Next, a region of interest (ROI) is selected on the specimen surface. For the case of the V-notch specimens, only the region within the notches are considered to extract the shear strain, as shown in Figure 17. It is essential to making sure the ROI selected represents a mean value for uncertainty (σ) below 0.008. This value indicates how accurate the strain computations are from the actual value and can be modified by selecting different subset sizes.

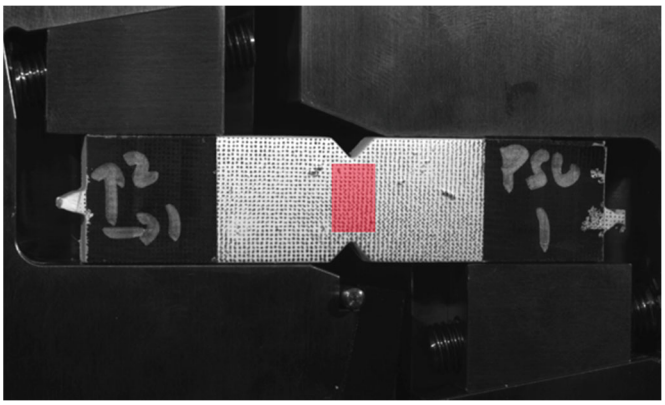

Figure 17. ROI considered for the shear test data reduction.

Thermo-mechanical Properties

The Coefficient of Thermal Expansion (CTE) is a thermo-mechanical property that depends on the local orientation of fibers within the specimen. Thus, the CTE is characterized for the three material directions and from specimens with a representative microstructure of the bead. The method used for characterizing the CTE utilizes the Digital Image Correlation (DIC) technique to capture the thermal strain that develops as the specimen is heated or cooled. A DIC setup consisting of one camera and the VIC-2D software from Correlated Solutions Inc. (Irmo, SC. USA) was used for characterizing thermal strains.

Figure 18 shows the test setup consisting of the heated stage, a light source, and a camera. The

position, focus, aperture, and exposure of the camera are adjusted to minimize the measurements uncertainty provided by the DIC software. The temperature history of the specimen was programmed in the controller of the heated stage fabricated by INSTEC (Builder, Co. USA). The specimens used for characterizing the CTE consist of plates with dimensions of about 30 by 30 mm and with thickness between 2.5 and 4 mm. A speckle pattern is spray painted on one side of the specimen to allow resolving for the thermal strains with the DIC. The specimen is placed inside a heated stage equipped with a glass window. Figure 19 shows an example of a specimen inside the heated stage without the upper cover installed.

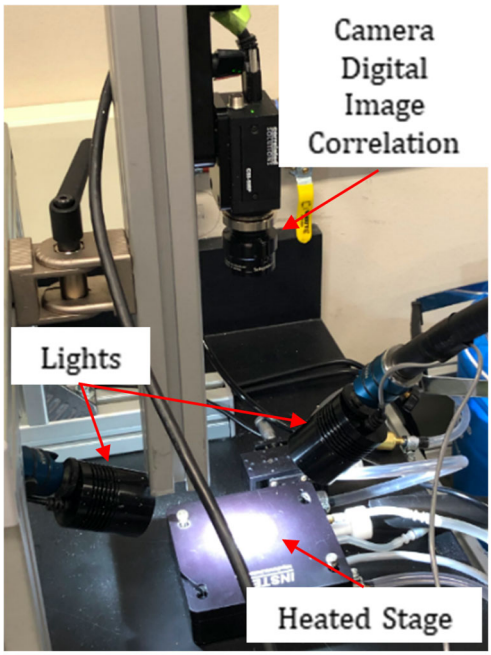

Figure 18. CTE experimental setup.

The temperature history for characterizing the CTE depends on the material, however, a typical temperature history consists of the following steps. First, the specimen is heated at a rate of 2 °C/min from the ambient temperature to the target upper temperature. Second, the specimen is held isothermal for 15 minutes. Third, the specimen is cooled down to the ambient temperature at a rate of 2 °C/min. Images are captured with the DIC camera every five seconds throughout the duration of the experiment. Upon completion of the temperature history, the images are post-processed with the software VIC-2D to resolve the strain in the two orthogonal directions of the sample. The strain is resolved for an user defined region of interest as shown in Figure 20. The temperature history collected by the INSTEC controller is combined with the thermal strains to generate a plot of strain as a function of temperature.

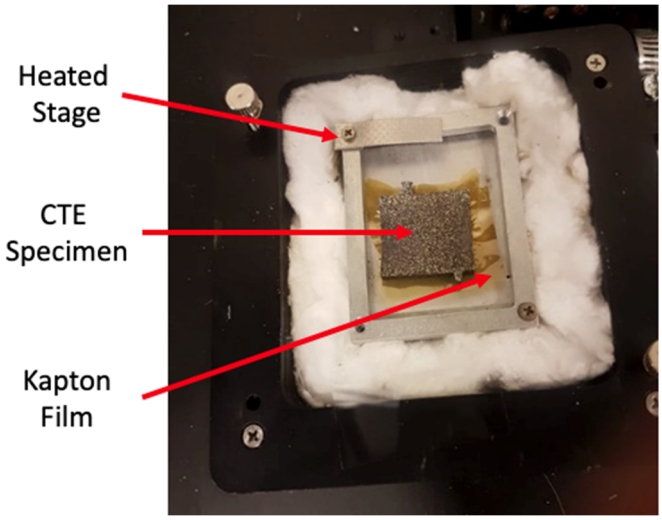

Figure 19. Specimen placed inside heated stage without the top cover installed.

The CTE denoted by α can be computed from the change in the thermal strain with respect to the temperature as shown in Equation (2). Continuous linear, quadratic, or higher order functions may be used to fit the thermal strain as a function of temperature. Thus, the CTE can be described as a continuous function of temperature by computing the first derivative of the strain function with respect to temperature.

$$\alpha = \frac{\Delta\varepsilon}{\Delta T} \tag{2}$$

The post-processing of the strain obtained from VIC-2D and the temperature history recorded by the INSTEC controller is carried out automatically through scripts implemented MATLAB©.

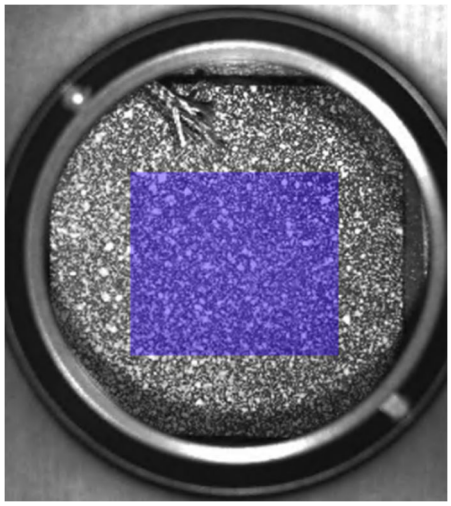

Figure 20. Region of interest (ROI) used in CTE experiment.

Melting and Crystallization Kinetics

The kinetics of the crystallization and melting process of semi-crystalline polymers is characterized via Differential Scanning Calorimeter (DSC) experiments. The kinetics of this reversible transformation is paramount for describing the behavior of fiber reinforced semi-crystalline polymers, e.g., CF-PPS, since crystallinity controls solidification, releases thermal energy, and gives rise to shrinkage. The crystallization and melting kinetics are modeled with phenomenological models that provide the evolution of the degree of crystallinity X as a function of time and temperature. The transition from melting to crystallization and vice versa is defined by the onset temperature of melting.

Polymer Crystallization

Crystallization is a physical transformation that occurs while the polymer is cooled from the melt to room temperature and consists of two processes: crystal nucleation and crystal growth. The former is a prerequisite for the latter. During this transformation, polymer chains are ordered into crystalline structures developed based on the cooling conditions. A penalty in entropy and enthalpy occurs due to the ordering of polymer chains in a crystalline structure which is manifested as shrinkage and release of thermal energy. Homogenous and heterogeneous nucleation occurs in semi-crystalline polymer after overcoming a free energy barrier. While in the former case nuclei develop in the bulk of a supercooled polymer, in the latter case nucleation occurs on the surface of impurities or heterogeneities such as carbon fiber [14,15].

To model the evolution of crystallinity in simulations of the EDAM process, a phenomenological model developed by Velisaris and Seferis [16] that captures changes in kinetics due to different crystallization mechanisms was implemented. The kinetics of each mechanism is considered through a function, $F_{c_i}, i = 1,2$, and the contribution of each mechanism to the overall crystallization rate is weighted by the factors, $w_i, i = 1,2$, as given by Equation (3). The product of the weighted sum of the two crystallization mechanisms and the maximum degree of crystallinity X_{vc_∞} yields the degree of crystallinity.

$$X(T) = X_\infty\left(w_1 F_{c_1} + w_2 F_{c_2}\right) \tag{3}$$

The weight factors satisfy the condition that their sum is always equal to unity. Each function F_{vc_i} describing a crystallization mechanism contributing to the crystallization rate is described by the integral expression given by Equation (4)

$$F_{c_i} = 1 - \exp\left\{-C_{1_i} \int_0^t \cdot exp\left[\frac{-C_{2_i}}{\left(T - T_g + T_{c_i}\right)} - \frac{C_{3_i}}{\left(T\left(T_{m_i} - T\right)^2\right)}\right] n_i \tau^{n_i - 1} d\tau\right\} \quad (4)$$

$$i = 1,2$$

where the parameters C_{1_i} capture the temperature dependence on the crystallization rate, and C_{2_i} describe the temperature dependence on the crystal growth for each mechanism. Similarly, C_{3_i} is related to the enthalpy of nucleation in each mechanism. The temperatures T, T_g, T_{c_i} and T_{m_i} used in this model represent the temperature of the process, the glass transition temperature of the polymer, the melting temperature of the polymer, and an empirically determined temperature limiting the diffusion term in Equation (4), respectively. n_i is the Avrami coefficient of each of the crystallization mechanisms characterized from isothermal crystallization experiments.

To characterize the crystallization kinetics, isothermal and non-isothermal crystallization experiments were carried out in the DSC. The degree of crystallinity X is resolved from the ratio between the thermal energy release during crystallization calculated by integrating the heat flow $\dot{Q}$ from the time where crystallization starts ($t = 0$) to a point in time t ($\int_0^t \dot{Q}(\tau)d\tau$) to the latent heat of crystallization of the fully crystallized polymer H_c^∞ as given by Equation (5).

$$X(t) = \frac{\int_0^t \dot{Q}(\tau)d\tau}{H_c^\infty} \quad (5)$$

Isothermal crystallization experiments involved the following steps: First, the sample is heated and held for five to ten minutes at the recommended material processing temperature to ensure melting of the polymer crystals in the sample. Second, the sample is quenched to a constant predefined temperature and monitored at the same temperature while crystallinity develops. Temperatures for isothermal crystallization experiments are determined from the crystallization kinetics developed during a non-isothermal experiment at a relatively low cooling rate, e.g., 3 $°\frac{C}{min}$s. As a general recommendation for conducting this type of DSC experiments, samples should be consistent within ± 0.5 mg to lessen the effect of variations in thermal mass C_{th} on the response of the PID temperature controller of the DSC ($C_{th} = mC_p$). Furthermore, baseline experiments are recommended for decoupling the sensitive heat from the latent heat. Baseline experiments can be performed with samples of an inert material with a similar thermal mass to polymer samples. Avrami coefficients are extracted from the Avrami plots for two distinct crystallization mechanisms as described in greater detail elsewhere [7,14]. Figure 21 shows an example of the heat flow measured in an isothermal DSC crystallization experiment. Referring to the same figure,

the blue line corresponds to the programmed temperature history whereas the green line corresponds to the heat flow released or absorbed by a polymer sample as it follows the programmed temperature history. Notice that positive heat flow indicates an exothermic process while negative indicates an endothermic process. The peak highlighted with a red circle in Figure 21 corresponds to the heat released during the crystallization of the polymer sample under isothermal conditions.

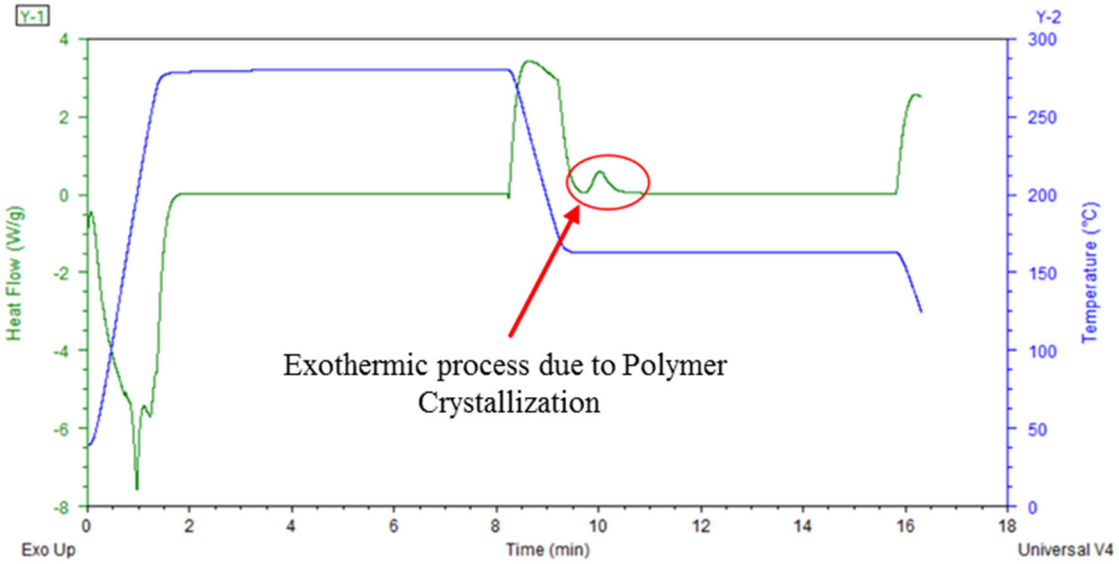

Figure 21. Example of isothermal DSC experiment for a semi-crystalline polymer.

Non-isothermal crystallization experiments are carried out at cooling rates relevant to the cooling conditions experienced by the material in the EDAM process. This includes cooling rates between 10 $°C/min$ and at least 150 $°C/min$. Cooling rates of up to 150 $°C/min$ can be achieved in a liquid nitrogen cooled DSC instruments for the temperature range where crystallization occurs. The general procedure for the non-isothermal DSC experiments consist of the following steps. First, the sample is heated to the processing temperature at a constant heating rate, and it is held under isothermal conditions to ensure complete melting of polymer crystals. Second, the sample is cooled at a cooling rate while the heat flow is recorded. The cooling rate may vary as a function of temperature depending on cooling capacity of the DSC instrument; however, the temperature range over which crystallization occurs should be considered only. The same procedure for heating and cooling can be repeated to create a second data set that can serve to extract data of the melting behavior. Figure 22 shows and example of a non-isothermal DSC experiment and indicates the exothermic and endothermic processes at crystallization and melting, respectively.

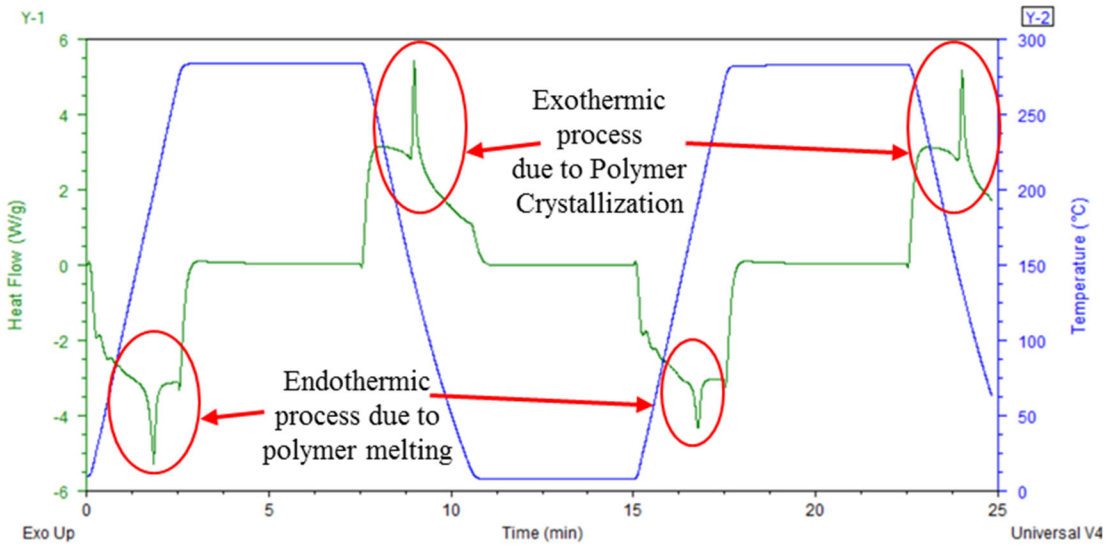

Figure 22. Example of non-isothermal DSC experiment for a semi-crystalline polymer.

Similar to the isothermal crystallization experiments, the evolution of the degree of crystallinity is computed as given by Equation (5). Figure 23 shows an example of the evolution of the degree of crystallinity characterized at different cooling rates for a semi-crystalline polymer. This example also shows the dependence of the maximum degree of crystallinity attained on the cooling rate wherein the higher the cooling rate the lower degree of crystallinity attained. The degree of crystallinity computed from the non-isothermal crystallization kinetics data and the Avrami coefficients extracted from the isothermal crystallization data are then used in a global nonlinear optimization algorithm implemented in Matlab© to determine the parameters in Equation (4).

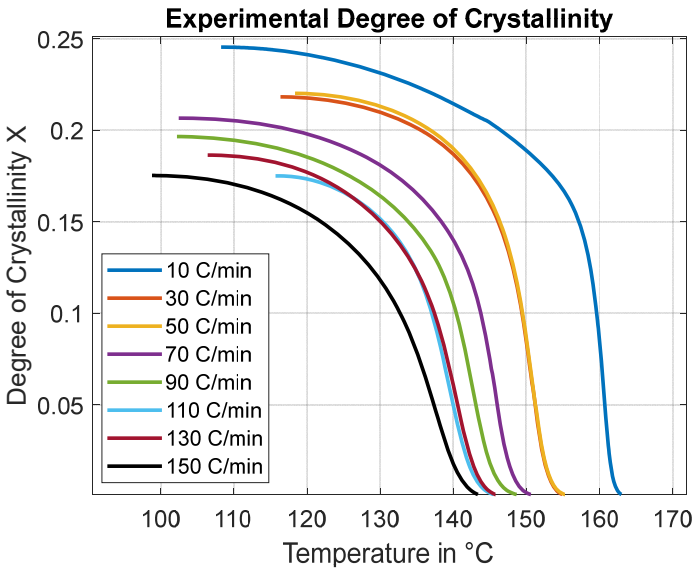

Figure 23. Example of the evolution of the degree of crystallinity at different cooling rates for a semi-crystalline polymer.

Polymer Melting

Melting of polymer crystals is essentially the reverse of crystallization. The melting behavior of polymer crystals depends upon the crystallization history of the semi-crystalline polymer [17]. While fine crystals developed under rapid cooling rates will melt at relatively low temperatures, large crystals formed under a slow cooling process will melt at temperatures closer to the equilibrium melting temperature. Therefore, we can expect melting to occur over a range of temperatures defined by the distribution of crystal sizes formed during the cooling process of the material. The dependence of the melting temperature on the crystal size is shown through the thermodynamics of melting which can be found elsewhere [14,15].

Melting is relevant in EDAM process simulations to capture potential melting of crystal polymers that can occur when a bead of molten material develops contact with material that is either partially or fully crystallized. The melting behavior of the printed material is captured in process simulations through a phenomenological model developed by Greco and Maffezzoli [18]. This model assumes a distribution of crystal lamellar thickness with a sharpness factor k_{mb} and a distribution factor d as given by Equation (6). Further, the temperature T_C corresponds to the peak in the heat flow signal characterized via DSC.

$$\frac{dX_{vc}}{dT} = k_{mb}\{exp[-k_{mb}(T - T_c)]\} \cdot (1 + (d-1)\, exp[-k_{mb}(T - T_c)])^{\frac{d}{1-d}} \quad (6)$$

To characterize the parameters in Equation (6), melting experiments were carried out in the DSC at heating rates of up to $150.0\ °C/min$ with samples cooled from the melt at cooling rates of similar magnitude. Figure 22 shows an example of a DSC experiment that provides data for characterizing the crystallization and melting models. The melting behavior is extracted from the second heating and cooling cycle to erase the cooling history of the manufacturing process of the material. A global nonlinear optimization algorithm implemented in Matlab© is used to characterize the parameters of the melting model, shown in Equation (6), based on the experimental DSC data.

Thermoviscoelastic Behavior

Unlike elastic materials like metals, polymers show a viscoelastic mechanical material behavior. This means that they exhibit both the solid characteristics of elastic materials and store elastic energy when loaded, but also dissipate a part of the energy and flow on the microscale showing a fluid-like behavior. Therefore, time becomes an essential parameter for the material description. A detailed discussion of the reasons for this combined behavior based on the morphology of polymers and related physics is beyond the scope of this text, therefore the reader is referred elsewhere for further details [19].

The printed material undergoes temperature changes from the extrusion temperature to the room temperature; therefore, the temperature influence on the viscoelastic material properties must be characterized and modeled to get the full thermoviscoelastic material behavior required for additive process simulations. The thermoviscoelastic behavior is characterized by performing stress relaxation experiments at different temperatures in a temperature range from room temperature to about the glass transition temperature in amorphous polymers and below the crystallization temperature for semi-crystalline polymers. Stress relaxation experiments are conducted at different temperatures in a Dynamic Mechanical Analyzer (DMA), wherein a strain step is applied, and the resulting stress is recorded as a function of time. Figure 24 shows an example of the stress relaxation behavior characterized at different temperature for a fiber reinforced polymer.

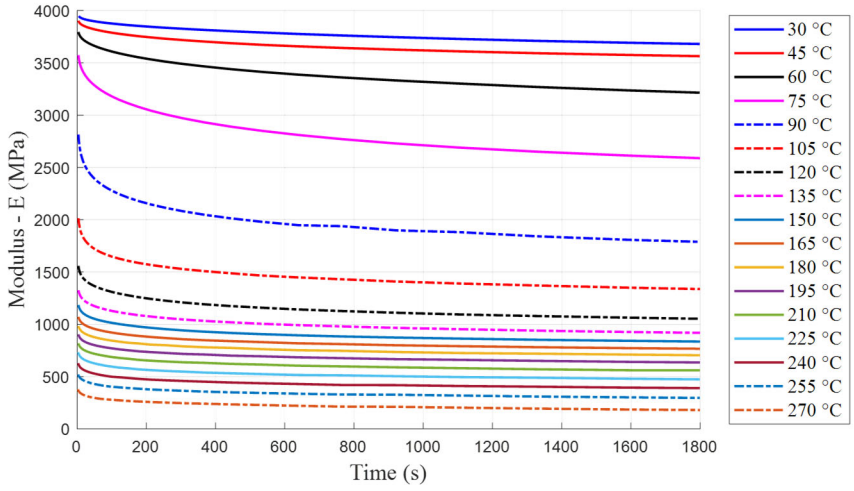

Figure 24. Example of stress relaxation experiments carried out in DMA at different temperatures.

For a thermorheologically simple material, the stress relaxation curves obtained from stress relaxation experiments are shifted horizontally to form a relaxation master curve. Further, following the time-temperature superposition principle, the time shifting process also implies that the stress relaxation behavior characterized at a given temperature is equivalent to the behavior characterized over a longer time at a lower temperature [19]. Similarly, for a thermorheologically simple material, the relaxation times of the polymers scale in a similar way with temperature [19]. Amorphous polymers that only develop one major molecular transition around the glass transition temperature behave as thermorheologically simple [20] whereas semi-crystalline polymers exhibit a thermorheologically complex behavior due to the second molecular transition caused by crystallization. Nevertheless, a semi-crystalline material can be treated as thermorheologically simple if only the temperature range from the room temperature to before the temperature of crystal melting is consider in fully crystallized material.

The stress relaxation experiments at different temperature are shifted with respect to a reference temperature T_o to generate a master curve as shown in the example given in Figure 25. The time shifting procedure is carried out in the logarithmic scale, and data for temperatures higher than the reference temperature are shifted to the right whereas data for temperatures lower than the reference temperature are shifted to the left in order to form a continuous function that spans over multiple decades of time. During the time shifting process, the logarithm of the time shifted for a specific temperature provides the shift factor a_T which will be utilized to stablish the relationship between time and temperature (time-temperature-superposition TTS).

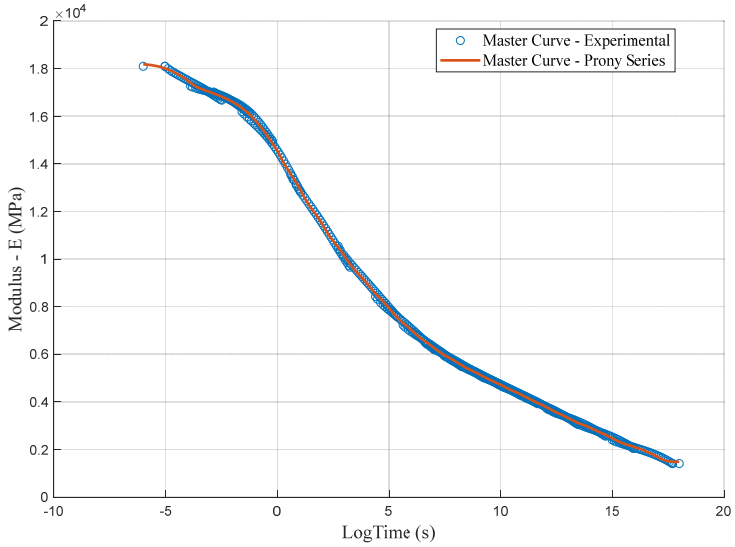

Figure 25. Example of master curve generated from stress relaxation experiments carried out at different temperatures.

Following generation of the master curve, a generalized Maxwell model consisting of N Maxwell elements (spring and dashpot configured in series) connected in parallel is used to capture the evolution of modulus with time given in the master curve [19]. Equation (7) shows the generalized Maxwell model which is also referred to as Prony series. The Prony series involves N coefficients E_w and N relaxation times λ_w which allows describing the material relaxation behavior over a broad time scale. The accuracy of the material description is controlled by the number of Maxwell elements utilized. To account for the modulus at equilibrium ($t \to \infty$), an equilibrium modulus E_∞ is used in Equation (7) [19]. To fit the Prony series to the experimental master curve, the procedure described by Brinson and Brinson [19] was adopted. Which suggests predefining relaxation times based on the range of reduced time obtained from the experimental results and to use between 1 and 2 Maxwell elements for each decade in time. The fitting of the Prony series to the experimental data is carried out through the local optimization routine lsqcurvefit available in Matlab©. Figure 25 shows a comparison between a master curve characterized experimentally and a Prony series with one Maxwell element per decade fitted to the same experimental data.

$$E(t) = E_\infty + \sum_{w=1}^{N} E_w \exp\left(-\frac{t}{\lambda_w}\right) \tag{7}$$

To describe the behavior of the fiber reinforced printed material as a function of time and temperature, an orthotropic thermoviscoelastic constitutive relation is utilized. An orthotropic

thermoviscoelastic material description requires nine different master curves, one for each independent stiffness tensor component. To reduce the required amount of characterization work, certain assumptions were made for the relaxation behavior of the material based on the three orthogonal planes of material symmetry recognized from the experimental and virtual characterization of the printed material (refer to Tensile Properties and Virtual Methods). Since fibers are dominantly aligned parallel to the printing direction (1-direction), they were expected to strongly influence the relaxation behavior in this direction. In contrast, the matrix behavior was assumed to govern the relaxation behavior of the material in the transverse directions and shear planes. Consequently, two different sets of samples are investigated to determine both the fiber and matrix dominated relaxation characteristics. By testing samples for both the printing direction (1-direction, fiber dominated) and the transverse in-plane direction (2-direction, matrix dominated), the experimental effort is significantly reduced. Following the logic above, the characterized matrix relaxation behavior was adopted for the modulus in the stacking direction (3-direction) and the shear moduli. Thus, the relaxation behavior was normalized and the resulting relaxation functions were used to scale the elastic properties characterized at room temperature experimentally and virtually (see sections Tensile Properties, Shear Properties, and Virtual Methods). This assumption has shown promising results in previous validation of deformation predictions in additive process simulations [2].

To account for the effects of temperature on the viscoelastic behavior, the shift factor function $a_T(T)$ is used to stablish a relationship between the real time t and a reduce time ξ. For the case of transient temperature conditions, the reduce time $\xi(t)$ can be expressed as given by Equation (8) [20]

$$\xi(t) = \int_0^t \frac{1}{a_T\big(T(\tau)\big)}\, d\tau \tag{8}$$

where τ is an arbitrary real variable in the interval $[0, t]$. The William-Landel-Ferry (WLF) equation given by Equation (9) can be used to describe the shift factors as a function of temperatures. This shift factor function is characterized from the shifting of the stress relaxation functions with respect to the reference temperature T_o. While the WLF equations captures the dependance of temperature on the shift factors appropriately for temperatures around and above the glass transition temperature [20], modifications of the same equation can be employed for temperatures below T_g [21].

$$\log a_T = \frac{-C_1(T - T_0)}{C_2 + T - T_0}$$
$$\log(a_T) = \frac{C_1(T_0 - T)^{C_3}}{C_2 + (T_0 - T)^{C_3}}, modified\ WLF \tag{9}$$

Figure 26 shows an example of shift factors and the WLF equation fitted to experimental data with shift factors below and above the reference temperature ($Log\ a_t = 0$).

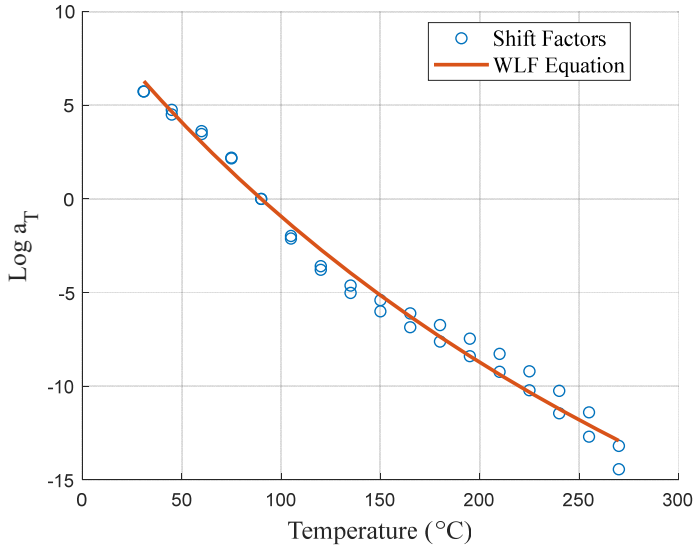

Figure 26. Example of shift factors and WLF equation fitted to experimental data.

To describe the orthotropic thermoviscoelastic behavior of the printed material, Prony series are required to define the nine independent components of the stiffness matrix C_{ij}. Equation (10) provides the definition of the stiffness matrix components wherein C_{ij0} are the relaxed and C_{ijw} the instantaneous parts of the stiffness matrix components, and λ_{ijw} are the relaxation times of the respective Maxwell elements describing the viscoelastic behavior of the material. As stated previously, the relaxation function for the polymer dominated properties was used to scale the elastic properties dominated by the polymer, e.g., $E_3, G_{12}, G_{13}, G_{23}$ whereas the Poisson's ratios were assumed constant. Thus, the components of the stiffness matrix were constructed utilizing a quasi-elastic approximation [22].

$$C_{ij}(T_0, t) = C_{ij0} + \sum_{w=1}^{N} C_{ijw} \exp\left(-\frac{t}{\lambda_{ijw}}\right) \tag{10}$$

Figure 27 shows an example of the nine independent stiffness components represented with Prony

series. Further details on the characterization of the master curves, the generation of the stiffness matrix with Prony series, and the shift factor functions can be found elsewhere [7].

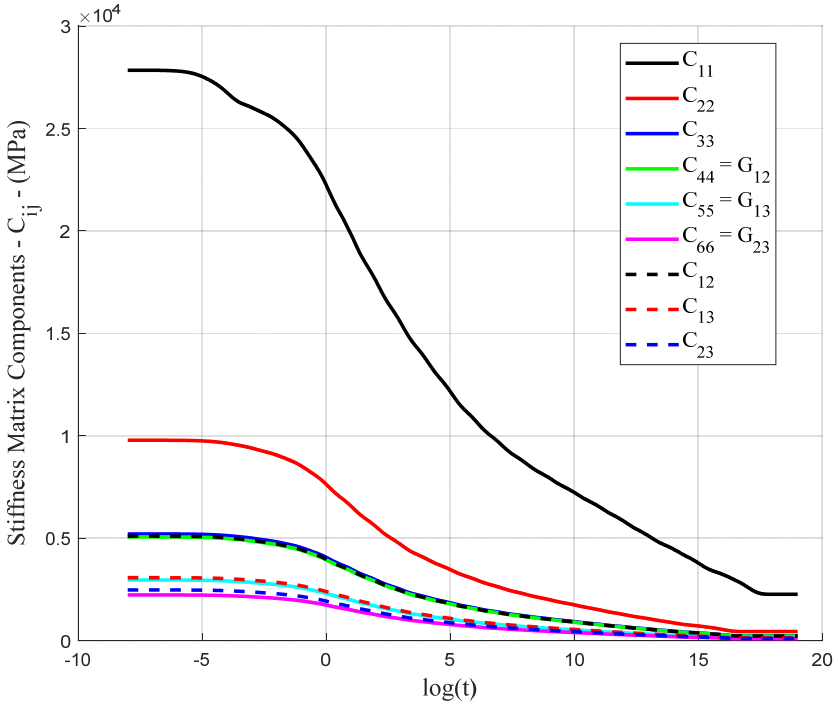

Figure 27. Example of stiffness matrix components described through Prony series.

Thermophysical Properties

Thermophysical properties such as density, heat capacity, and thermal conductivity in the three principal material directions are required for simulating the EDAM process. Further, the thermal conductivities and heat capacity were characterized as a function of temperature from the room temperature to about the processing temperature. The thermophysical characterization was outsourced to the Thermophysical Properties Research Laboratory Inc (TPRL). located in West Lafayette, IN.

Heat Capacity

The heat capacity was characterized as a function of temperature for the printed materials according to the ASTM E1269 [23] standard. The heat capacity is determined by differential scanning calorimetry under an inert atmosphere and with sapphire as the reference material. The reference material and the sample are subjected to the same heat flux and the differential powers required to heat the reference material and sample at the same rate were determined using the digital data acquisition system. Utilizing the mass of the reference material, the differential power,

and the known heat capacity of the sapphire, the heat capacity of the sample is computed. Figure 28 shows an example of the evolution of the heat capacity as a function of temperature along with the heat of crystallization characterized for a semi-crystalline polymer.

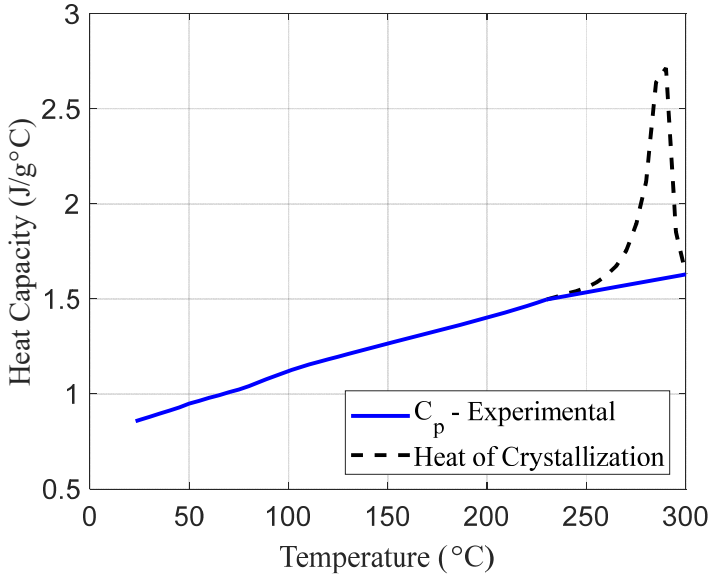

Figure 28. Example of heat capacity as a function of temperature and heat of crystallization characterized for a semi-crystalline polymer.

Thermal Conductivity

The thermal conductivity was determined from measurements of thermal diffusivity, heat capacity, and density for the three principal material directions, namely along the print direction (1-direction), transverse in-plane (2-direction), and layer stacking direction (3-direction). Thermal diffusivity was measured as a function of temperature using the laser flash method according to the ASTM E1461 [24] standard. Thermal conductivity is determined from the product of the thermal diffusivity, the heat capacity, and the density. The density was calculated from the mass and geometry of the samples whereas the heat capacity was measured via DSC. A constant density value was assumed in the calculation of the thermal conductivity. In the laser flash method, the front face of a small disk-shaped sample is subjected to a short laser burst while the resulting temperature rise on the rear face of the sample is recorded and analyzed. The laser flash apparatus employed at TPRL consists of Korad K2 laser, a high vacuum system including a bell jar with windows for monitoring of the sample, a tantalum or stainless steel tube heater surrounding a sample holding assembly, a thermocouple or and IR detector, and a data acquisition system with signal conditioners. The specimens provided to TPRL for characterizing the thermal conductivity were extracted in the three material directions (disks of about 12 mm in diameter) from a block

printed in the CAMRI system. Figure 29 shows an example of the thermal conductivity characterized as a function of temperature via the laser flash method for a fiber reinforced polymer.

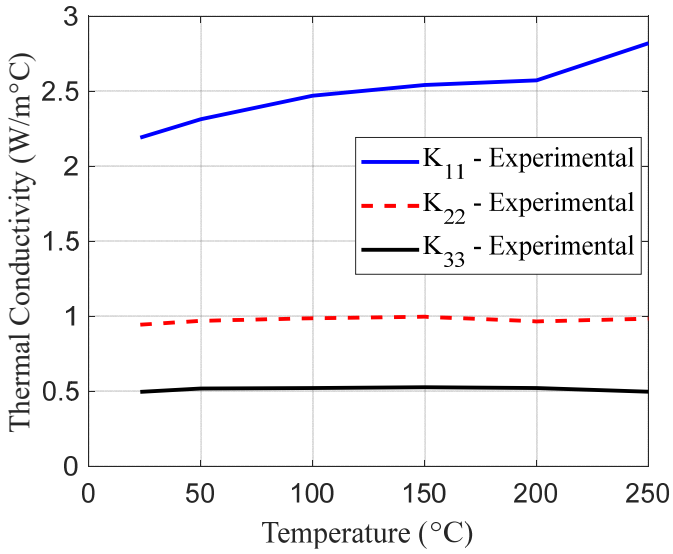

Figure 29. Example of thermal conductivity characterized as a function of temperature for a fiber reinforced polymer in the three principal directions.

Virtual Methods

In addition to the experimental methods described previously, micromechanics-based methods are used to fully characterize the mechanical properties of the composite. However, the micromechanics models require inputs which include the elastic modulus and poisons ratio of the polymer, and the orientation tensor of the short fiber system. To that end, this section presents a method to calculate, virtually, the orientation of the fiber and the in-situ properties of the polymer. The problem is posed as a 'reverse' engineering or inverse problem where some macroscopic properties of the composite are measured, and the properties of the constituents and microstructural characteristics are estimated.

The reverse engineering problem at hand is ubiquitous in literature and is more commonly referred to as inverse problems or model calibration problems. To proceed with the mathematical formulation, let $\boldsymbol{y \epsilon R^m}$ be a set of experiments conducted to infer the model parameters. Physical systems are mathematically represented using a set of model parameters, $\boldsymbol{x \epsilon R^d}$ and a suitable model $\boldsymbol{f(x) : R^d \rightarrow R^m}$. The reverse engineering problem can now be defined as shown in Equation (11).

$$\boldsymbol{x^* = arg\min_x l(f(x), y)} \tag{11}$$

where $l(\cdot,\cdot)$ is a suitable error metric. The model at hand is the mean field homogenization micromechanics model (Mori-Tanaka method) implemented in Digimat and the model parameters are the matrix modulus (E_m), matrix Poisson's ratio (ν_m), and the two terms of the orientation tensor ($a_{11},\ a_{22}$). Note that, in this formulation it is assumed that all the fibers are oriented in the principal material directions. This enables the third component of the orientation tensor to be calculated by, $a_{33} = 1 - a_{11} - a_{22}$. The micromechanics model predicts the 9 independent constants necessary for the orthotropic material description. However, only 5 of the 9 constants are experimentally determined namely - E_1, E_2, E_3, ν_{12}, and ν_{13}. Although some of the shear moduli are measured with experiments, they are not used in the reverse engineering process since the compliance of the interfaces between beads is not considered in the mean-field homogenization micromechanics model, thus leading to erroneous reverse engineered properties. With this limited information, a squared error loss metric as shown in Equation (12) is proposed.

$$l(f(\boldsymbol{x}), \boldsymbol{y}) = \sum_{i=1}^{5} \left(\frac{f_i(x)}{y_i} - 1 \right)^2 \tag{12}$$

where $f_i(\boldsymbol{x})$ is the model prediction for experiment y_i. Note that Equation (12) is essentially the square of the Euclidian norm of the normalized error between the model predictions and the experimental measurements. Response surface approximation is a methodology that approximates an engineering system to optimize some or all of it parameters. In this study, we approximate the loss metric shown in Equation (12) using this methodology. That is, we need to find a function, $f'(w, b)$, that satisfies $f'(w, b) \approx l(f(\boldsymbol{x}), \boldsymbol{y})$. Approximating the loss metric enables the use of complex and computationally expensive micromechanics models but keeping the reverse engineering simple and computationally inexpensive. The method samples the input space at specific locations and evaluates the loss metric at these locations. Once this data is synthesized a suitable map between the input parameters, x, and the loss metric, y', is created which is used for the optimization process. To that end, the support vector regression (SVR) method is used in this study to create the map.

To create the data set for the SVR fitting, we sample the inputs using the Latin Hypercube sampling methodology. Once the inputs have been sampled, the loss metric as shown in Equation (12) at these input points to create the data set. Using this data set the response surface is created and the reverse engineering is performed using the sequential least squares programming method. The method used can be summarized using the flow-chart illustration shown in Figure 30.

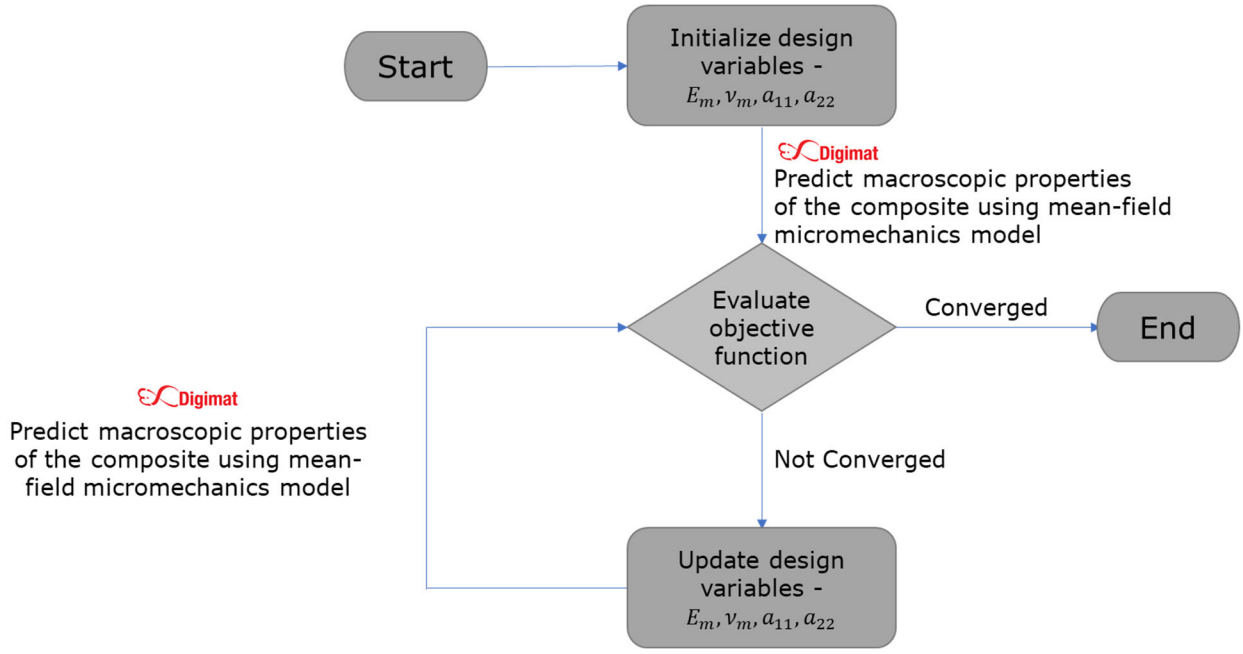

Figure 30. Flowchart summarizing the reverse engineering procedure.

Note that in Figure 30 there is no mention about the response surface approximation and is only meant for an understanding of the reverse engineering procedure at a higher level. Once the properties E_m, ν_m, a_{11}, and a_{22} are determined, the micromechanics model can be used to find the mechanical properties that are not measured experimentally.

Specimen Preparation

The mechanical properties are based on a set of processing conditions including a nozzle size of 4mm, bead width of 6.15mm, bead height of 1.5mm, and nozzle to bead area ratio of 1.44 (as indicated in Table 2).

Table 2. Bead and nozzle dimensions used during the EDAM process.

Parameter	**Value**
Nozzle Diameter	4mm
Bead Width, w	6.15mm
Bead Height, h	1.5mm
Ratio of A_n/A_b	1.44

There are two standard panel types, Panel A (1-3 plane properties) and Panel B (1-2 plane properties), used for extracting the specimens. Figure 31 illustrates these geometries, and the dimensions are provided in Table 3. For some material systems, a lot of warpage is developed during the printing of the Panel B. In case of excessive warpage, the Panel B alternatives are illustrated in Figure 31 and their measurements are provided in Table 3.

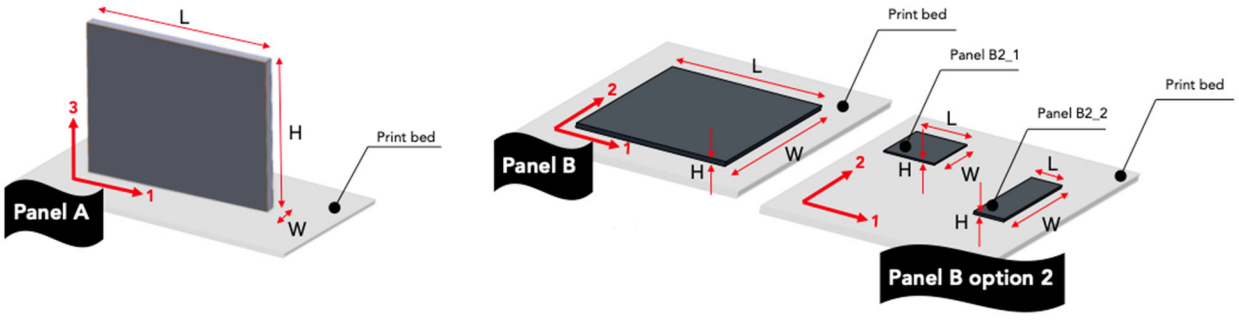

Figure 31 Standard panels geometries for mechanical characterization of 3D-printed material.

Table 3. Standard dimensions for Panel A and Panel B.

	1 direction (X), L	**2 direction (Y), W**	**3 direction (Z), H**
Panel A	320mm	18.45mm*/3beads	321mm
Panel B	320mm	319.8mm	12mm**/8beads
Panel B2_1	175mm	159.9mm	9mm or 12mm*
Panel B2_2	120mm	196.8mm	9mm or 12mm*

Following the printing process of the panels, a heat treatment was conducted to alleviate processing-induced residual stresses. The treatment temperature is around the glass transition temperature T_g of the polymer.

Panel A will have three beads along its width direction (i.e., the 2 direction), the outer-most beads will need to be removed, as shown in Figure 32 Schematic of bead overlap and removal regions for Panel A. The bead overlap is usually 5% or 0.3075mm; however, it is needed to confirm the bead overlap percentage when modifying the factory file. The planer was used to remove the red portions of Panel A. For most panels, the procedure started by incrementally machining away 0.25mm (1/8" of a full revolution of the hand wheel) from each side of the panel (i.e., alternating

sides for each pass) and then slowly attempting to machine 0.5mm (1/4" of a full revolution of the hand wheel). As getting closer to the nominal dimension, the increment depth was decreased to approximately 1/16" of a revolution (i.e., that is 0.125mm). Periodical checks to the thickness of the panel are needed to ensure not over-machining the panel.

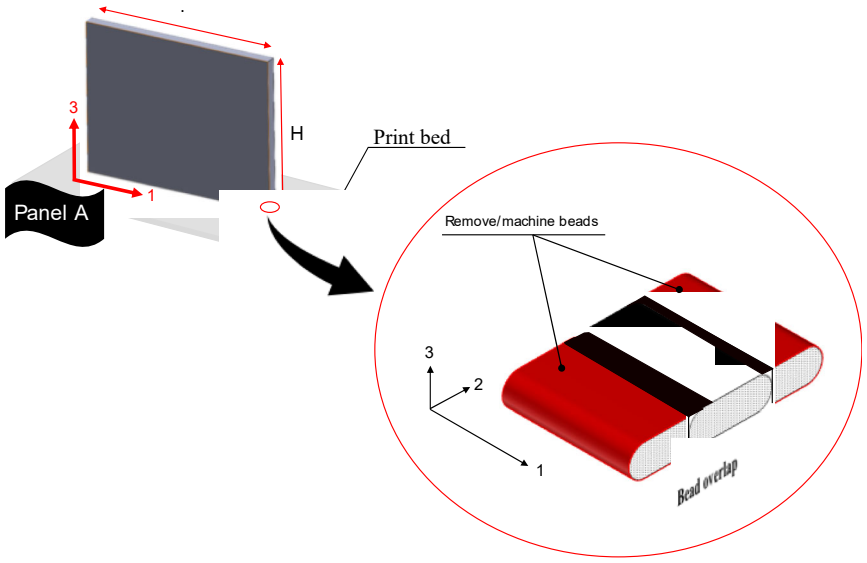

Figure 32 Schematic of bead overlap and removal regions for Panel A.

Panel B contains six or eight beads along its stacking direction (i.e., the 3 direction), the outer-most beads will need to be removed, see Figure 33 Schematic removal regions for Panel B, same for option 2. The planer was used to remove the red portions of *Panel B*. The red portions are approximately 1.5mm or 3mm for six or eight bead heights, respectively. As a starting point, we passed the panel once or twice, depending on the thickness, on each side such that each cutting increment depth is 1.5mm (e.g., one full revolution on the planer is equivalent to 1/16" or 1.5875mm, this means 1.5mm is approximately 0.94 revolution). For getting CTE specimens, we followed the procedure mentioned above with the difference that the nominal thickness desired is changed to 3 mm (2 beads in the stacking direction).

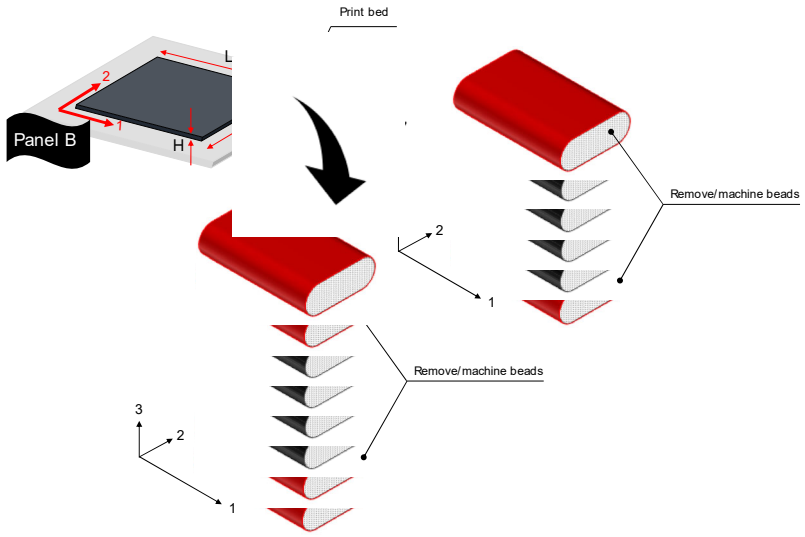

Figure 33 Schematic removal regions for Panel B, same for option 2.

The panels were sectioned using the waterjet cutter. Figure 34 illustrates the dimensions for extracting tension coupons along the 1 direction as well as shear specimens (i.e., along the 1 – 3 direction). Figure 35 shows the dimensions for extracting tension coupons along the 2 directions as well as shear specimens (i.e., along the 1 – 2 direction). Lastly, Figure 36 shows the dimensions for extracting tension coupons along the 3 directions as well as shear specimens (i.e., along the 1 – 3 direction). Dedicated waterjet files were created to get multiple tensile and shear specimens from standard Panel A and B. Finally, the geometry for the CTE experiments is a squared specimen of 1" per side cut out of the Panel B planed down to 3 mm.

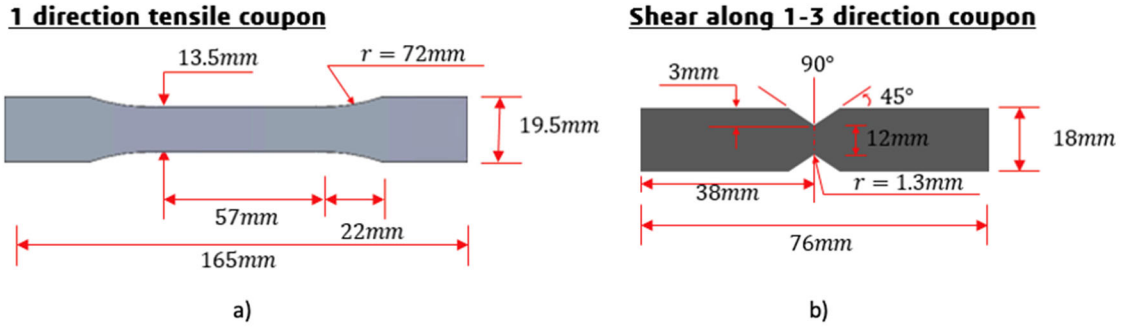

Figure 34 (a) Dimensions for tension specimens along 1 direction. b) Dimension for shear specimens in the 1-3 plane.

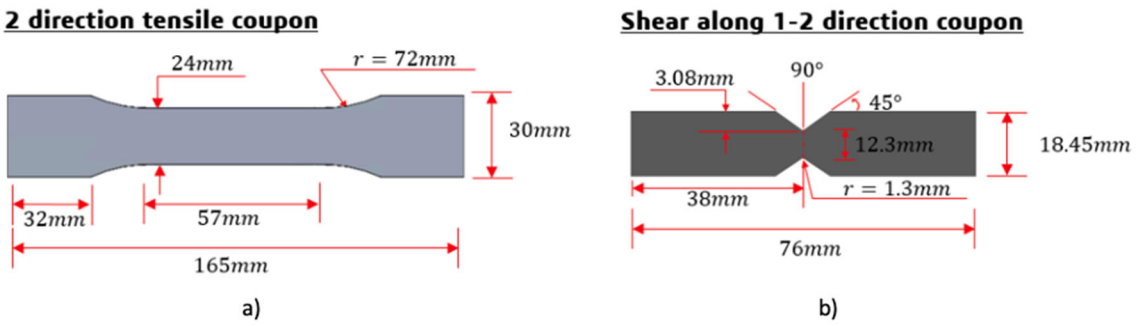

Figure 35. (a) Dimensions for tension specimens along 2-direction. b) Dimension for shear specimens in the 1-2 plane.

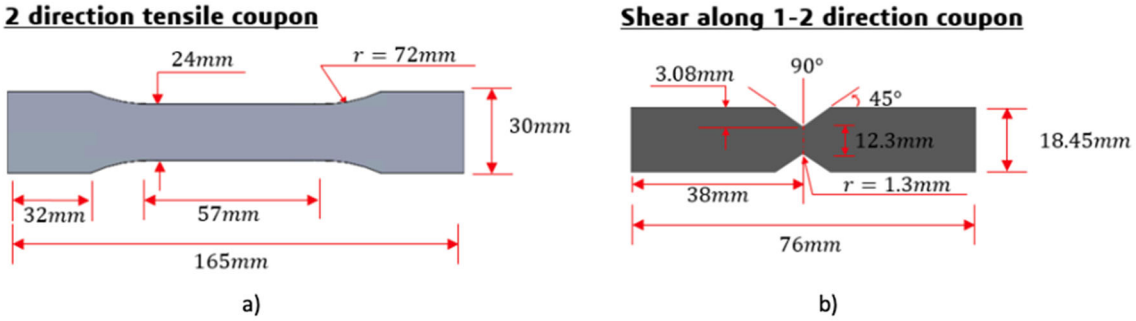

Figure 36. (a) Dimensions for tension specimens along 3 direction. b) Dimension for shear specimens in the 1-3 plane.

After the waterjet cutting process, it was necessary to dry all coupons to remove any absorbed water/moisture. The drying step is imperative for polymers, as they are known to have relatively high moisture absorptivity. All coupons were dried in a polymer pellet drier for 12 hours at 100 $°C$. Nevertheless, depending on the polymer and its characteristics (e.g., such as its T_g), the temperature was adjusted as needed.

Once the coupons are dry, it is pertinent to label them and measure the cross-sectional area using a caliper. After that, the sample speckling can be done. The surfaces that needed to be sprayed with white paint are shown in Figure 37. A relatively thin coating of white paint was applied onto the surfaces of the specimen. Ideally, both surfaces should be spray painted. A relatively thin coat of white spray paint was applied at the surface of the specimen to enhance the contrast with the black speckle pattern. The Correlated Solutions roller was used to apply a stochastic speckle pattern. For the case of the CTE samples, white paint is sprayed to create a pattern that contrasts with the black surface of the material.

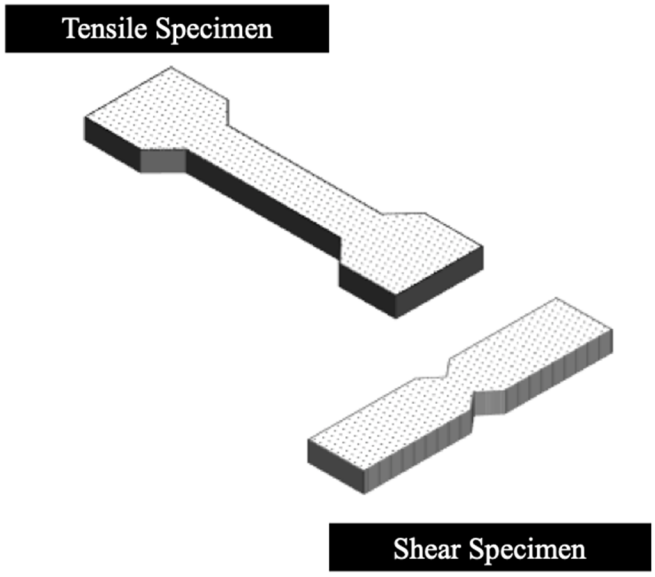

Figure 37 Example of speckle patterned tension and shear specimens.

A similar procedure was followed to prepare samples for the CF-PESU printed in the LSAM. Further details on the sample preparation procedure can be found in previous reports [6].

5. RESULTS AND DISCUSSION

The results of the material characterization for the three material systems are presented and followed by the experimental validation of simulation predictions carried out with ADDITIVE3D©.

Material Characterization

50% wt. CF-PPS 1501 3DP

Glass Transition Temperature

The glass transition temperature of the CF-PPS was determined from the drop in storage modulus as described in the section Glass Transition Temperature. Thus, a glass transition temperature of 94.4 $°C$ was determined from the drop in storage modulus characterized via DMA. Figure 38 shows the storage and loss moduli characterized via DMA and the glass transition temperature determined from drop in the storage modulus.

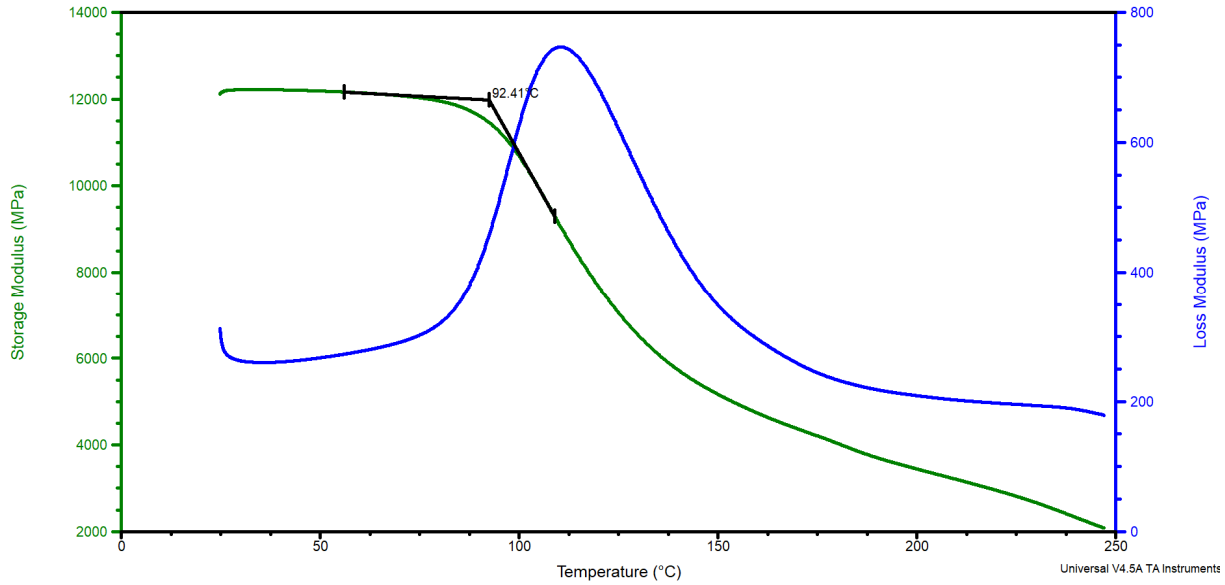

Figure 38. Glass transition temperature of CF-PPS determined from drop in storage modulus.

Microstructural characteristics of material printed in CAMRI

Two microstructural descriptors, namely the fiber length distribution and fiber orientation tensor, were characterized for the beads of 50% wt. CF-PPS printed in the CAMRI system. While the fiber length distribution was characterized experimentally, the fiber orientation tensor was characterized virtually.

Fiber Length Distribution

The fiber length distribution was characterized as described in the section Fiber Length Distribution from samples of 50% wt. CF-PPS printed in the CAMRI system. About one thousand fibers were measured in ImageJ and organized in bins to create a bar plot of the fiber length distribution. Figure 39 shows the fiber length distribution characterized for the 50% wt. CF-PPS. Additionally, the average number fiber length was computed and yielded a value of 87.4 μm. A fiber diameter of 6 μm was measured via optical microscopy which yields an average number fiber aspect ratio of 14.56.

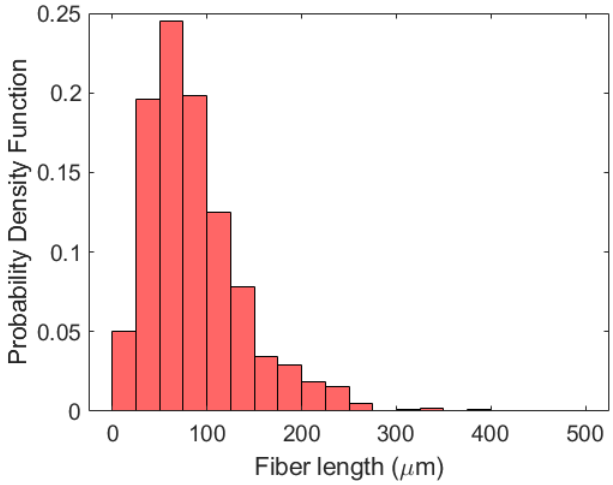

Figure 39 Fiber length distribution characterized for 50% wt. CF-PPS.

Fiber Orientation Tensor

The diagonal components of the second order fiber orientation were calculated using reverse engineering methods discussed in Virtual Methods. Table 4 lists the components of the fiber orientation tensor characterized for the material 50% wt. CF-PPS printed in the CAMRI system with a nozzle diameter of 4 mm and final bead dimensions of 1.5 mm bead height and 6.5 mm bead width.

Table 4. Fiber orientation tensor characterized for 50% CF-PPS.

Orientation Tensor Component	Value
A_{11}	0.65
A_{22}	0.25
A_{33}	0.1

Mechanical Properties

Tensile Properties in the 1-Direction

To measure tensile properties of 50% wt. CF-PPS in the printing direction, eight coupons were prepared according to specimen preparation listed in Specimen Preparation and mechanical tests were conducted as described in Tensile Properties. Sample orientation is shows in Figure 40, where 1 is the printing direction and 3 the stacking direction. Figure 41 shows the strain fields of one specimen of the set at different points of the test.

Figure 40. Tensile coupon for mechanical characterization in the 1-direction.

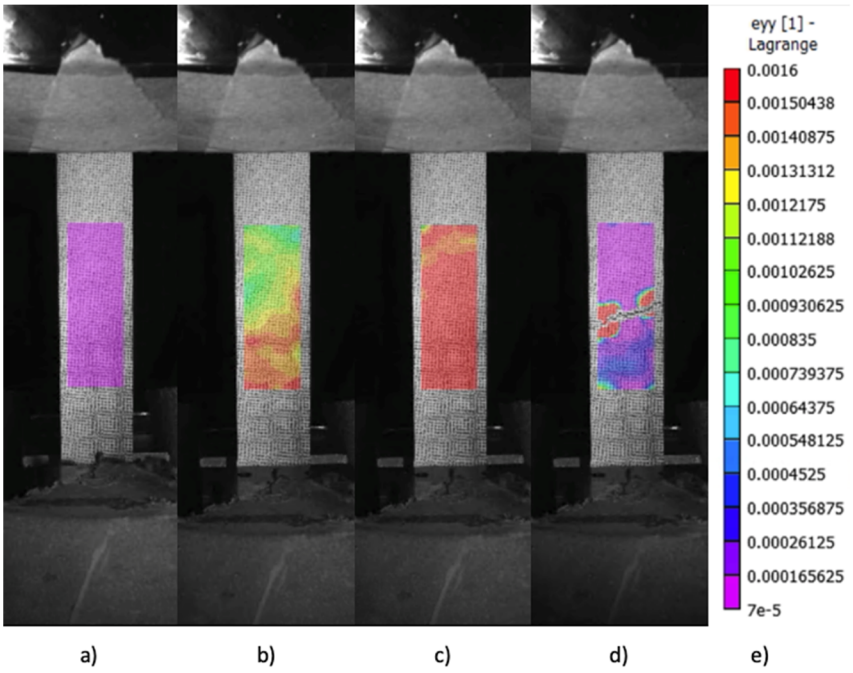

Figure 41. Strain field developed in the loading direction. a) before the load application b) when strains start to develop c) just before failure d) just after failure e) strain field distribution.

Figure 42 shows the stress-strain curves obtained after post-processing the tensile test data for all the specimens. Figure 43 is a plot of the tensile strength values of all specimens showing the mean strength. Finally, Table 5 summarizes the results obtained for the Young's Modulus, Tensile Strength, and Poisson's ratio obtained.

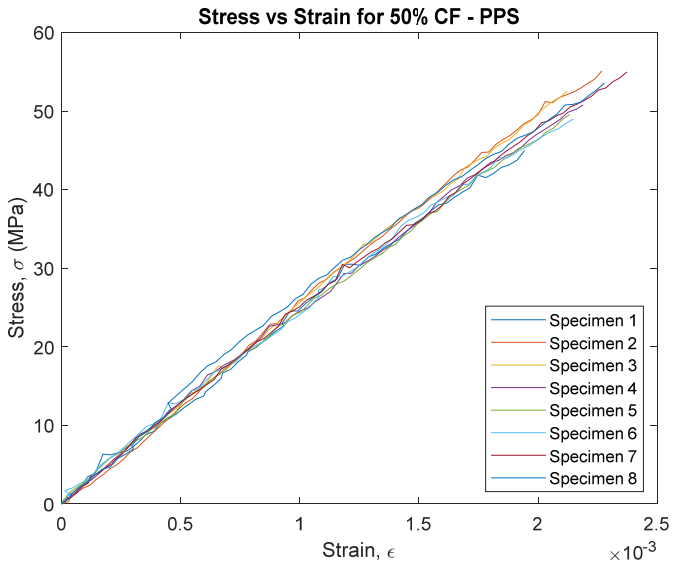

Figure 42. Stress-strain curves of the tensile test in the 1-Direction for 50% CF-PPS.

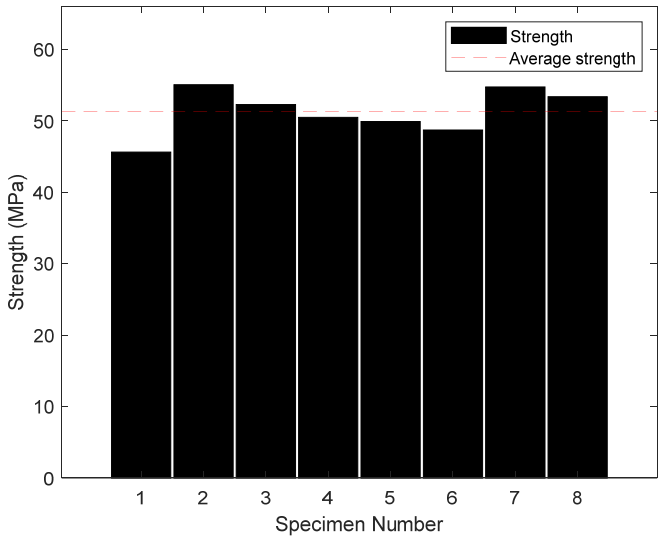

Figure 43. Ultimate strength in the 1-direction for CF-PPS.

Table 5. Tensile test results for CF-PPS in the 1-direction.

50% CF-PPS Printing Direction Tensile Results			
Sample #	Young's Modulus, E_1 $[GPa]$	Poisson's Ratio, ν_{13}	Ultimate Strength, X_1^u $[MPa]$

1	25.84	0.392	45.65
2	26.96	0.390	55.07
3	25.05	0.333	52.29
4	24.26	0.380	50.50
5	24.33	0.352	49.92
6	23.80	0.445	48.73
7	25.70	0.349	54.75
8	24.30	0.356	53.40
AVG	**25.03**	**0.374**	**51.29**
STDEV	1.00	0.033	3.01

Experimental results for tensile properties of 50% CF-PPS manufactured in the CAMRI system indicate mean values of 25.03 GPa for the Young's Modulus, 0.374 for the Poisson's ratio and 51.29 MPa for the Ultimate Tensile Strength, in the printing direction.

Tensile Properties in the 2-Direction

To measure tensile properties of 50% CF-PPS in the transverse direction, ten coupons were prepared according to specimen preparation listed in Specimen Preparation and mechanical tests were conducted as described in Tensile Properties. The sample orientation is indicated in Figure 44, where 1 is the printing direction and 2 is the transverse direction. Figure 45 shows the strain fields at different points of the test for one specimen of the set.

Figure 44 Tensile coupon orientation for the 2-direction characterization

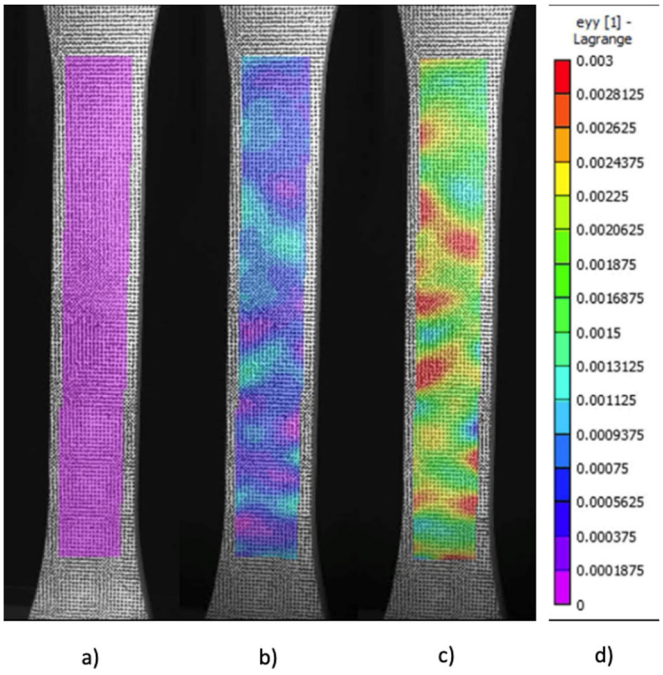

Figure 45. Strain field developed in the load direction at different instants of time. a) before the load application b) when strains start to develop c) just before failure d) strain field distribution.

Figure 46 shows the stress-strain curves for all samples obtained after post-processing the tensile test data. Figure 47 is a plot of the tensile strength values for all specimens along with the mean strength value. Finally, Table 6 summarizes the results obtained for the Young's Modulus, Tensile Strength and Poisson's ratio.

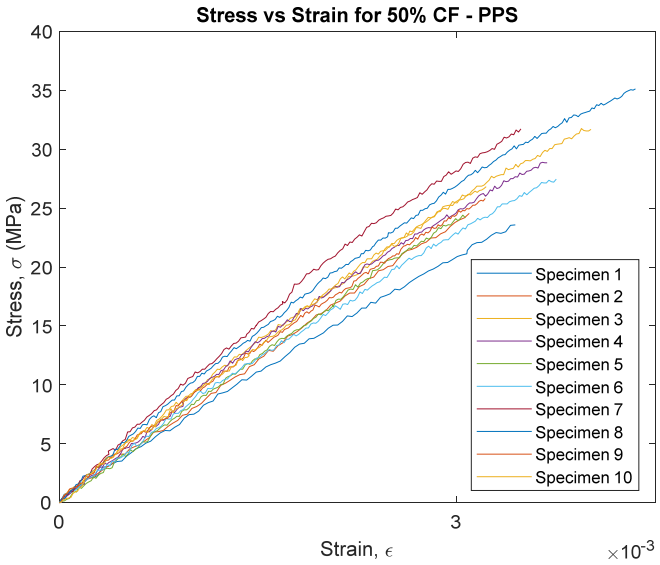

Figure 46. Stress-strain curves of the tensile test in the 2-Direction for 50% CF-PPS.

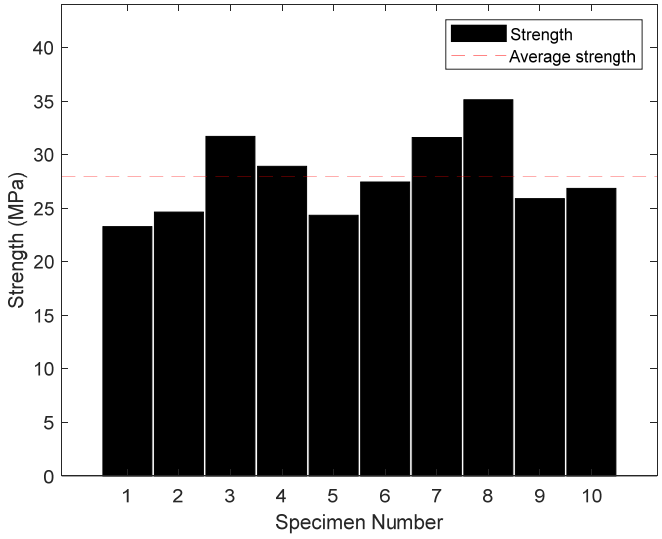

Figure 47. Ultimate strength values of the 2-Direction coupons made of 50% CF-PPS.

Table 6. Tensile test results for CF-PPS in the 2-Direction.

50% CF-PPS Transverse Direction Tensile Results			
Sample #	Young's Modulus, E_2 $[GPa]$	Poisson's Ratio, ν_{21}	Ultimate Strength, X_2^u $[MPa]$
1	7.05	0.093	23.28
2	8.32	0.116	24.63
3	8.31	0.129	31.71
4	8.58	0.179	28.91
5	8.24	0.072	24.34
6	7.08	0.115	27.44
7	9.22	0.175	31.60
8	8.72	0.140	35.13
9	8.21	0.111	25.89

10	8.30	0.106	26.85
AVG	**8.20**	**0.124**	**27.98**
STDEV	**0.67**	**0.033**	**3.82**

Experimental results for tensile properties of 50% wt. CF-PPS manufactured in the CAMRI system indicate mean values of 8.2 GPa for the Young's Modulus, 0.124 for the Poisson's ratio and 27.98 MPa for the Ultimate Tensile Strength, in the transverse direction.

Tensile Properties in the 3-Direction

To measure tensile properties of 50% wt. CF-PPS in the stacking direction, nine coupons were prepared according to specimen preparation listed in Specimen Preparation and mechanical tests were conducted as described in Tensile Properties. The sample orientation is indicated in Figure 48, where 1 is the printing direction and 3 the stacking direction. Figure 49 shows the strain fields of one specimen of the set at different points of the test.

Figure 48. Tensile coupon orientation for characterization in the 3-direction.

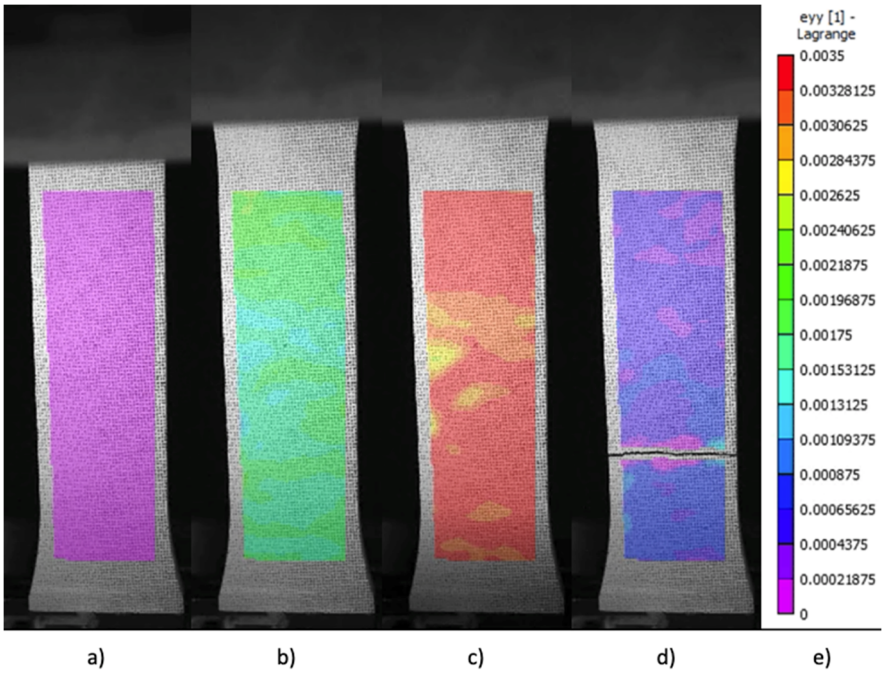

Figure 49. Longitudinal strain field developed by the specimen at: a) before the load application b) when strains start to develop c) just before failure d) just after failure e) strain field distribution.

Figure 50 shows the stress-strain curves obtained out of the data reduction and post-processing analysis for every sample. Figure 51 is a plot of the strength values considered for the mean strength computation of this experimental set. Finally, Table 7 summarizes the results obtained for the Young's Modulus, Tensile Strength and Poisson's ratio obtained.

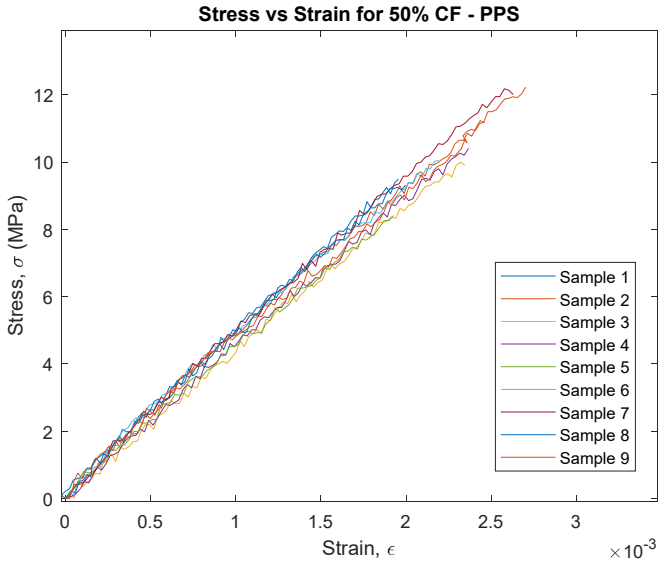

Figure 50. Stress-strain curves of the tensile test in the 3-direction for CF-PPS.

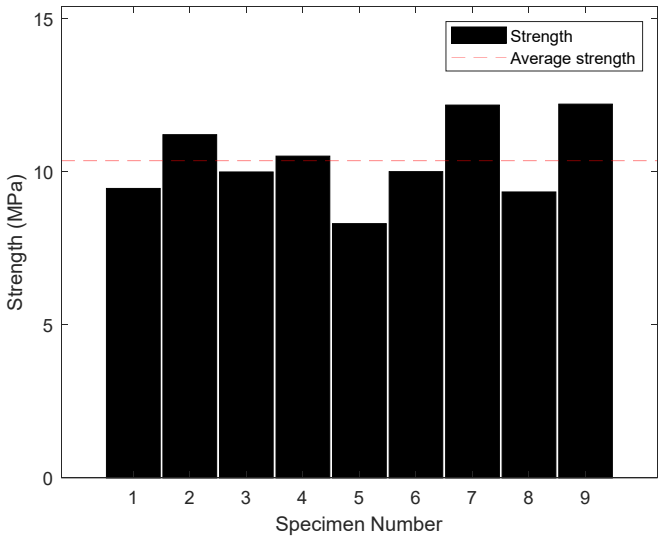

Figure 51. Ultimate strength in the 3-direction characterized for CF-PPS.

Table 7. Results tensile test for CF-PPS in the 3-direction.

50% CF-PPS Stacking Direction Tensile Results			
Sample #	Young's Modulus, E_3 $[GPa]$	Poisson's Ratio, ν_{31}	Ultimate Strength, X_3^u $[MPa]$
1	4.94	0.085	9.46
2	4.67	0.088	11.21
3	4.40	0.055	9.99
4	4.59	0.022	10.51
5	4.53	0.093	8.31
6	4.34	0.082	10.00
7	4.45	0.056	12.18
8	4.37	0.058	9.34

9	4.02	0.061	12.21
AVG	**4.48**	**0.067**	**10.36**
STDEV	**0.24**	**0.021**	**1.24**

Experimental results for tensile properties of 50% wt. CF-PPS manufactured in the CAMRI system indicate mean values of 4.48 GPa for the Young's Modulus, 0.067 for the Poisson's ratio and 10.36 MPa for the Ultimate Tensile Strength, in the stacking direction.

Shear Properties in the 1-3 plane

To measure shear properties of 50% wt. CF-PPS, seven V-notch coupons were prepared with length along printing direction and height along stacking direction, according to specimen preparation listed in Specimen Preparation and shear tests were conducted as described in Shear Properties. The sample orientation is indicated in Figure 52, where 1 is the printing direction and 3 the stacking direction. Figure 53 shows the strain fields of one specimen of the set at different points of the test.

Figure 52. Shear coupon orientation for the 1-3 plane characterization.

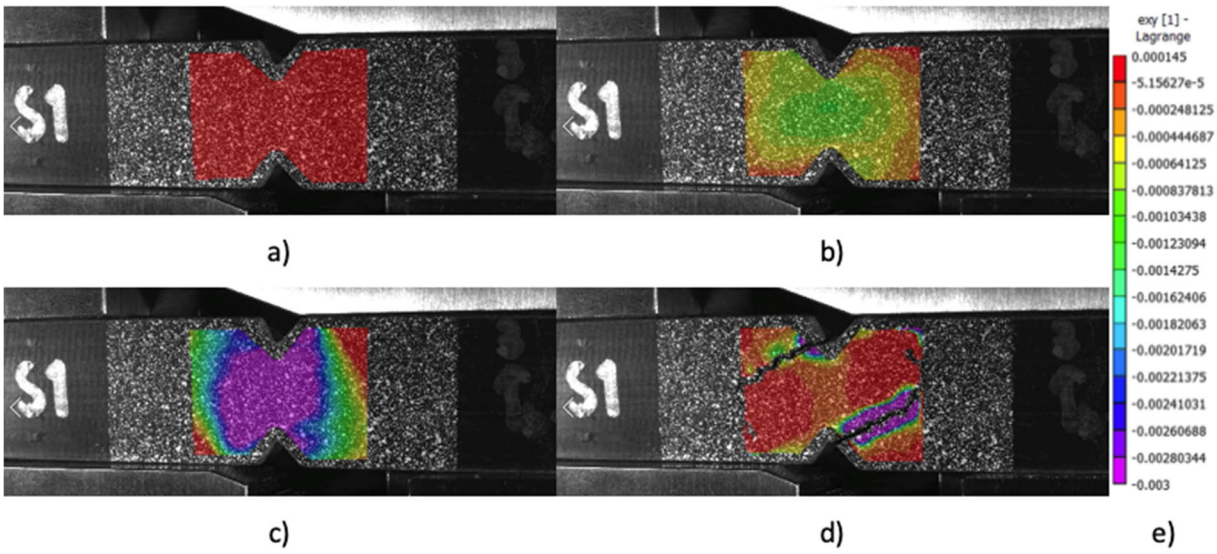

Figure 53. Shear strain field developed by the specimen at: a) before the load application b) when strains start to develop c) just before failure d) just after failure e) shear strain field distribution.

Figure 54 shows the shear stress-shear strain curves obtained out of the data reduction and post-processing analysis for every sample. Figure 55 is a plot of the shear strength values considered for the mean shear strength computation of this experimental set. Finally, Table 8 summarizes the results obtained for the Shear Modulus and Shear Strength obtained.

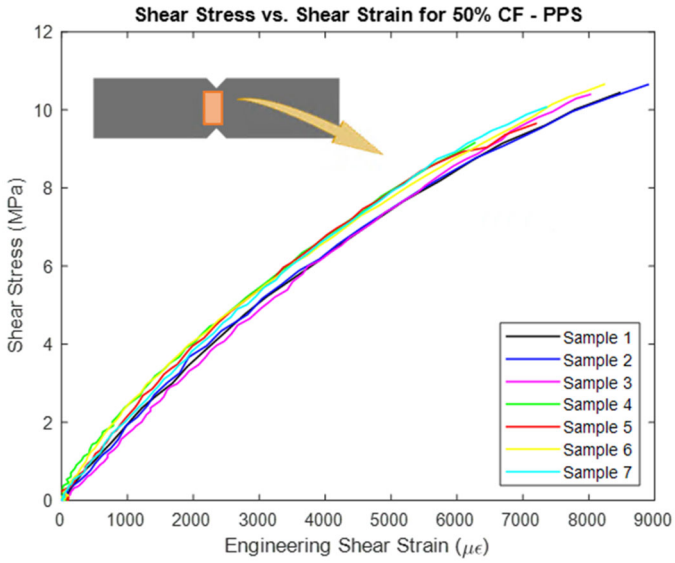

Figure 54. Stress-strain curves of the shear test in the 1-3 plane for 50% CF-PPS.

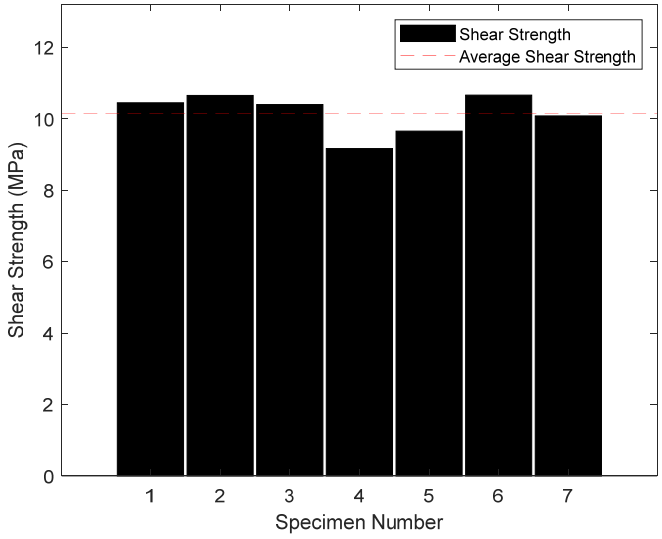

Figure 55. Ultimate shear strength values of the plane 1-3 coupons made of 50% CF-PPS

Table 8. Results shear test in the 1-3 plane for CF-PPS.

50% CF-PPS 1-3 Plane Shear Results		
Sample #	Shear Modulus, G_{13} $[GPa]$	Ultimate Shear Strength, τ_{13}^{u} $[MPa]$
1	0.97	10.45
2	0.94	10.657
3	1.14	10.403
4	1.06	9.170
5	0.89	9.660
6	1.00	10.665
7	1.09	10.083
AVG	**1.01**	**10.16**
STDEV	**0.09**	**0.56**

Experimental results for shear properties in the 1-3 plane of 50% by weight CF-PPS manufactured in the CAMRI system indicate mean values of 1.01 GPa for the Shear Modulus and 10.16 MPa for the Ultimate Shear Strength.

Thermophysical Properties

An average density of $1.336\ g/cm^3$ was obtained for the CF-PPS based on the density measurements carried out at TPRL for three samples submitted to thermal conductivity measurements. The method used for characterizing the density is described in the section Thermophysical Properties.

Heat Capacity

The heat capacity C_p of the CF-PPS was measured as a function of temperature using the DSC method as previously described in the Heat Capacity section. Figure 56 shows the heat capacity characterized as a function of temperature for the CF-PPS. The heat of crystallization (dashed black line in Figure 56) was decoupled from the heat capacity since the heat of crystallization is captured in the heat transfer analysis and coupled with the evolution of crystallinity.

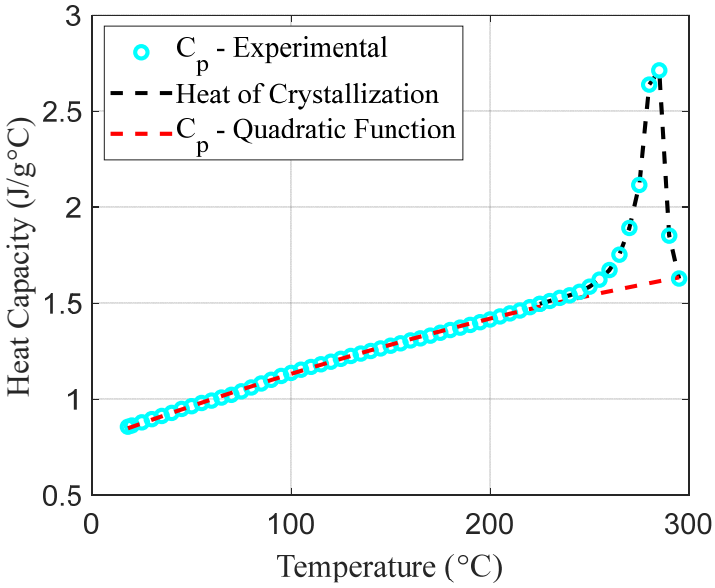

Figure 56. Heat capacity characterized as a function of temperature for the CF-PPS.

A quadratic function (red dashed line in Figure 56) was used to describe the evolution of heat capacity with temperature from room temperature to the processing temperature of $300\ °C$. Table 9 lists the parameters of the quadratic function that describes the heat capacity of the CF-PPS as a function of temperature.

Table 9. Parameters of quadratic function used to describe the heat capacity of CF-PPS as a function of temperature.

$C_p(T) = p_1T^2 + p_2T + p_3$			
	$p_1\ (J/g°C^3)$	$p_2\ (J/g°C^2)$	$p_3\ (J/g°C)$
Value	$-3.172 \cdot 10^{-6}$	$3.832 \cdot 10^{-3}$	$7.806 \cdot 10^{-1}$

Thermal Conductivity

The thermal conductivity was characterized in the three principal material directions for the CF-PPS via the laser flash method as described in the section Thermal Conductivity. The characterization was requested to TPRL from the room temperature to the material processing temperature of $300\ °C$. However, the measurements were only reliable up to $250\ °C$ since the sample was significantly deformed upon melting ($\sim 270\ °C$). Figure 57 shows the thermal conductivity as a function of temperature in the three principal material directions for the CF-PPS.

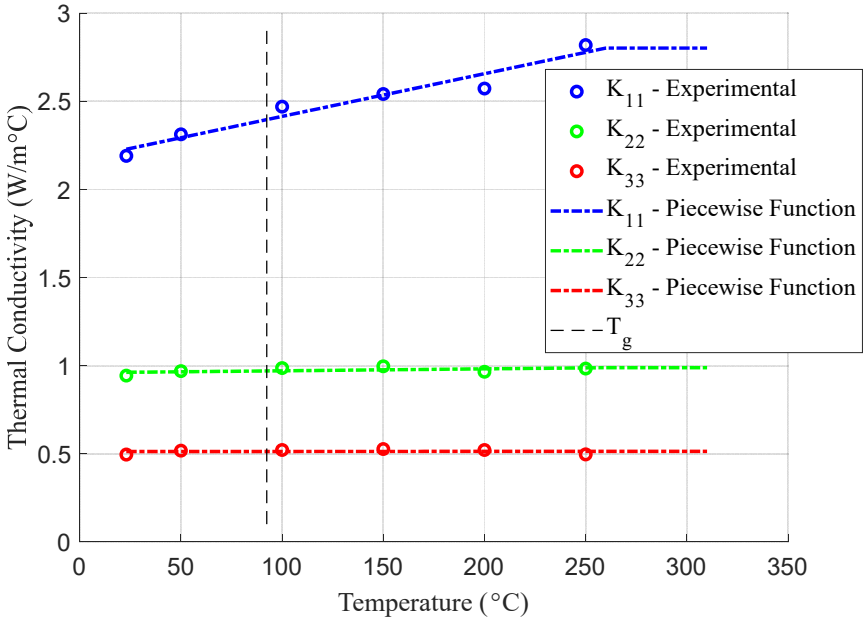

Figure 57. Thermal conductivity as a function of temperature for CF-PPS.

A piecewise function was used to describe the evolution of the thermal conductivity as a function of temperature in the heat transfer analysis of the process simulations. A linear function was used to describe the thermal conductivity from the room temperature to $250\ °C$ whereas a constant value was assumed beyond that temperature. Table 10 lists the parameters of the piecewise functions

used to describe the thermal conductivities of CF-PPS as a function of temperature.

Table 10. Parameters of piecewise functions used to describe thermal conductivities of CF-PPS as a function of temperature.

	$K_{11}\ (W/m°C)$	$K_{22}\ (W/m°C)$	$K_{33}\ (W/m°C)$
$T \leq 250\ °C$	$2.42 \cdot 10^{-3} \cdot T + 2.17$	$1.10 \cdot 10^{-4} \cdot T + 9.59 \cdot 10^{-1}$	$3.74 \cdot 10^{-6} \cdot T + 5.12 \cdot 10^{-1}$
$T > 250\ °C$	2.80	$9.88 \cdot 10^{-1}$	$5.13 \cdot 10^{-1}$

Melting and Crystallization Kinetics

The melting and crystallization kinetics of the CF-PPS was characterized via DSC experiments. A detailed description of the experiments conducted is provided in the sections Polymer Crystallization and Polymer Melting.

Polymer Crystallization

The first step in the characterization of the crystallization kinetics of the CF-PPS was to carry out isothermal crystallization experiments. Isothermal crystallization experiments were carried out in a temperature range from 255 to $261\ °C$ and at intervals of $2\ °C$. Figure 58 shows the heat of crystallization released during the isothermal crystallization experiments with CF-PPS.

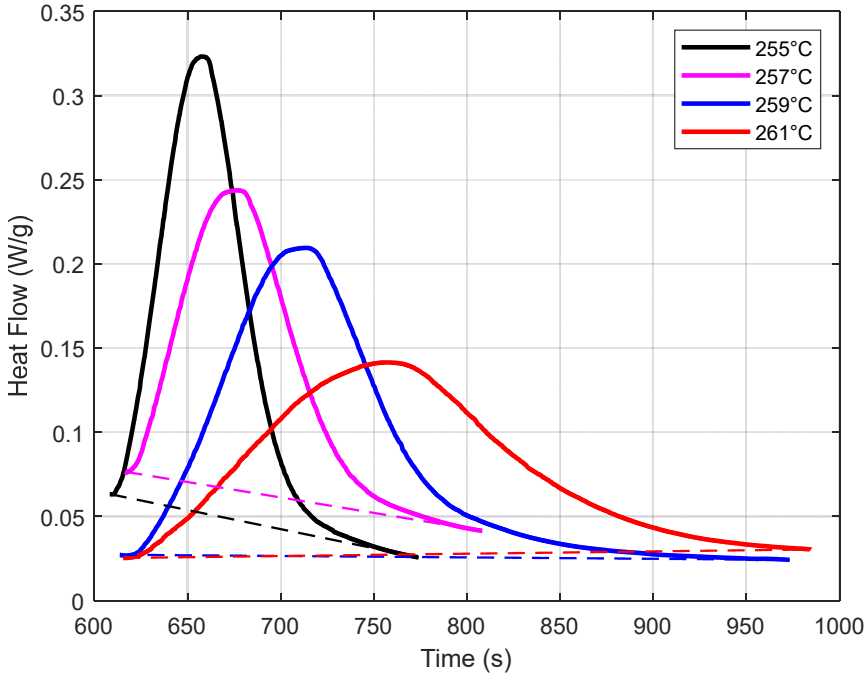

Figure 58. Heat of crystallization released in isothermal crystallization experiments with CF-PPS.

After converting the heat flow to degree of crystallinity (refer to section Polymer Crystallization), a logarithmic transformation is applied to the degree of crystallinity and time to generate an Avrami plot [7,14] as shown in Figure 59 for the CF-PPS. The Avrami coefficients are determined from the slopes of the Avrami plot as shown in Figure 59. Two Avrami coefficients were used to capture the changes in slope for each of the isothermal crystallization kinetics experiments. The average of the Avrami coefficients was computed for n_1 and n_2. Subsequently, the average value was rounded to the nearest integer which yielded values of 3 and 2 for n_1 and n_2, respectively.

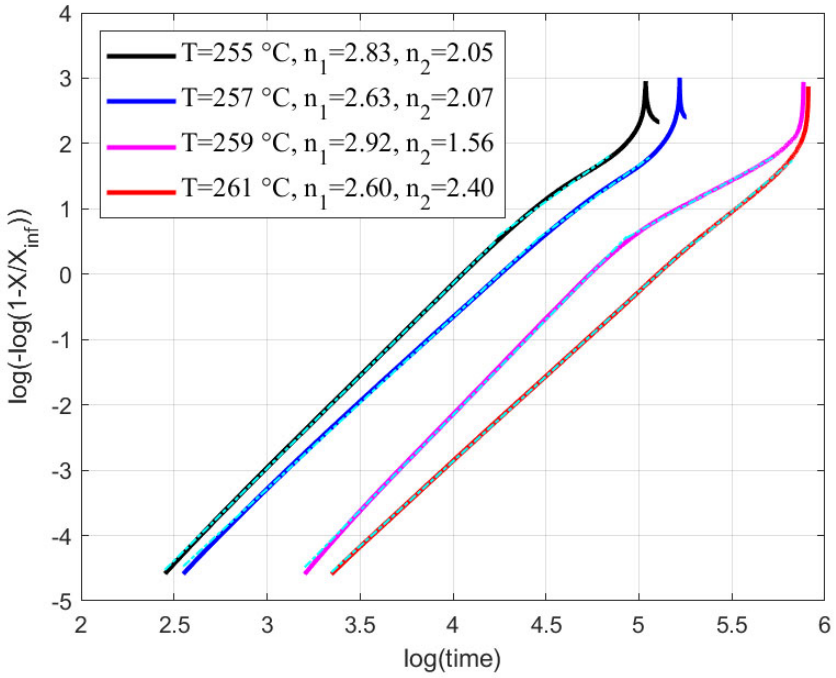

Figure 59. Avrami plot generated from isothermal crystallization experiments for the determination of Avrami coefficient.

To characterize the crystallization kinetics model given by Equation (3) and (4), non-isothermal DSC crystallization experiments were carried out for the CF-PPS at cooling rates from 10 to 120 $°C/min$. Figure 60 shows the evolution of the degree of crystallinity in the CF-PPS for different cooling rates. The Avrami coefficients determined from the isothermal crystallization experiments and the data plotted in Figure 59 were utilized to characterize the parameters of the crystallization kinetics model, as shown in Equation (3) and (4).

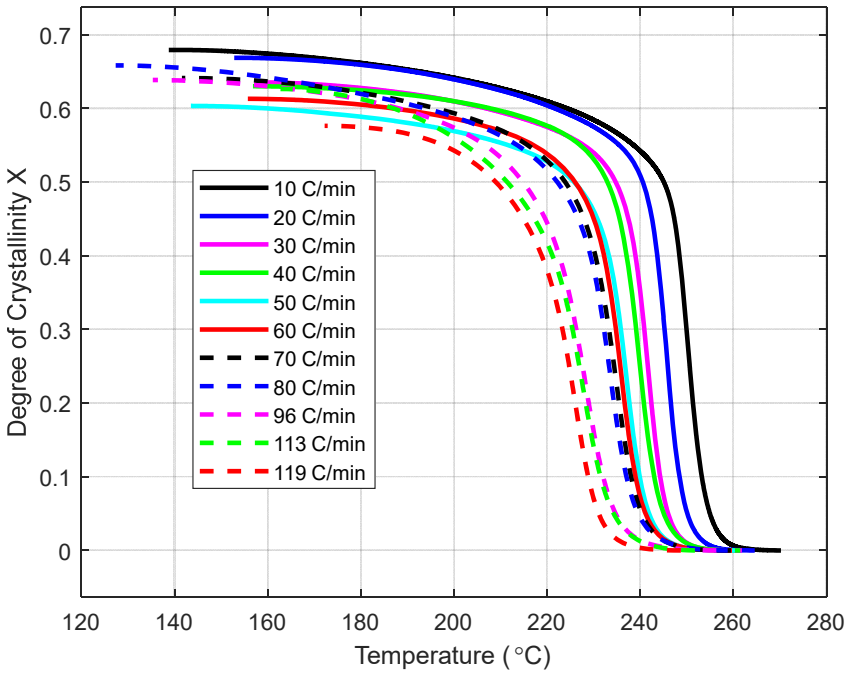

Figure 60. Evolution of degree of crystallinity in CF-PPS for different cooling rates.

After characterizing the parameters of the crystallization kinetics model as described in the section Polymer Crystallization, the evolution of the degree of crystallinity predicted with the model was compared against the experimental measurements. Figure 61 compares the evolution of the degree of crystallinity measured experimentally with the model predictions for the same cooling rates shown in Figure 60.

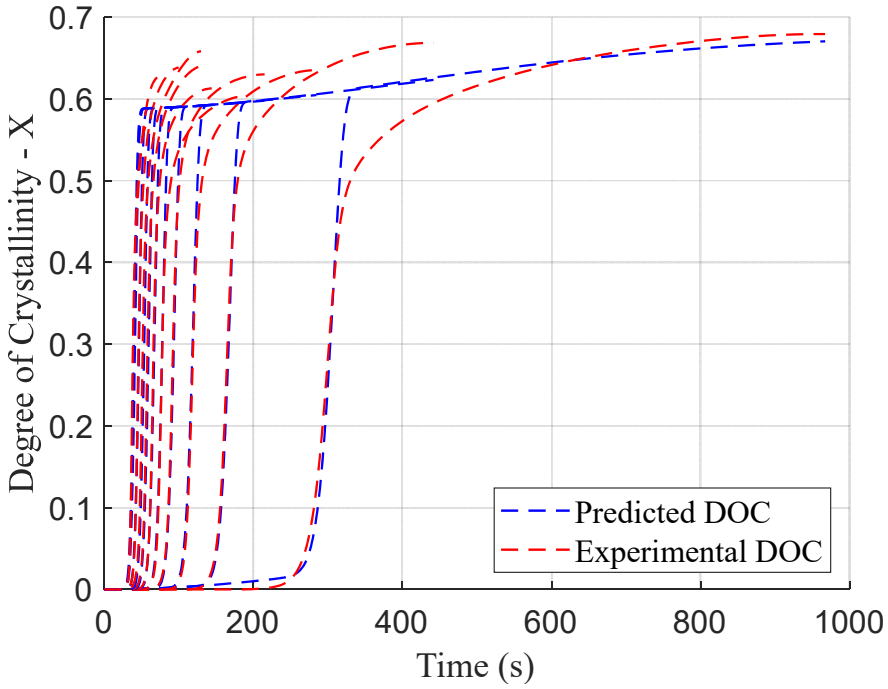

Figure 61. Comparison of degree of crystallinity measured experimentally and predicted with crystallization kinetics model for different cooling rates.

Table 11 lists the parameters of the crystallization kinetics model given by Equation (4) characterized for the CF-PPS.

Table 11. Parameters of crystallization kinetics model characterized for the CF-PPS.

Parameters	Mechanism 1 ($i = 1$)	Mechanism 2 ($i = 2$)
w_i	$8.647 \cdot 10^{-1}$	$1.353 \cdot 10^{-1}$
n_i	3.00	2
C_{1i} $(s^{-n}K^{-1})$	$3.077 \cdot 10^{-4}$	$5.327 \cdot 10^{-9}$
C_{2i} (K)	$4.456 \cdot 10^{2}$	$1.000 \cdot 10^{1}$
C_{3i} (K^3)	$1.449 \cdot 10^{7}$	$7.293 \cdot 10^{1}$
T_{ci} (K)	$1.000 \cdot 10^{1}$	$5.732 \cdot 10^{2}$
T_{mi} (K)	$5.732 \cdot 10^{2}$	$1.130 \cdot 10^{2}$

Polymer Melting

The melting behavior of the crystalline phase in the semi-crystalline polymer is captured in the

simulations of the EDAM process with the model given by Equation (6). The non-isothermal DSC experiments described in the section Polymer Crystallization provided the experimental data required for characterizing the parameters of the melting model. Data for heating rates between 10 and 120 $°C/min$ was considered in the characterization of the melting model. Figure 62 compares the melting behavior characterized via DSC experiments and predicted with the melting model characterized for the CF-PPS.

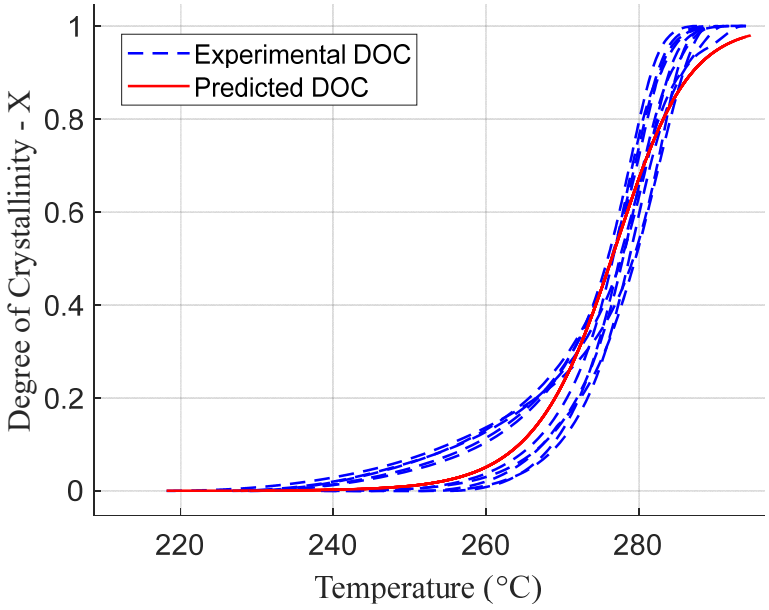

Figure 62. Comparison of the melting behavior characterized experimentally and predicted with the melting model characterized for CF-PPS.

Table 12 lists the parameters of the melting model, shown in Equation (6), characterized for the CF-PPS based on DSC experiments.

Table 12. Parameters of melting model characterized for CF-PPS.

Parameter	Value
$T_C\ (K)$	553.29
k_{mb}	$2.218 \cdot 10^{-1}$
d	1.717

Thermomechanical Properties

To measure the thermomechanical properties of 50% wt. CF-PPS, experimental procedure as

discussed in section Thermo-mechanical Properties was employed to characterize the coefficient of thermal expansion. One sample was prepared in the 1-2 plane and one sample in the 2-3 plane. Only the data measured during the heating cycle of the experiment are reported here. Based on the number of samples prepared, we have data from one sample for characterizing the CTE in the printing and stacking directions, and data from two samples for characterizing CTE in transverse direction.

Figure 63 shows a plot of the variation of thermal strain with temperature for the printing direction, as recorded from the heated stage during the heated cycle. For strain data below T_g, a linear regression model was used. Based on the regression models fit, the mean value of α_3 below T_g was obtained as $4.26\ \frac{\mu\epsilon}{°C}$, while the α_3 for data above T_g was obtained as $7.57\ \frac{\mu\epsilon}{°C}$.

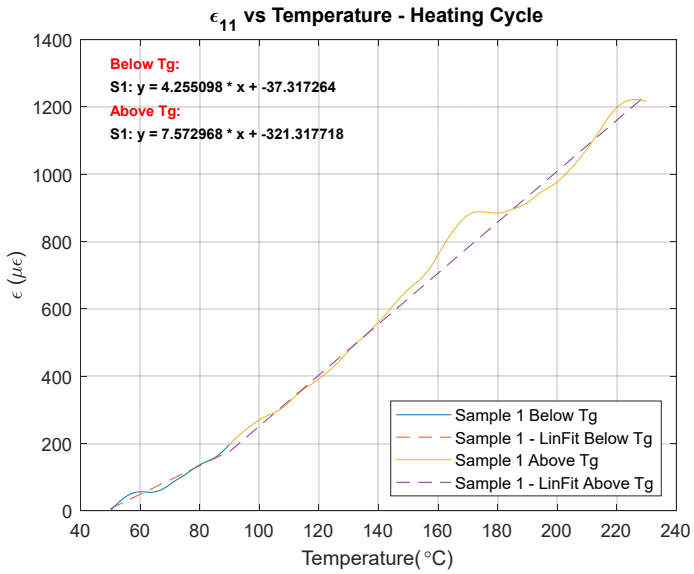

Figure 63 CTE in the 1-direction for 50% CF-PPS.

Figure 64 shows a plot of the variation of thermal strain with temperature for the transverse direction, as recorded from the heated stage during the heated cycle. For strain data below T_g, a linear regression model was used and for data above T_g, a quadratic regression was used. Based on the regression models fit, the mean value of α_3 below T_g was obtained as $25.69\ \frac{\mu\epsilon}{°C}$, while the α_3 for data above T_g was obtained as a linear function $0.18T\ +\ 17.17\ (\mu\epsilon/°C)$.

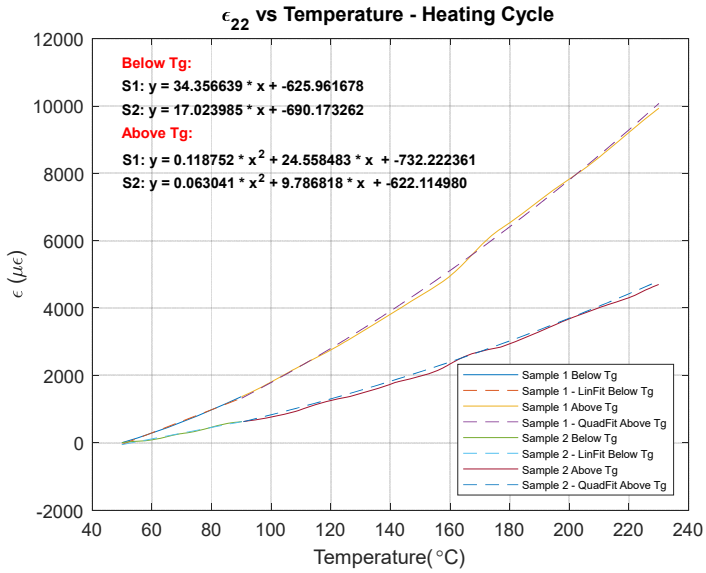

Figure 64 CTE in the 2-direction for 50% CF-PPS

Figure 65 shows a plot of the variation of thermal strain with temperature for the stacking direction, as recorded from the heated stage during the heated cycle. For strain data below T_g, a linear regression model was used and for data above T_g, a quadratic regression was used. Based on the regression models fit, the mean value of α_3 below T_g was obtained as 30.50 $\frac{\mu\epsilon}{°C}$, while the α_3 for data above T_g was obtained as a linear function $0.36T\ +\ 8.58\ (\mu\epsilon/°C)$.

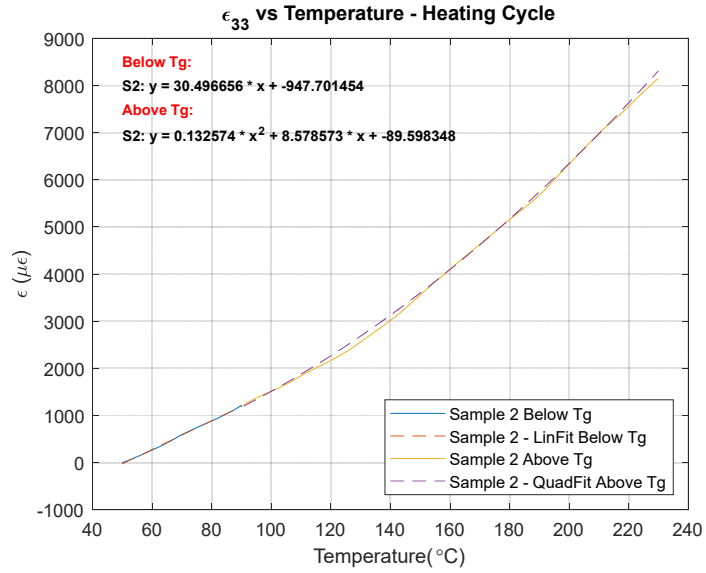

Figure 65. CTE in the 3-direction for 50% CF-PPS.

Table 13 is a summary of the CTE in all directions computed for the 50% CF-PPS for the ranges above and below T_g.

Table 13. Coefficient of thermal expansion of CF-PPS.

50% CF-PPS Coefficient of Thermal Expansion			
	CTE 1-Direction, α_1 $[\mu\epsilon/°C\ ]$	CTE 2-Direction, α_2 $[\mu\epsilon/°C\ ]$	CTE 3-Direction, α_3 $[\mu\epsilon/°C\ ]$
Below T_g	4.26	25.69	30.50
Above T_g	7.57	$0.18T\ +\ 17.17$	$0.36T\ +\ 8.58$

Thermoviscoelastic Properties

Stress relaxation experiments were carried out with samples of CF-PPS in a DMA model Q800 from TA Instruments© and in a temperature range over which the material retains the full crystallinity. The material was characterized in a temperature range from $30\ °C$ to $270\ °C$. Figure 66 shows the stress relaxation experiments carried out in the 1-direction (A) and in the 2-direction for sample of CF-PPS printed in the CAMRI system.

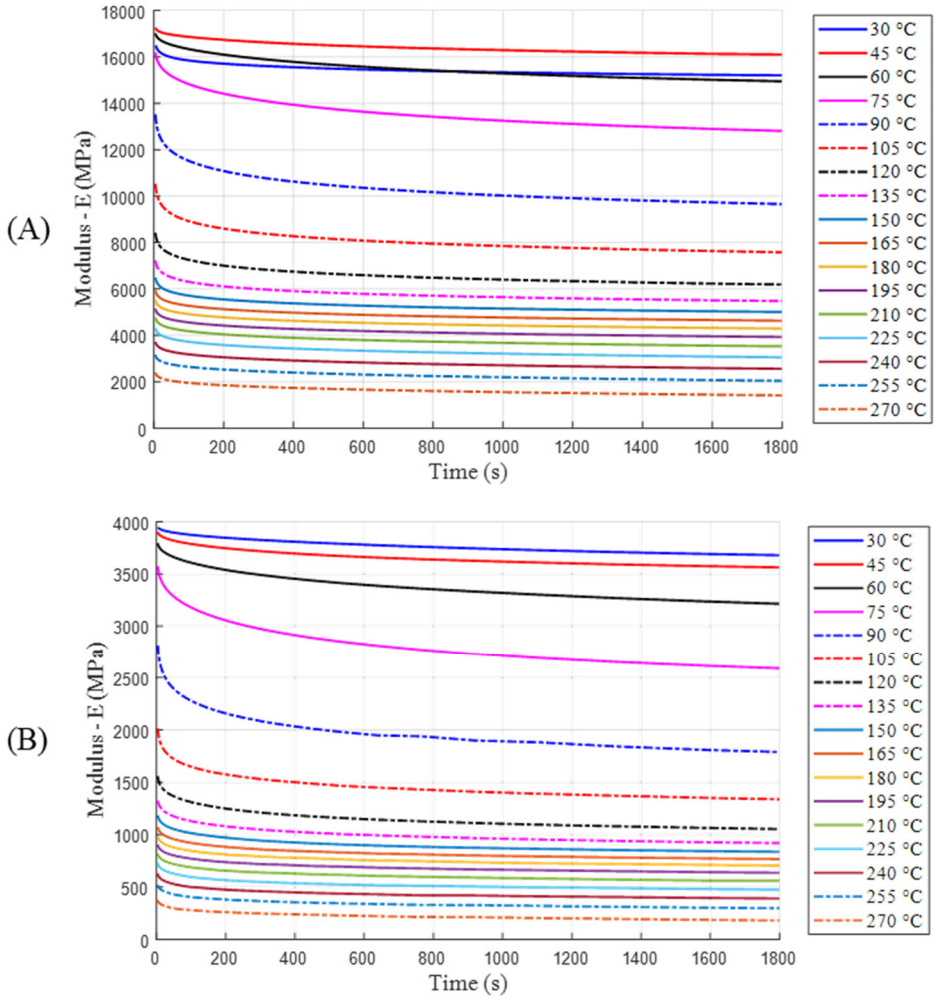

Figure 66. Stress relaxation experiments carried for CF-PPS at multiple temperatures. A) Stress relaxation behavior in the 1-Direction. B) Stress relaxation behavior in the 2-direction.

After characterizing the stress relaxation behavior at different temperatures, master curves were generated by shifting the stress relaxation curves as described in the section Thermoviscoelastic Behavior. Figure 67 A and B shows the master curves generated from the stress relaxation response characterized in the 1 and 2 directions, respectively. Prony series with 24 Maxwell elements were used to fit the master curves in both directions as shown in Figure 67. As a result, the relaxation times were predefined in increments of one decade as discussed in the section Thermoviscoelastic Behavior. To capture the effect of crystallinity in the material behavior, a linear function dependent of crystallinity was used to scale the stiffness matrix as described elsewhere [7].

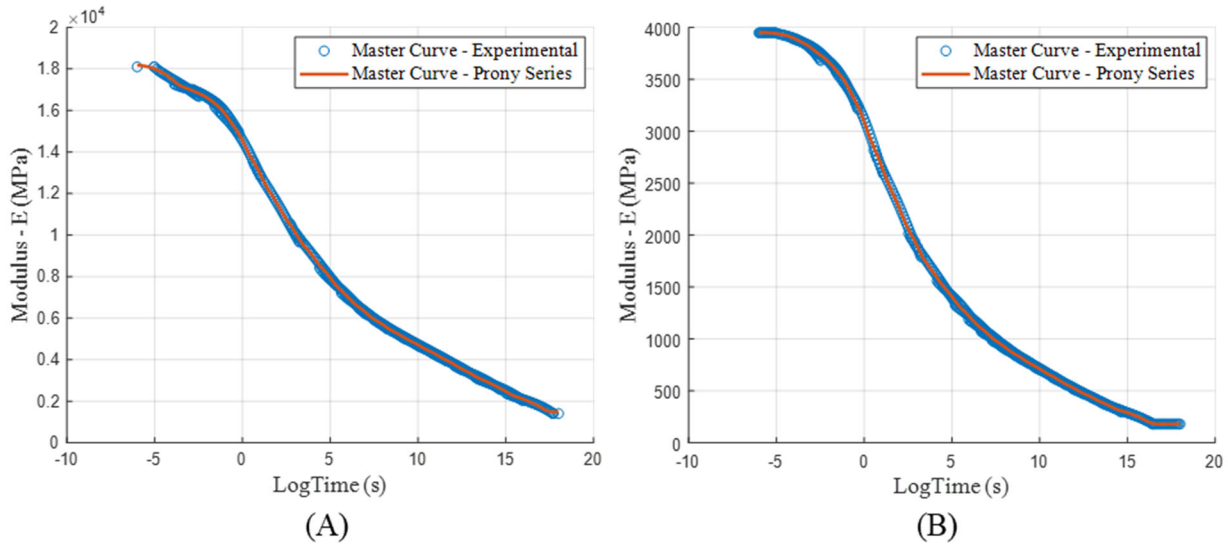

Figure 67. Master curves characterized for the CF-PPS in (A) 1-direction and (B) 2-direction.

A Williams-Landel-Ferry (WLF) equation was adopted for the shift factor function. A single WLF equation was used to fit the shift factors resulting from the generation of master curves in the two material directions. Figure 68 shows the shift factors obtained experimentally and the fit of the WLF equation to the experiments.

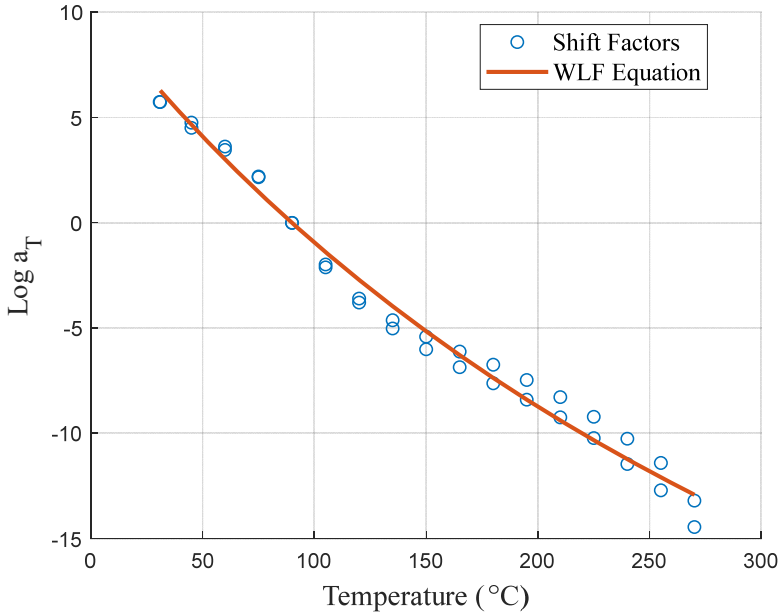

Figure 68. Shift factors and shift factor function characterized for the CF-PPS.

After generating master curves for the fiber dominated material direction (1-direction) and the matrix dominated direction (2-direction), the relaxation functions described through Prony series were normalized. The nine components of the stiffness matrix described through Prony series were generated as described in the section Thermoviscoelastic Behavior. Figure 69 shows the stiffness components of the stiffness matrix described through Prony series for the CF-PPS printed in the CAMRI system.

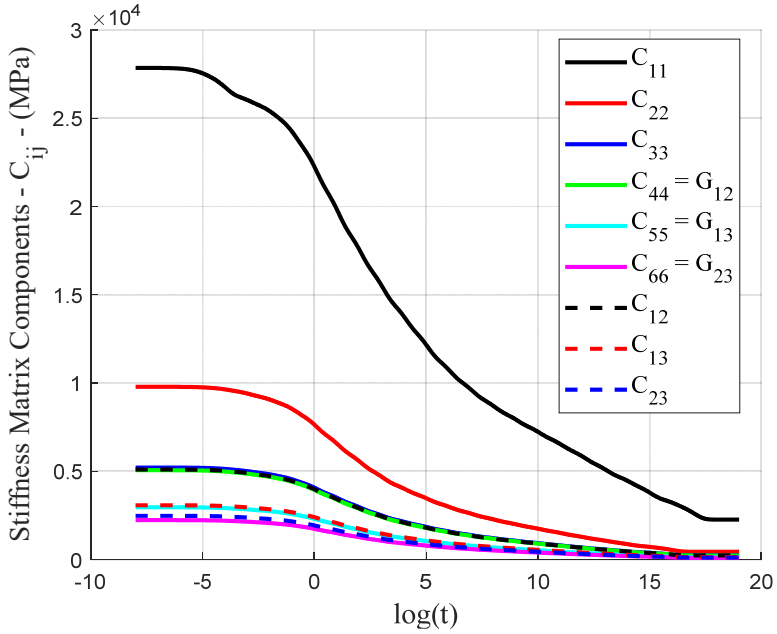

Figure 69. Components of stiffness matrix described through Prony series for the CF-PPS.

Micromechanical Prediction of Material Properties

Once the experimental measurements are carried out, they are used to calibrate a micromechanics model that can predict all the elastic constants of the orthotropic material printed. The calibrated values are given in Table 14. The micromechanics model requires inputs which are not calibrated including the fiber properties and fiber length. The constituent fiber properties were taken from [25] and the fiber aspect ratio was calculated by measuring the fiber length. The fiber length was measured using optical microscopy as described in the section Fiber Length Distribution [26].

Table 14. Reverse engineered values.

Property	Value
Elastic Modulus of Polymer (GPa)	1.78
Poisson's Ratio of Polymer	0.34
a_{11}	0.65
a_{22}	0.25

Once the properties of the polymer and the microstructure descriptors are determined, the micromechanics model can be used to predict elastic properties of the composite that were not measured experimentally. The elastic properties predicted from the micromechanics model are given in Table 15.

Table 15. Micromechanics predictions of the elastic constants of the composite.

Composite Elastic Property	Value
$E_1(GPa)$	23.51
$E_2(GPa)$	8.46
$E_3(GPa)$	5.19
$G_{12}(GPa)$	4.92
$G_{13}(GPa)$	3.01
$G_{23}(GPa)$	2.31
ν_{12}	0.40
ν_{13}	0.36
ν_{23}	0.39

25% wt. CF-PSU 1901 3DP

Glass Transition Temperature

The glass transition temperature of the CF-PSU was determined from the drop in storage modulus as described in the section Glass Transition Temperature. Thus, a glass transition temperature of 186.2 $°C$ was determined from the drop in storage modulus characterized via DMA. Figure 70 shows the storage and loss moduli characterized via DMA and the glass transition temperature determined from drop in the storage modulus.

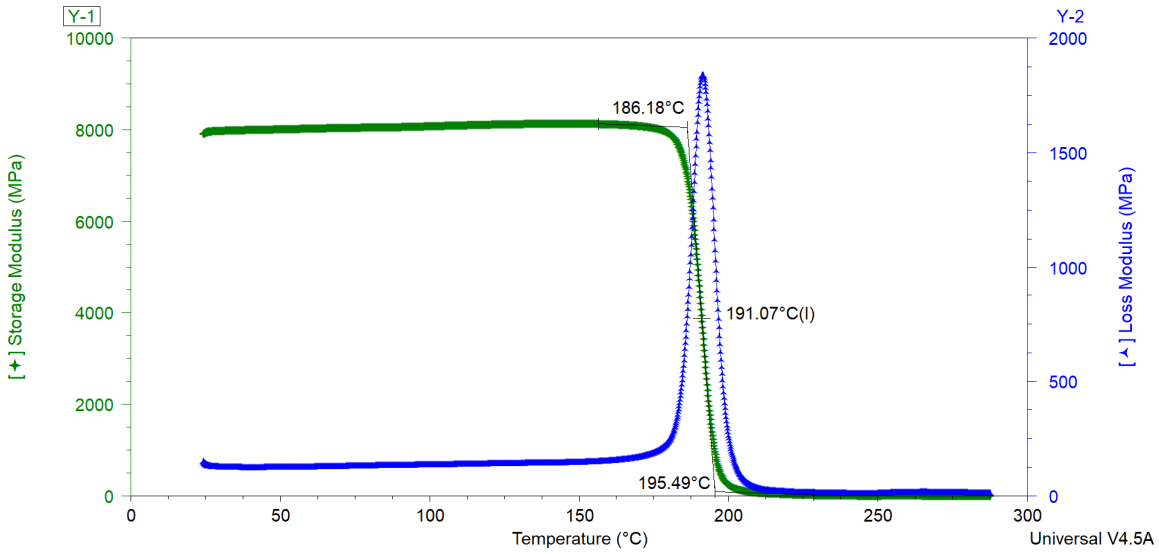

Figure 70. Glass transition temperature of CF-PSU determined from drop in storage modulus.

Microstructural characteristics of material printed in CAMRI

Two microstructural descriptors, namely the fiber length distribution and fiber orientation tensor, were characterized for the beads of 25% wt. CF-PSU printed in the CAMRI system. While the fiber length distribution was characterized experimentally, the fiber orientation tensor was characterized virtually.

Fiber Length Distribution

The fiber length distribution was characterized as described in the section Fiber Length Distribution from samples of 25% wt. CF-PSU printed in the CAMRI system. About one thousand fibers were measured in ImageJ and organized in bins to create a bar plot of the fiber length distribution. Figure 71 shows the fiber length distribution characterized for the 25% wt. CF-PSU. Additionally, the average number fiber length was computed and yielded a value of 87.2 μm. A fiber diameter of 6 μm was measured via optical microscopy which yields an average number fiber aspect ratio of 14.5.

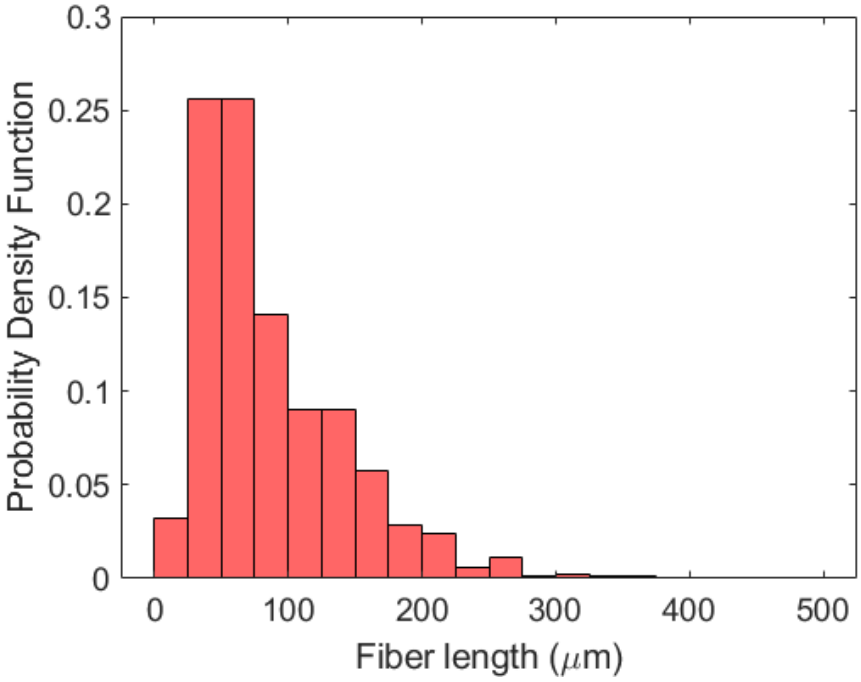

Figure 71. Fiber length distribution characterized for the CF-PSU.

Fiber Orientation Tensor

The fiber orientation tensor was reverse engineered with the method outlined in the section Virtual Methods. Table 16 lists the components of the fiber orientation tensor characterized for the 25% CF-PSU printed in the CAMRI system with a nozzle of four millimeters and with final bead dimensions of $1.5\ mm$ by $6.15\ mm$.

Table 16. Fiber orientation tensor characterized for the CF-PSU.

Orientation Tensor Component	Value
$\boldsymbol{A_{11}}$	0.73
$\boldsymbol{A_{22}}$	0.17
$\boldsymbol{A_{33}}$	0.10

Mechanical Properties

Tensile Properties in the 1-direction

To measure the tensile properties in 1-direction for 25% wt. CF-PSU, fourteen tensile coupons were prepared according to section Specimen Preparation and subjected to the mechanical

tensile test procedure as described in section Tensile Properties. The sample orientation is indicated in Figure 72, where 1 is the printing direction and 3 the stacking direction. Figure 73 shows the strain fields of one specimen of the set at different points of the test.

Figure 72. Tensile coupon orientation for the 1-direction characterization.

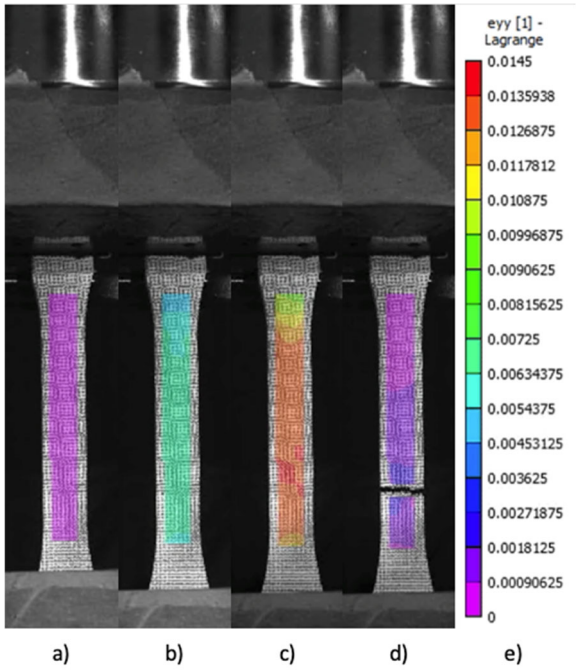

Figure 73. Longitudinal strain field developed by the specimen at: a) before the load application b) when strains start to develop c) just before failure d) just after failure e) strain field distribution

Figure 74 shows the stress-strain curves obtained out of the data reduction and post-processing analysis for every sample. Figure 75 is a plot of the strength values considered for the mean strength computation of this experimental set. Finally, Table 17 summarizes the results obtained for the Young's Modulus, Tensile Strength and Poisson's ratio obtained.

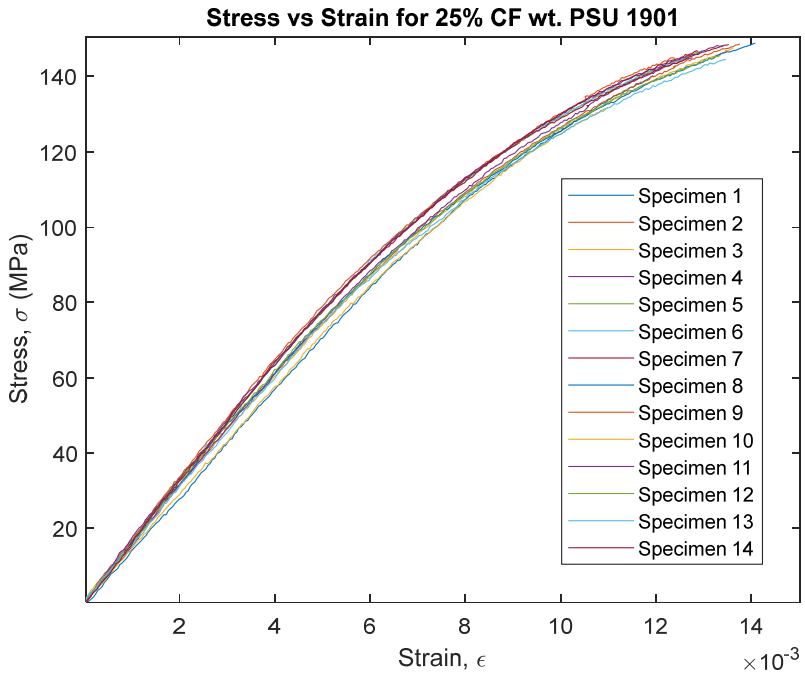

Figure 74. Stress-strain curves of the tensile test in the 1-direction for 25% CF-PSU.

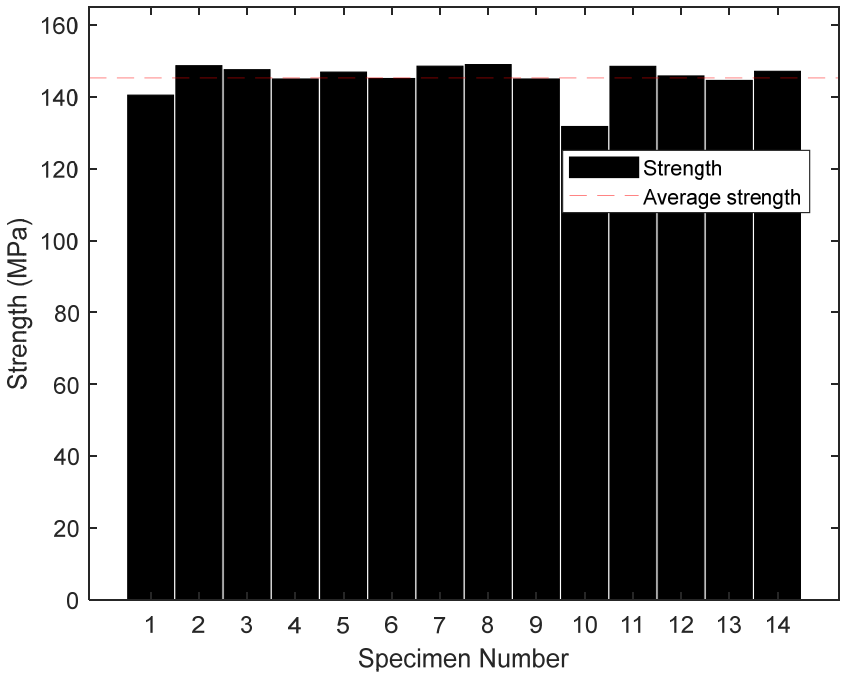

Figure 75. Ultimate strength values in the 1-direction characterized for 25% CF-PSU.

Table 17. Results tensile test in the 1-direction for CF-PSU.

25% CF-PSU Printing Direction Tensile Results			
Sample #	Young's Modulus, E_1 $[GPa]$	Poisson's Ratio, ν_{13}	Ultimate Strength, X_1^u $[MPa]$
1	14.26	0.305	140.40
2	14.97	0.329	148.57
3	15.40	0.332	147.49
4	15.77	0.340	144.89
5	15.74	0.325	146.80
6	15.99	0.339	145.05
7	16.05	0.322	148.46
8	15.68	0.324	148.92
9	16.43	0.370	144.92
10	14.17	0.287	131.67
11	15.38	0.323	148.40
12	16.16	0.329	145.75
13	15.21	0.331	144.51
14	15.65	0.344	147.01
AVG	**15.49**	**0.329**	**145.20**
STDEV	0.64	0.018	4.35

Experimental results for tensile properties of 25% wt. CF-PSU manufactured in the CAMRI system indicate mean values of 15.49 GPa for the Young's Modulus, 0.329 for the Poisson's ratio and 145.2 MPa for the Ultimate Tensile Strength, in the printing direction.

Tensile Properties in the 2-Direction

To measure the tensile properties in 2-direction for 25% wt. CF-PSU, twelve tensile coupons were prepared according to section Specimen Preparation and subjected to the mechanical tensile test procedure as described in section Tensile Properties. The sample orientation is indicated in Figure 76, where 1 is the printing direction and 2 the transverse direction. Figure 77 shows the strain fields of one specimen of the set at different points of the test.

Figure 76. Tensile coupon orientation for the 2-direction characterization.

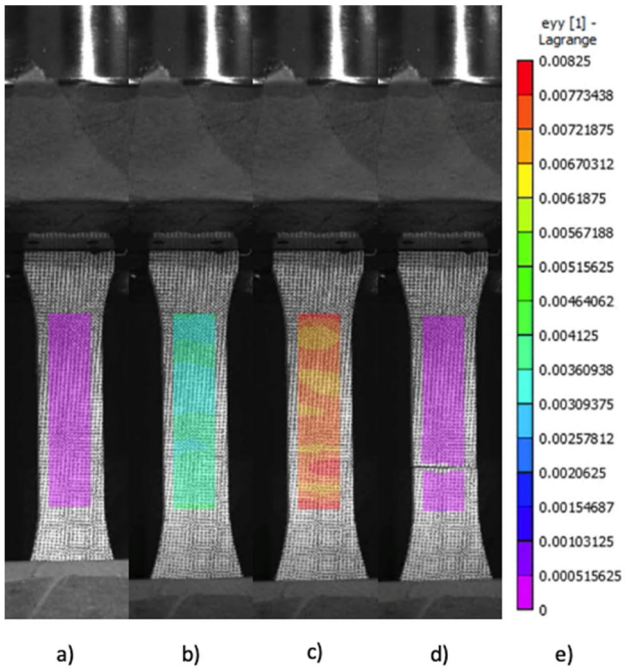

Figure 77. Strain field developed in the loading direction. a) before the load application b) when strains start to develop c) just before failure d) just after failure e) strain field distribution

Figure 78 shows the stress-strain curves obtained out of the data reduction and post-processing analysis for every sample. Figure 79 is a plot of the strength values considered for the mean strength computation of this experimental set. Finally, Table 18 summarizes the results obtained for the Young's Modulus, Tensile Strength and Poisson's ratio obtained.

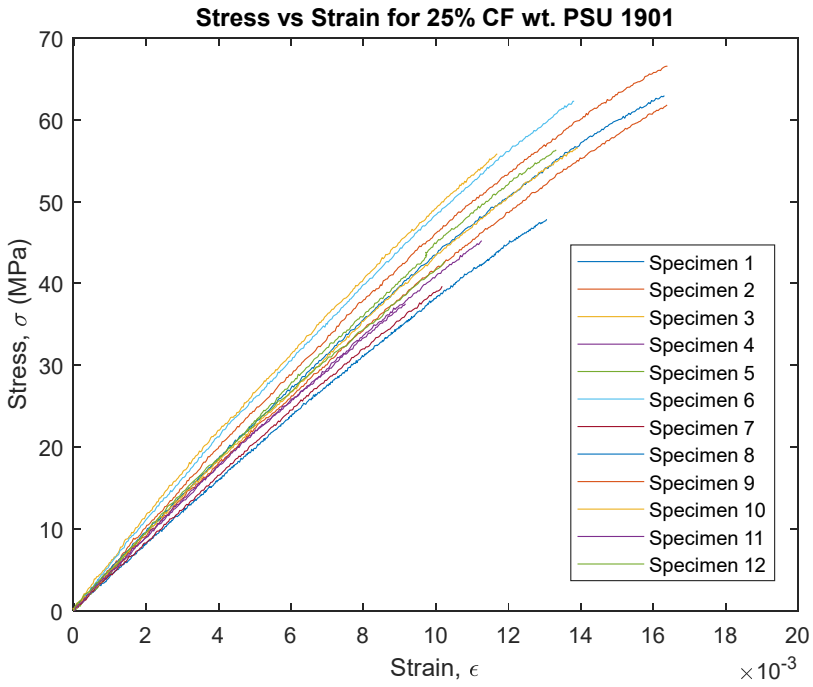

Figure 78. Stress-strain curves of the tensile test in the 2-direction for CF-PSU.

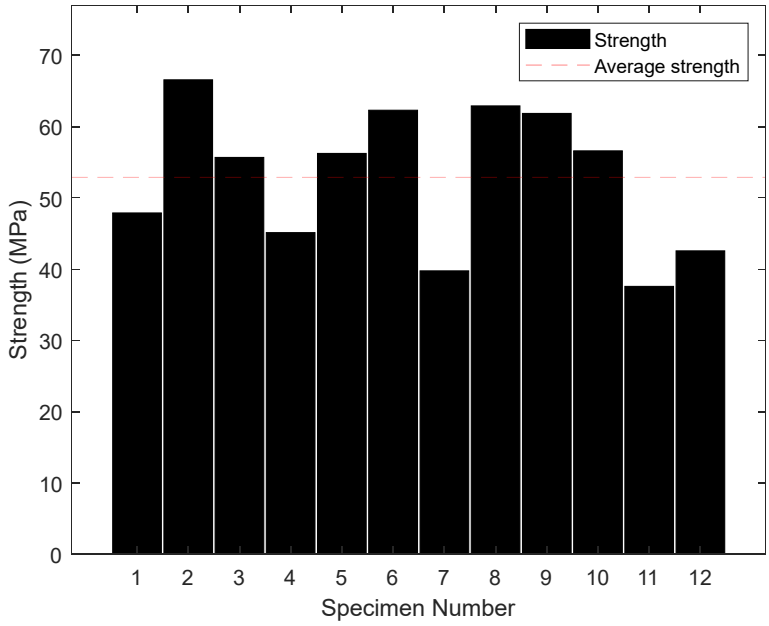

Figure 79. Ultimate strength in the 2-direction for CF-PSU.

Table 18. Results tensile tests in the 2-direction for CF-PSU.

25% CF-PSU Transverse Direction Tensile Results			
Sample #	Young's Modulus, E_2 $[GPa]$	Poisson's Ratio, ν_{21}	Ultimate Strength, X_2^u $[MPa]$
1	3.98	0.140	47.88
2	4.93	0.161	66.57
3	5.51	0.129	55.69
4	4.43	0.149	45.13
5	4.77	0.166	56.24
6	5.20	0.176	62.30
7	4.08	0.109	39.76
8	4.54	0.172	62.93
9	4.51	0.180	61.85
10	4.56	0.153	56.60
11	4.50	0.127	37.57
12	4.83	0.154	42.56
AVG	**4.65**	**0.151**	**52.92**
STDEV	0.41	0.021	9.53

Experimental results for tensile properties of 25% wt. CF-PSU manufactured in the CAMRI system indicate mean values of 4.65 GPa for the Young's Modulus, 0.151 for the Poisson's ratio and 52.92 MPa for the Ultimate Tensile Strength, in the transverse direction.

Tensile Properties in the 3-Direction

To measure the tensile properties in 3-direction for 25% wt. CF-PSU, nine tensile coupons were prepared according to section Specimen Preparation and subjected to the mechanical tensile

test procedure as described in section Tensile Properties. The sample orientation is indicated in Figure 80 , where 1 is the printing direction and 3 the stacking direction. Figure 81 shows the strain fields of one specimen of the set at different points of the test.

Figure 80. Tensile coupon orientation for characterizing tensile properties in the 3-direction.

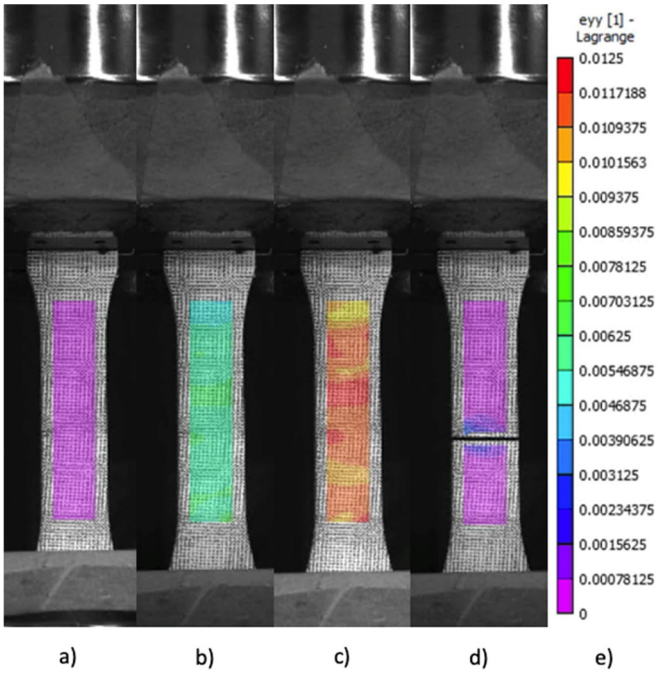

Figure 81. Strain field developed in the loading direction. a) before the load application b) when strains start to develop c) just before failure d) just after failure e) strain field distribution

Figure 82 shows the stress-strain curves obtained out of the data reduction and post-processing analysis for every sample. Figure 83 is a plot of the strength values considered for the mean strength computation of this experimental set. Finally, Table 19 summarizes the results obtained for the Young's Modulus, Tensile Strength and Poisson's ratio obtained.

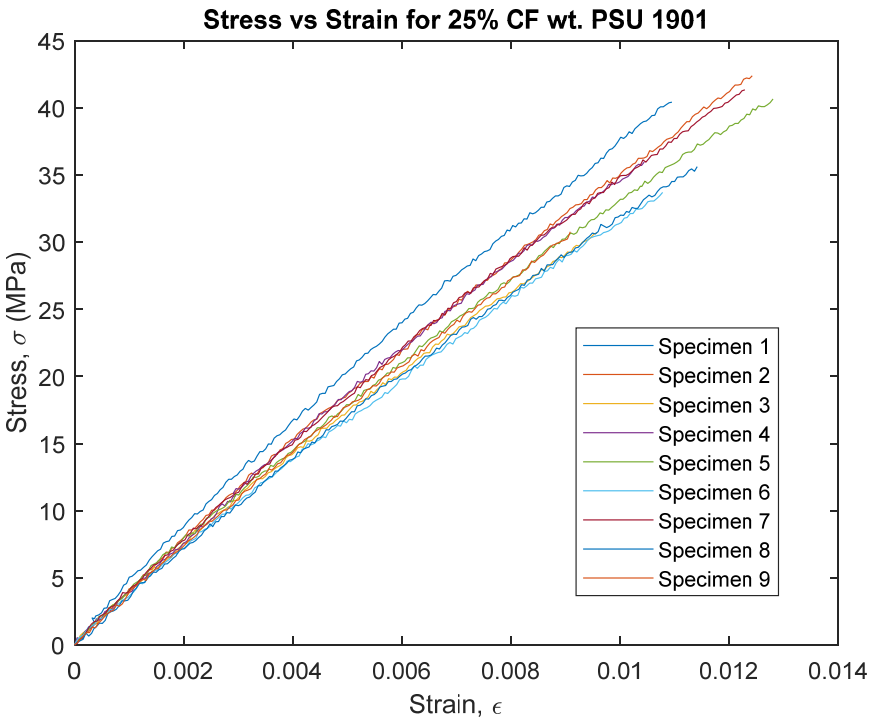

Figure 82. Stress-strain curves of the tensile test in the 3-direction for CF-PSU.

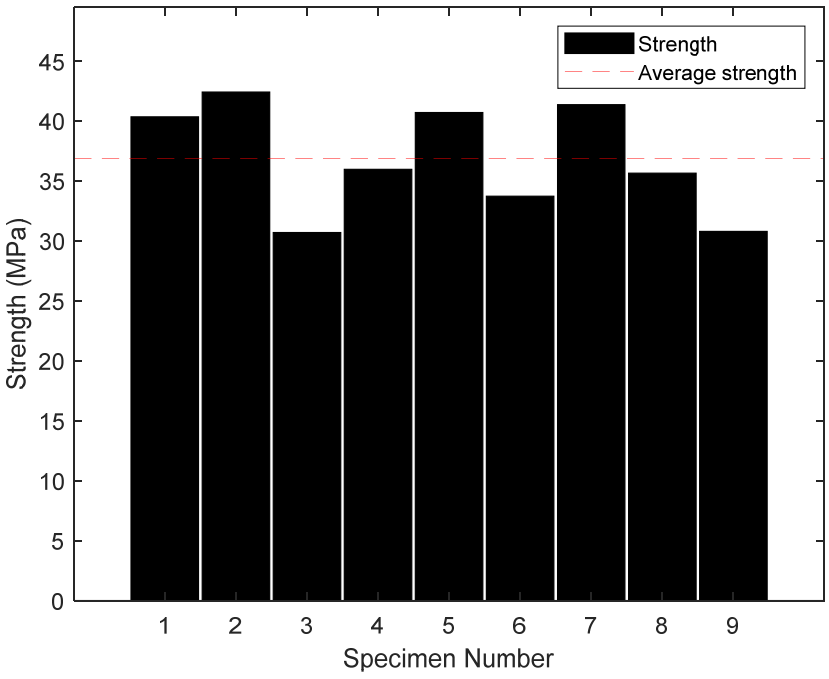

Figure 83. Ultimate strength in the 3-direction for CF-PSU.

Table 19. Tensile test results in the 3-direction for CF-PSU.

25% CF-PSU Stacking Direction Tensile Results			
Sample #	Young's Modulus, E_3 $[GPa]$	Poisson's Ratio, ν_{31}	Ultimate Strength, X_3^u $[MPa]$
1	4.09	0.096	40.35
2	3.81	0.080	42.42
3	3.57	0.080	30.70
4	3.65	0.086	35.97
5	3.48	0.064	40.71
6	3.50	0.082	33.72
7	3.81	0.070	41.36
8	3.35	0.082	35.64
9	3.68	0.063	30.79
AVG	**3.66**	**0.078**	**36.85**
STDEV	0.22	0.011	4.54

Experimental results for tensile properties of 25% wt. CF-PSU manufactured in the CAMRI system indicate mean values of 3.66 GPa for the Young's Modulus, 0.078 for the Poisson's ratio and 36.85 MPa for the Ultimate Tensile Strength, in the stacking direction.

Shear Properties in the 1-3 plane

To measure the shear properties for 25% wt. CF-PSU, seventeen V-notch coupons were prepared with the length along printing direction and height along stacking direction, according to section Specimen Preparation and subjected to the mechanical shear test procedure as described in section Shear Properties. The sample orientation is indicated in Figure 84, where 1 is the printing direction and 3 the stacking direction. Figure 85 shows the strain fields of one specimen of the set at different points of the test.

Figure 84. Shear coupon orientation for the 1-3 plane characterization.

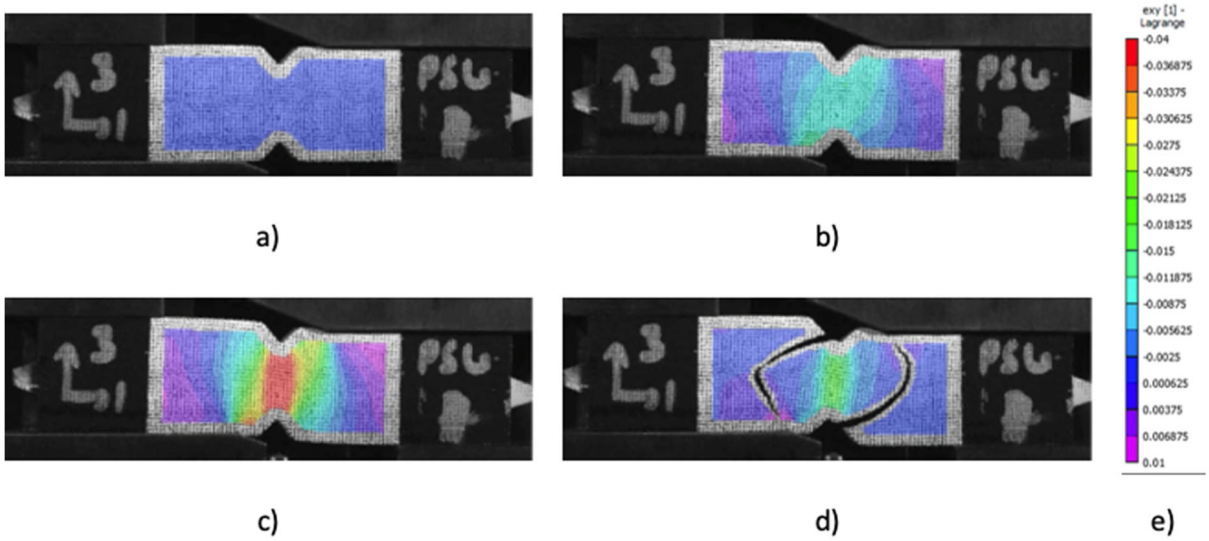

Figure 85. Shear strain field developed during test. a) before the load application b) when strains start to develop c) just before failure d) just after failure e) shear strain field distribution

Figure 86 shows the shear stress-shear strain curves obtained out of the data reduction and post-processing analysis for every sample. Figure 87 is a plot of the shear strength values considered for the mean shear strength computation of this experimental set. Finally, Table 20 summarizes the results obtained for the Shear Modulus and Shear Strength obtained.

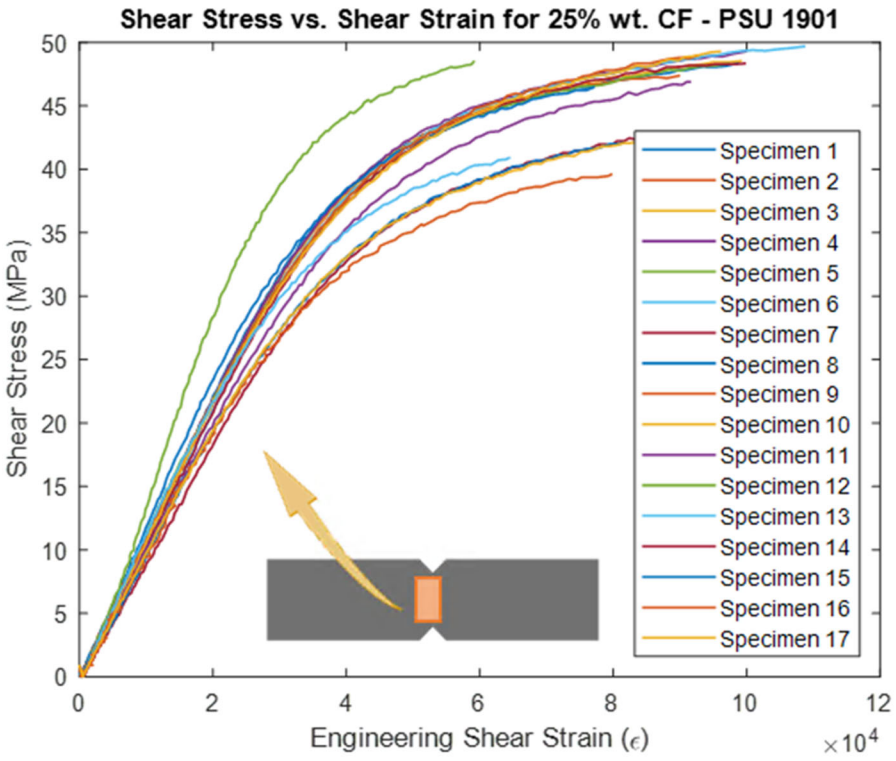

Figure 86. Stress-strain curves of the shear test in the 1-3 plane CF-PSU.

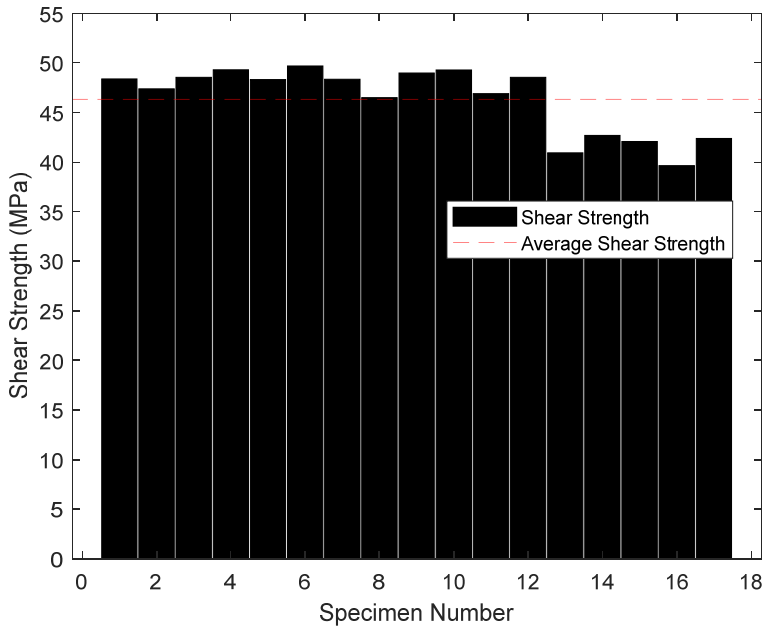

Figure 87. Ultimate shear strength in the 1-3 plane for CF-PSU.

Table 20. Results shear tests in the 1-3 plane for CF-PSU.

25% CF-PSU 1-3 Plane Shear Results		
Sample #	Shear Modulus, G_{13} $[GPa]$	Ultimate Shear Strength, τ_{13}^{u} $[MPa]$
1	1.06	48.38
2	1.08	47.39
3	1.02	48.55
4	1.14	49.31
5	1.12	48.32
6	1.03	49.69
7	1.06	48.35
8	1.20	46.50
9	1.12	48.99
10	1.11	49.29
11	1.07	46.90
12	1.40	48.55
13	1.19	40.93
14	0.93	42.69
15	0.98	42.08
16	1.00	39.64
17	1.03	42.39
AVG	**1.09**	**46.35**
STDEV	**0.11**	**3.36**

Experimental results for shear properties in the 1-3 plane of 25% wt. CF-PSU manufactured in the CAMRI system indicate mean values of 1.09 GPa for the Shear Modulus and 46.35 MPa for the Ultimate Shear Strength.

Thermophysical Properties

An average density of $1.28\,g/cm^3$ was obtained for the CF-PSU based on the density measurements carried out at TPRL for three samples submitted to thermal conductivity measurements. The density measurement is around 7% lower than what is expected from a simply rule of mixtures considering the density of standard carbon fiber and PSU polymer obtained from online databases (MatWeb, www.matweb.com). Such a subtle difference in density can be attributed to variations in the fiber content, a small volume fraction of voids (e.g., <3.5%) entrapped within the printed beads, and errors inherent to the experimental method. The presence of voids within the printed bead (intra-bead voids) is not critical in the application of printed tooling since the voids are small in diameter (e.g., < 25 μm). Furthermore, intra-bead voids are not interconnected to compromise the vacuum integrity of the printed tool. The method used for characterizing the density is described in the section Thermophysical Properties.

Heat Capacity

The heat capacity C_p of the CF-PSU was measured as a function of temperature using the DSC method as previously described in the Heat Capacity section. Figure 88 shows the heat capacity characterized as a function of temperature for the CF-PSU. A discontinuity in the heat capacity occurs at around the glass transition temperature (indicated with vertical dashed lines in Figure 88) which is observed as a smooth transition in Figure 88.

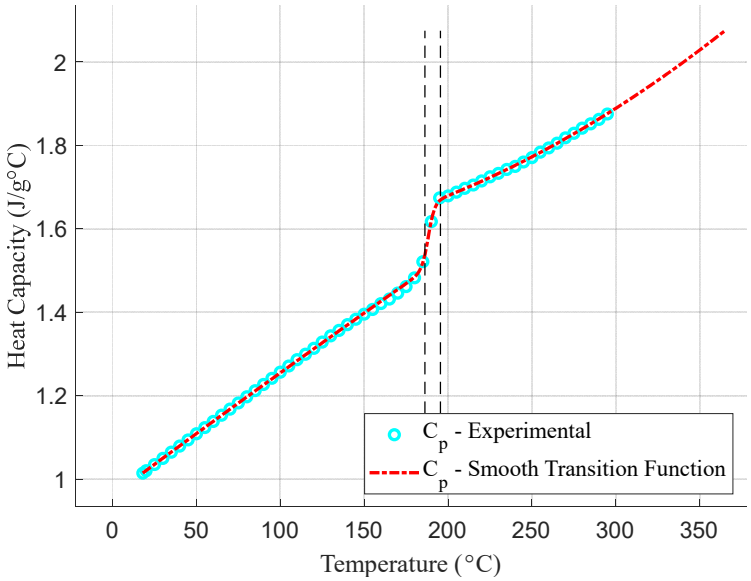

Figure 88. Heat capacity characterized as a function of temperature for the CF-PSU.

A piecewise function with a smooth transition introduced with a sigmoid function (red dashed line in Figure 88) was used to describe the evolution of heat capacity with temperature from the room temperature to the processing temperature of 360 °C. The heat capacity is described as a function of temperature as given by Equation (13). Quadratic functions are used to describe the heat capacity for temperature above ($C_p^{aT_g}$) and below ($C_p^{bT_g}$) the glass transition temperature.

$$C_p(T) = \big(1 - S(T)\big) \cdot C_p^{bT_g}(T) + S(T) \cdot C_p^{aT_g}(T) \tag{13}$$

Table 21 lists the parameters of the quadratic and sigmoid functions that describes the heat capacity of the CF-PSU as a function of temperature.

Table 21. Parameters of piecewise function with a smooth transition used to describe the heat capacity of CF-PSU as a function of temperature.

$C_p(T) = p_1T^2 + p_2T + p_3$			
	$p_1\ (J/g°C^3)$	$p_2\ (J/g°C^2)$	$p_3\ (J/g°C)$
$C_p^{bT_g}\ (J/g°C)$	$-4.854 \cdot 10^{-7}$	$2.987 \cdot 10^{-3}$	$9.61 \cdot 10^{-1}$
$C_p^{aT_g}\ (J/g°C)$	$4.663 \cdot 10^{-6}$	$-2.346 \cdot 10^{-4}$	1.541
$S(T) = 1/(1 + e^{(-(T-C_1)/C_2)})$			
C_1	188.363		

C_2	1.862

Thermal Conductivity

The thermal conductivity was characterized in the three principal material directions for the CF-PSU via the laser flash method as described in the section Thermal Conductivity. The characterization was requested to TPRL from the room temperature to the material processing temperature of 335 °C. However, the measurements were only reliable up to 200 °C since the sample was significantly deformed after crossing the T_g (~186 °C). Figure 89 shows the thermal conductivity as a function of temperature in the three principal material directions for the CF-PSU.

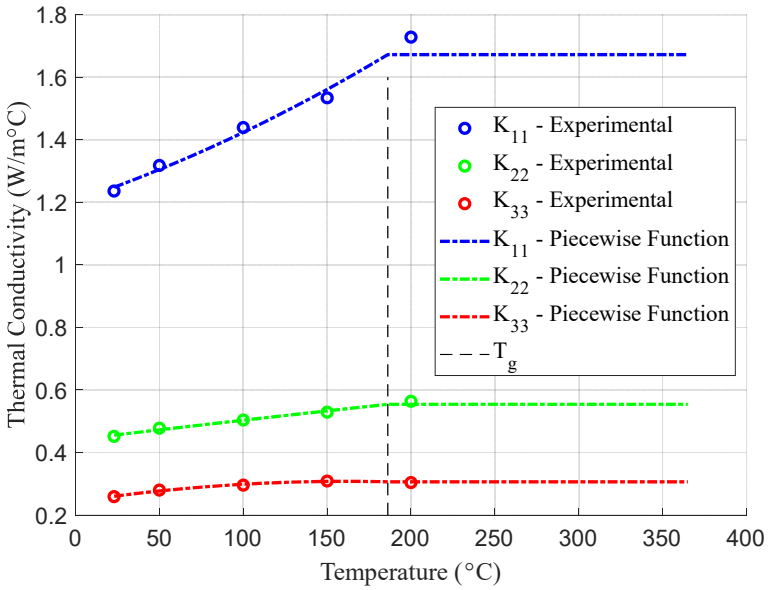

Figure 89. Thermal conductivity as a function of temperature for CF-PSU.

A piecewise function was used to describe the evolution of the thermal conductivity as a function of temperature in the heat transfer analysis of the process simulations. A quadratic function was used to describe the thermal conductivity from the room temperature to the T_g (186 °C) whereas a constant value was assumed beyond that temperature. Table 22 lists the parameters of the piecewise functions used to describe the thermal conductivities of CF-PSU as a function of temperature.

Table 22. Parameters of piecewise functions used to describe thermal conductivities of CF-PSU as a function of temperature.

$K_{ii}(T) = p_1T^2 + p_2T + p_3$			
$T < T_g$	p_1 $(W/m°C^3)$	p_2 $(W/m°C^2)$	p_3 $(W/m°C)$

K_{11} $(W/m°C)$	$3.725 \cdot 10^{-6}$	$1.819 \cdot 10^{-3}$	1.204
K_{22} $(W/m°C)$	$-1.789 \cdot 10^{-7}$	$6.409 \cdot 10^{-4}$	$4.410 \cdot 10^{-1}$
K_{33} $(W/m°C)$	$-2.489 \cdot 10^{-6}$	$8.034 \cdot 10^{-4}$	$2.432 \cdot 10^{-1}$
$T > T_g$			
K_{11} $(W/m°C)$	1.672		
K_{22} $(W/m°C)$	$5.542 \cdot 10^{-1}$		
K_{33} $(W/m°C)$	$3.064 \cdot 10^{-1}$		

Thermomechanical Properties

To measure the thermomechanical properties of 25% wt. CF-PSU, experimental procedure as discussed in section Thermo-mechanical Properties was employed to characterize the coefficient of thermal expansion. One sample was prepared in the 1-2 plane and once sample in the 2-3 plane. Only the data measured below T_g, during the heating cycle of the experiment are reported here, as PSU is an amorphous material. Based on the number of samples prepared, we have data from one sample for characterizing the CTE in the printing and stacking directions, and data from two samples for characterizing CTE in transverse direction.

Figure 90 shows a plot of the variation of thermal strain with temperature for the 1-direction, as recorded from the heated stage during the heated cycle. For strain data below T_g, a linear regression model was used. Based on the regression models fit, the mean value of α_3 below T_g was obtained as $6.23\ \frac{\mu\epsilon}{°C}$.

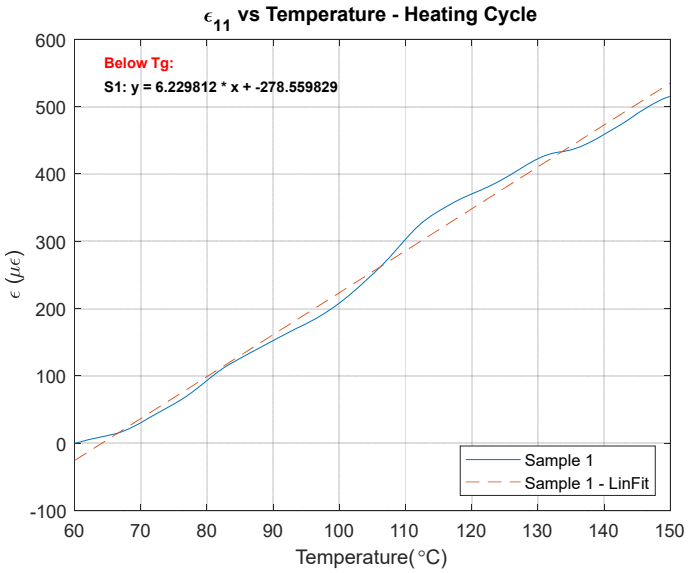

Figure 90. CTE in the 1-direction for CF-PSU.

Figure 91 shows a plot of the variation of thermal strain with temperature for the 2-direction, as recorded from the heated stage during the heated cycle. For strain data below T_g, a linear regression model was used. Based on the regression models fit, the mean value of α_3 below T_g was obtained as $34.79\ \frac{\mu\epsilon}{^\circ C}$.

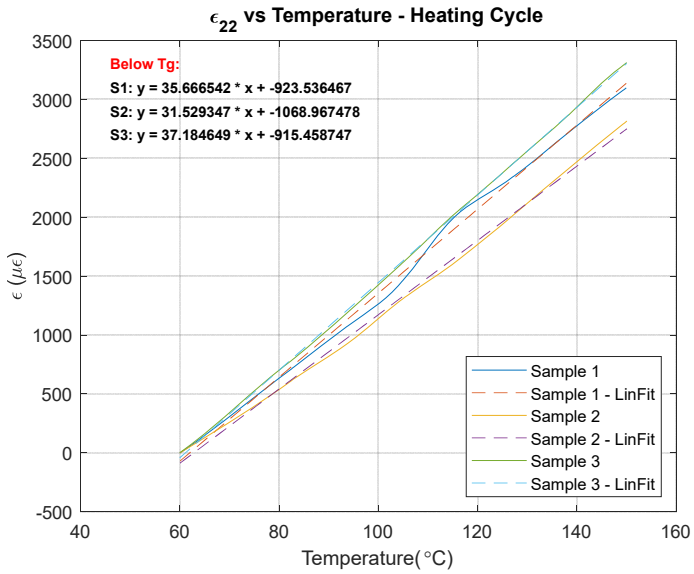

Figure 91. CTE in the 2-direction for CF-PSU.

Figure 92 shows a plot of the variation of thermal strain with temperature for the 3-direction, as recorded from the heated stage during the heated cycle. For strain data below T_g, a linear regression model was used. Based on the regression models fit, the mean value of α_3 below T_g was obtained as $63.44\ \frac{\mu\epsilon}{^\circ C}$.

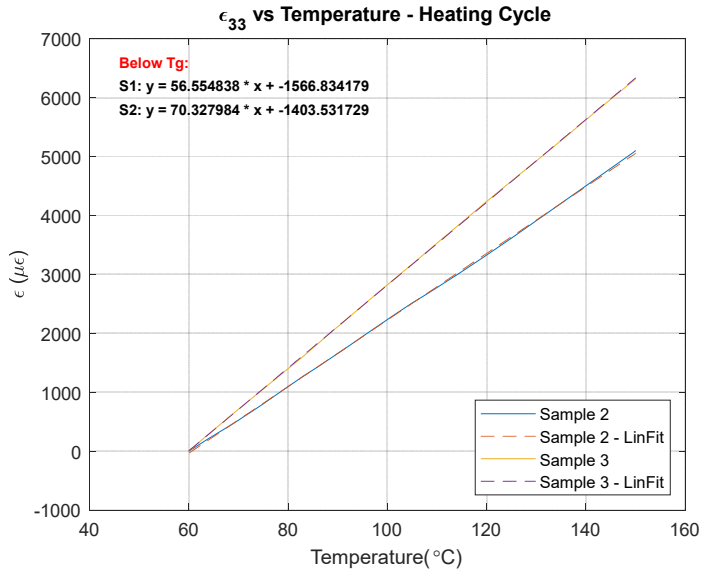

Figure 92. CTE in the 3-direction for CF-PSU.

Table 23. Coefficients of thermal expansion for CF-PSU.

25% CF-PSU Coefficient of Thermal Expansion			
	CTE 1-Direction, α_1 $[\mu\epsilon/°C\ ]$	CTE 2-Direction, α_2 $[\mu\epsilon/°C\ ]$	CTE 3-Direction, α_3 $[\mu\epsilon/°C\ ]$
Below T_g	6.23	34.79	63.44

Thermoviscoelastic Properties

Stress relaxation experiments were carried out with samples of CF-PSU in a DMA model Q800 from TA Instruments© and in a temperature range from 30 °C to 185 °C. Figure 93 shows the stress relaxation experiments carried out in the 1-direction (A) and in the 2-direction for sample of CF-PSU printed in the CAMRI system.

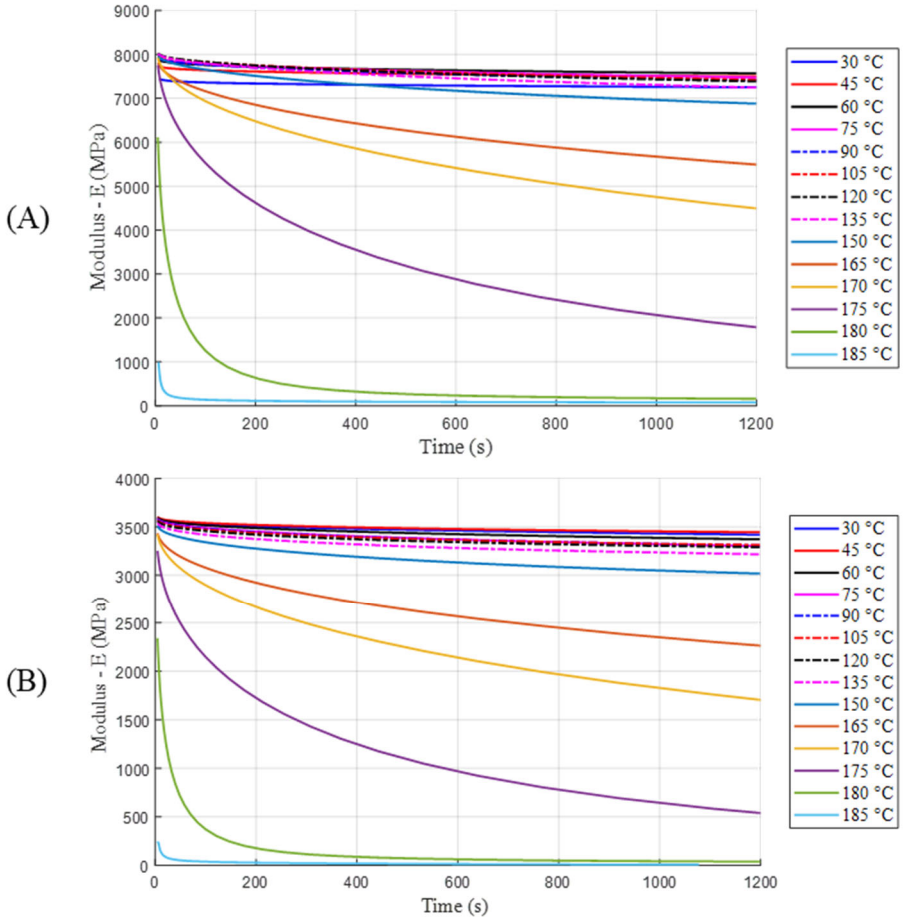

Figure 93: Stress relaxation experiments carried for CF-PSU at multiple temperatures. A) Stress relaxation behavior in the 1-Direction. B) Stress relaxation behavior in the 2-direction.

After characterizing the stress relaxation behavior at different temperatures, master curves were generated by shifting the stress relaxation curves as described in the section Thermoviscoelastic Behavior. Figure 94 A and B shows the master curves generated from the stress relaxation response characterized in the 1 and 2 directions, respectively. Prony series with 14 Maxwell elements were used to fit the master curves in both directions as shown in Figure 94. As a result, the relaxation times were predefined in increments of one decade as discussed in the section Thermoviscoelastic Behavior.

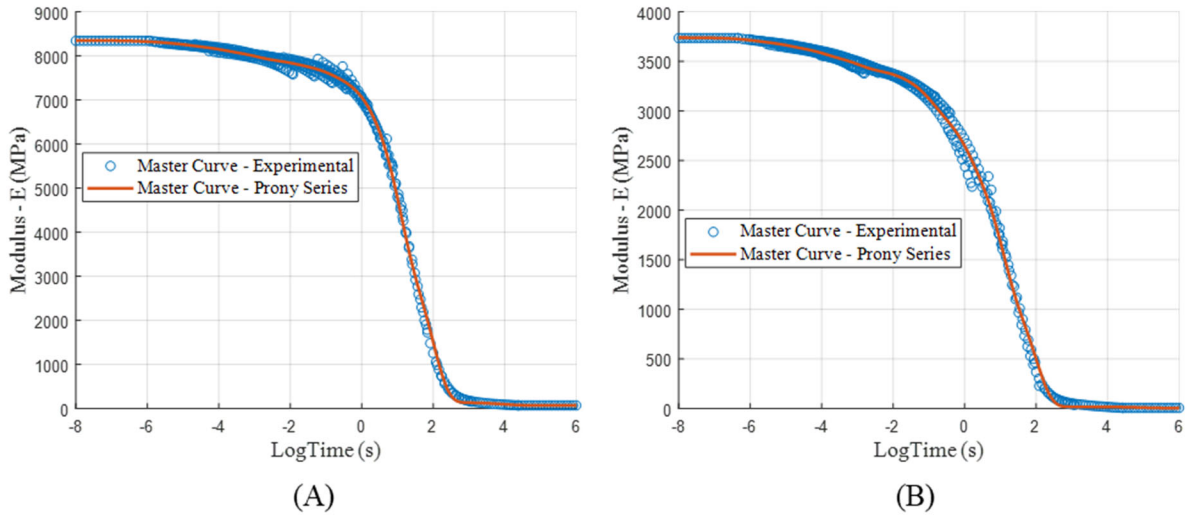

Figure 94: Master curves characterized for the CF-PSU in (A) 1-direction and (B) 2-direction.

The regular and modified WLF equations were used to model the shift factor as a function of temperature. Figure 95 shows the shift factors obtained experimentally and the fit of the WLF equations to the experiments [21].

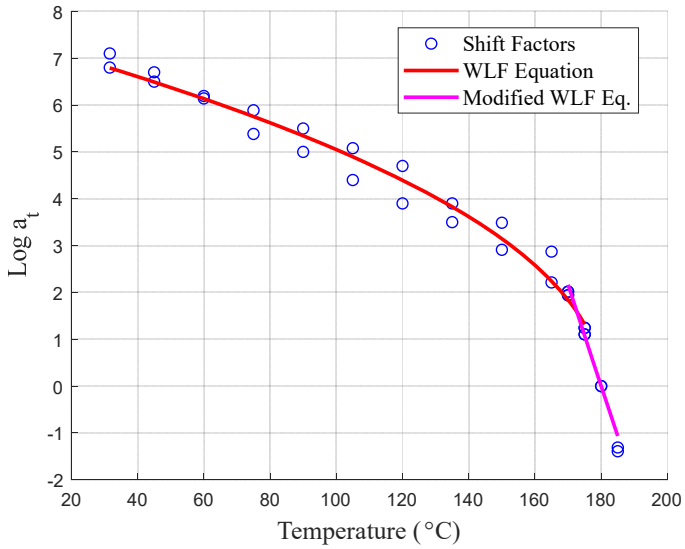

Figure 95. Shift factors and shift factor function characterized for the CF-PSU.

After generating master curves for the fiber dominated material direction (1-direction) and the matrix dominated direction (2-direction), the relaxation functions described through Prony series were normalized. The nine components of the stiffness matrix described through Prony series were generated as described in the section Thermoviscoelastic Behavior. Figure 96 shows the stiffness

components of the stiffness matrix described through Prony series for the CF-PSU printed in the CAMRI system.

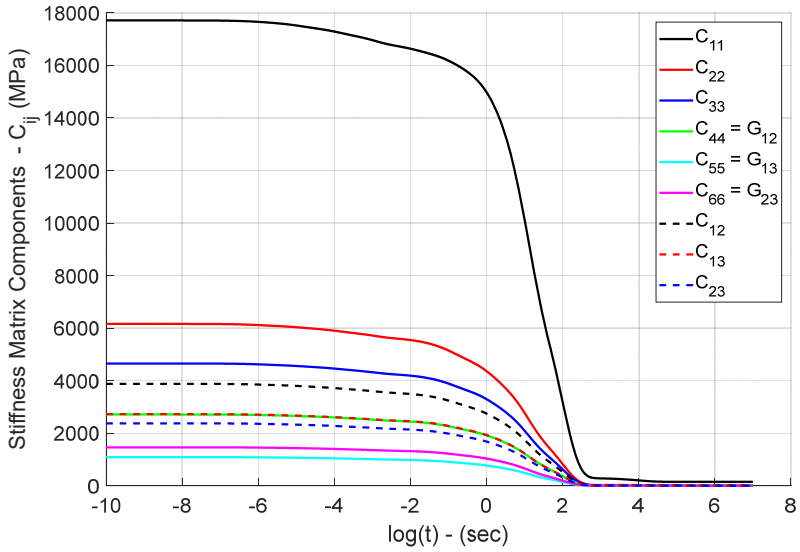

Figure 96. Components of stiffness matrix described through Prony series for the CF-PSU.

Micromechanical Prediction of Material Properties

Once the experimental measurements are carried out, they are used to calibrate a micromechanics model that can predict all the elastic constants of the orthotropic material printed. The calibrated values are given in Table 24. The micromechanics model requires inputs which are not calibrated including the fiber properties and fiber length. The constituent fiber properties were taken from [25] and the fiber aspect ratio was calculated by measuring the fiber length. The fiber length was measured using optical microscopy as described in the section Fiber Length Distribution [26].

Table 24. Reverse engineered values.

Property	Value
Elastic Modulus of Polymer (GPa)	2.129
Poisson's Ratio of Polymer	0.357
$\boldsymbol{a_{11}}$	0.73
$\boldsymbol{a_{22}}$	0.17

Once the properties of the polymer and the microstructure descriptors are determined, the micromechanics model can be used to predict elastic properties of the composite that were not

measured experimentally. The elastic properties predicted from the micromechanics model are given in Table 26.

Table 25. Micromechanics predictions of the elastic constants of the composite.

Composite Elastic Property	Value
$E_1(GPa)$	15.78
$E_2(GPa)$	4.59
$E_3(GPa)$	3.87
$G_{12}(GPa)$	2.54
$G_{13}(GPa)$	1.95
$G_{23}(GPa)$	1.46
ν_{12}	0.42
ν_{13}	0.38
ν_{23}	0.44

25% wt. CF-PESU 1810 3DP

Glass Transition Temperature

The glass transition temperature of the CF-PESU was determined from the drop in storage modulus as described in the section Glass Transition Temperature. Thus, a glass transition temperature of $222.8\,°C$ was determined from the drop in storage modulus characterized via DMA. Figure 97 shows the storage and loss moduli characterized via DMA and the glass transition temperature determined from drop in the storage modulus.

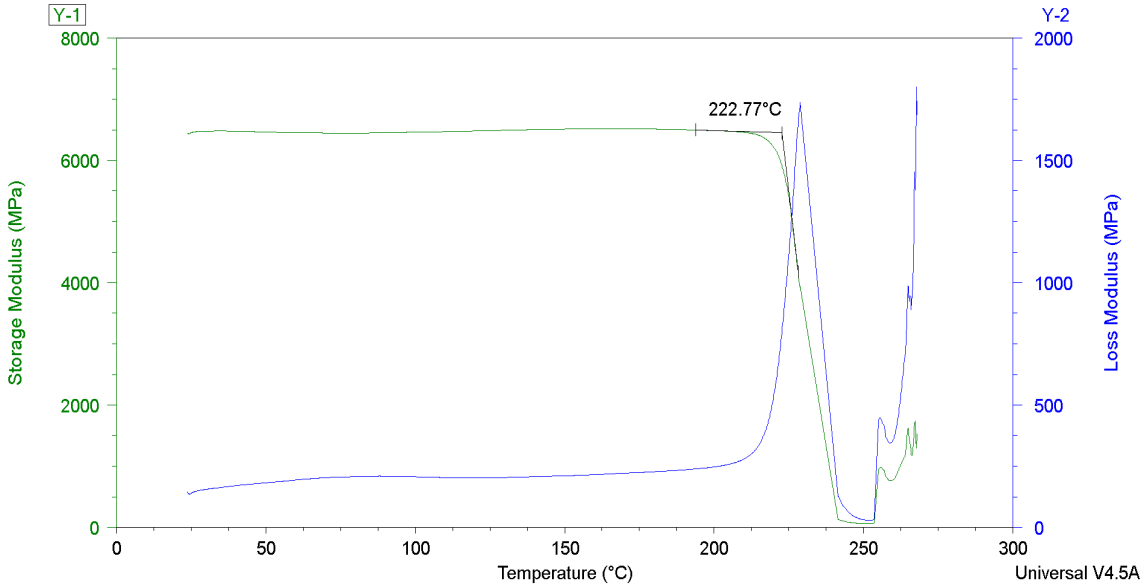

Figure 97. Glass transition temperature of CF-PESU determined from drop in storage modulus.

Microstructural characteristics of material printed in CAMRI

Two microstructural descriptors, namely the fiber length distribution and fiber orientation tensor, were characterized for the beads of 25% CF-PESU printed in the LSAM system. While the fiber length distribution was characterized experimentally, the fiber orientation tensor was characterized virtually.

Fiber Length Distribution

The fiber length distribution was characterized as described in the section Fiber Length Distribution from samples of 25% CF-PESU printed in the CAMRI system. About nine hundred fibers were measured in ImageJ and organized in bins to create a bar plot of the fiber length distribution. Figure 98 shows the fiber length distribution characterized for the material 25% wt. CF-PESU. Additionally, the average number fiber length was computed and yielded a value of 97.5 μm. A fiber diameter of 6 μm was measured via optical microscopy which yields an average number fiber aspect ratio of 16.25.

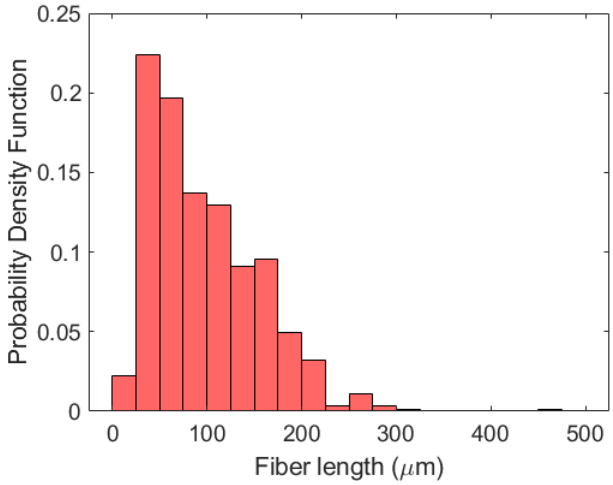

Figure 98. Fiber length distribution characterized for 25% CF-PESU.

Fiber Orientation Tensor

The fiber orientation tensor was reversed engineered with the method outlined in the section Virtual Methods. Table 26 lists the components of the fiber orientation tensor characterized for the material 25% wt. CF-PESU printed in the LSAM system with a nozzle of 12.7 millimeters and with final bead dimensions of $21.08\ mm$ by $5.08\ mm$.

Table 26. Fiber orientation tensor characterized for the material 25% wt. CF-PESU.

Orientation Tensor Component	Value
$\boldsymbol{A_{11}}$	0.58
$\boldsymbol{A_{22}}$	0.29
$\boldsymbol{A_{33}}$	0.13

Mechanical Properties

The mechanical characterization of the CF-PESU was limited to tensile properties in the 1 and 3 directions, the Poisson's ratio in the 1-3 plane, and the shear properties in the 1-3 plane. The additional five properties required in an orthotropic material definition were obtained through micromechanics as outlined in the section Virtual Methods.

Tensile Properties in the 1-direction

To measure the tensile properties in 1-direction for 25% wt. CF-PESU printed in the LSAM, 6 tensile coupons were prepared according to test standard D638 and subjected to the

mechanical tensile test procedure as described in section Tensile Properties. The sample dimensions are indicated in Figure 99, where 1 is the printing direction along the length of the sample and 3 the stacking direction along the width of the sample.

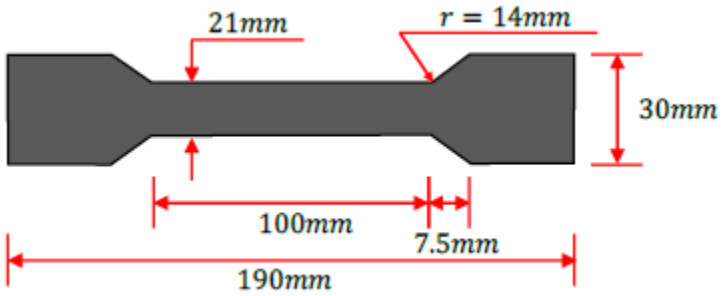

Figure 99. Tensile coupon orientation for the 1-direction characterization

Figure 100 shows the stress-strain curves obtained out of the data reduction and post-processing analysis for every sample. Finally, Table 27 summarizes the results obtained for the Young's Modulus, Tensile Strength and Poisson's ratio obtained.

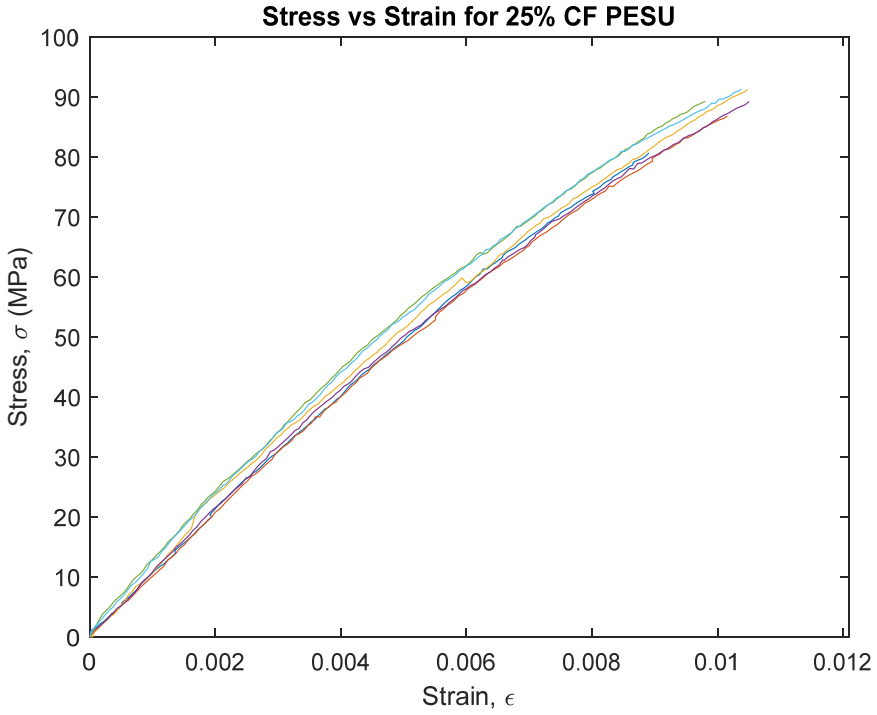

Figure 100. Stress-strain curves of the tensile test in the 1-direction for CF-PESU.

Table 27. Tensile properties in the 1-direction characterized for CF-PESU.

25% CF-PESU 1-Direction Tensile Results			
Sample #	Young's Modulus, E_1 $[GPa]$	Poisson's Ratio, ν_{13}	Ultimate Strength, X_1^u $[MPa]$
1	10.47	0.40	81.02
2	10.40	0.43	87.12
3	11.20	0.43	91.54
4	10.38	0.42	88.95
5	10.48	0.37	89.11
6	10.63	0.48	91.07
AVG	10.59	0.42	88.14
STDEV	0.28	0.04	3.49

Experimental results for tensile properties of 25% wt. CF-PESU manufactured in the LSAM system indicate mean values of 10.59 GPa for the Young's Modulus, 0.42 for the Poisson's ratio and 88.14 MPa for the Ultimate Tensile Strength, in the 1-direction.

Tensile Properties in the 3-Direction

To measure the tensile properties in 3-direction for 25% wt. CF-PESU printed in LSAM, 3 tensile coupons were successfully tested according to test standard D638 and subjected to the mechanical tensile test procedure as described in section Tensile Properties. The sample dimensions are indicated in Figure 101, where 1 is the printing direction along width of the sample and 3 the stacking direction along the length of the sample.

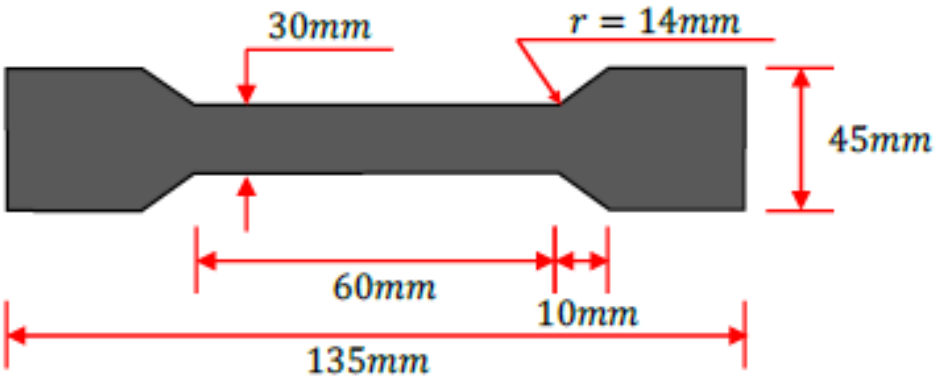

Figure 101. Tensile coupon orientation for 3-direction characterization.

Figure 102 shows the stress-strain curves obtained out of the data reduction and post-processing analysis for every sample. Finally, Table 28 summarizes the results obtained for the Young's Modulus, Tensile Strength and Poisson's ratio obtained.

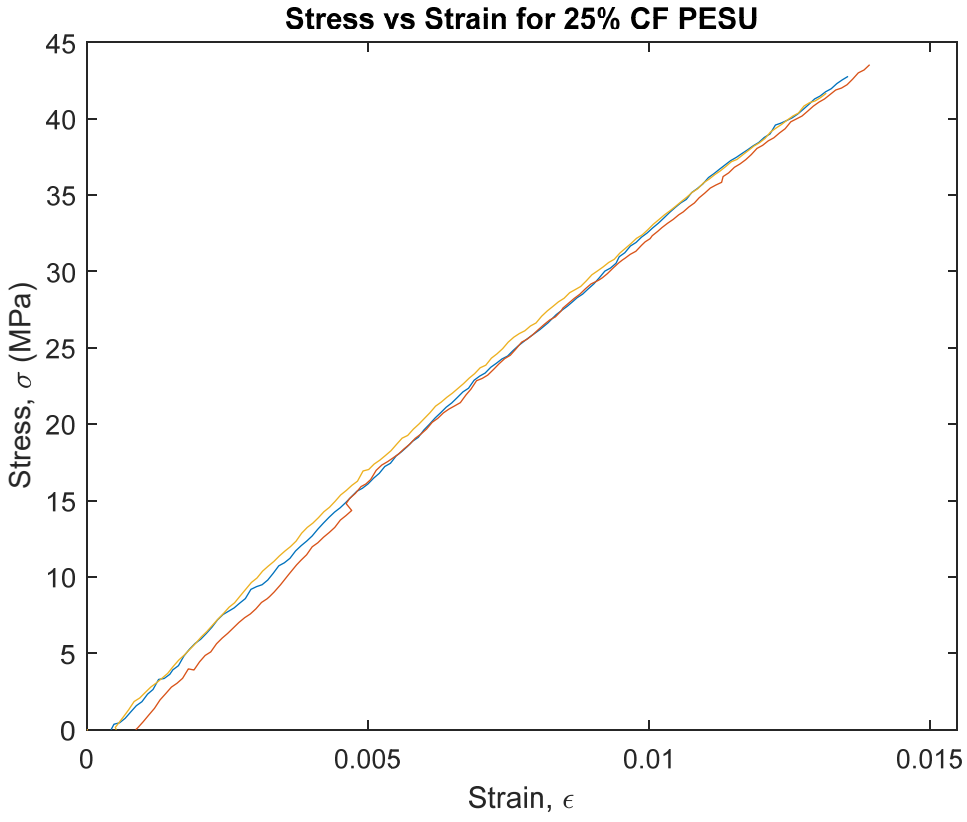

Figure 102. Stress strain plots of CF PESU in the 3-direction.

Table 28. Tensile properties in the 3-direction for CF-PESU.

25% CF-PESU 3-Direction Tensile Results			
Sample #	Young's Modulus, E_3 $[GPa]$	Poisson's Ratio, ν_{31}	Ultimate Strength, X_3^u $[MPa]$
1	3.69	0.16	42.74
2	3.65	0.13	43.52
3	3.84	0.10	41.67
AVG	3.73	0.13	42.64
STDEV	0.10	0.03	0.92

Experimental results for tensile properties in the stacking direction of 25% wt. CF-PESU manufactured in the LSAM system indicate mean values of 3.73 GPa for the Young's Modulus, 0.13 for the Poisson's ratio and 42.64 MPa for the ultimate tensile strength.

Shear Properties in the 1-3 plane

To measure the shear properties for 25% wt. CF-PESU printed in LSAM, 6 V-notch coupons were prepared with the length along printing direction and height along stacking direction and subjected to the mechanical shear test procedure as described in section for Experimental methods. The sample dimensions are indicated in Figure 103.

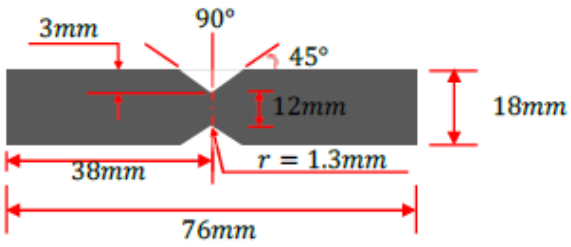

Figure 103. Shear coupon orientation for the 1-3 plane characterization.

Figure 104 shows the shear stress-shear strain curves obtained out of the data reduction

and post-processing analysis for every sample. Finally, Table 29 summarizes the results obtained for the Shear Modulus and Shear Strength obtained.

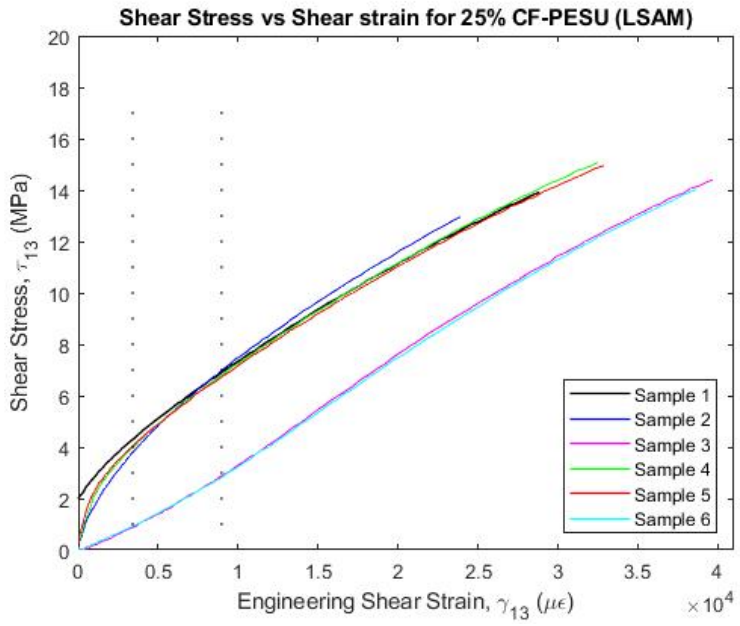

Figure 104. Stress-strain curves of the shear test in the 1-3 plane for 25% CF-PESU.

Table 29. Shear properties in the 1-3 plane for CF-PESU.

25% CF-PESU 1-3 Plane Shear Results		
Sample #	Shear Modulus, G_{13} $[GPa]$	Ultimate Shear Strength, τ_{13}^{u} $[MPa]$
1	0.468	13.9
2	0.585	13.0
3	0.355	14.4
4	0.509	15.1
5	0.491	15.0
6	0.342	14.0
AVG	0.458	14.2
STDEV	0.094	0.782

Experimental results for shear properties in the 1-3 plane of 25% wt. CF-PESU manufactured in the LSAM system indicate mean values of 0.46 GPa for the Shear Modulus and 14.2 MPa for the Ultimate Shear Strength.

Thermophysical Properties

An average density of $1.34\ g/cm^3$ was obtained for the CF-PESU based on the density measurements carried out at TPRL for three samples submitted to thermal conductivity measurements. The method used for characterizing the density is described in the section Thermophysical Properties.

Heat Capacity

The heat capacity C_p of the CF-PESU was measured as a function of temperature using the DSC method as previously described in the Heat Capacity section. Figure 105 shows the heat capacity characterized as a function of temperature for the CF-PSU. A discontinuity in the heat capacity occurs at around the glass transition temperature (indicated with vertical dashed lines in Figure 105) which is observed as a smooth transition in Figure 105.

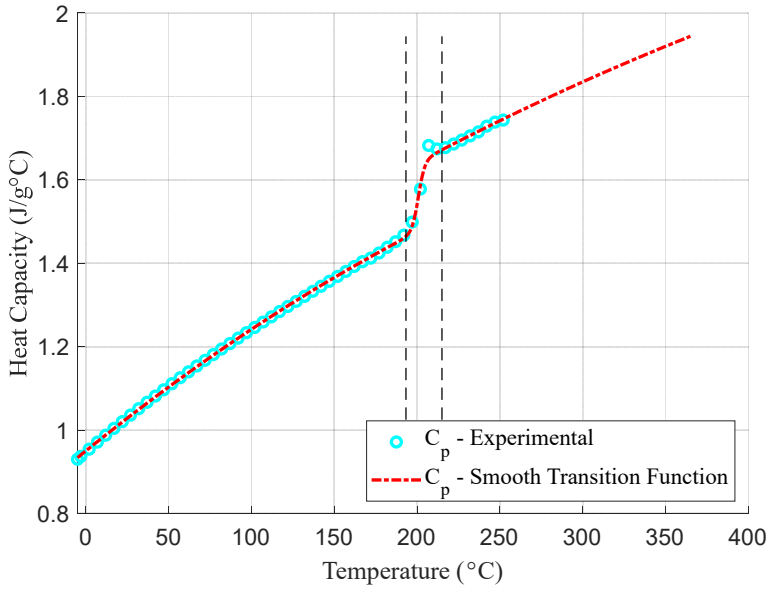

Figure 105. Heat capacity characterized as a function of temperature for the CF-PESU.

A piecewise function with a smooth transition introduced with a sigmoid function (red dashed line in Figure 105) was used to describe the evolution of heat capacity with temperature from the room temperature to the processing temperature of $360\ °C$. The heat capacity is described as a function of temperature as given by Equation (14). Quadratic functions are used to describe the heat capacity for temperature above ($C_p^{aT_g}$) and below ($C_p^{bT_g}$) the glass transition temperature.

$$C_p(T) = \big(1 - S(T)\big) \cdot C_p^{bT_g}(T) + S(T) \cdot C_p^{aT_g}(T) \quad (14)$$

Table 30 lists the parameters of the quadratic and sigmoid functions that describes the heat capacity of the CF-PESU as a function of temperature.

Table 30. Parameters of piecewise function with a smooth transition used to describe the heat capacity of CF-PESU as a function of temperature.

$C_p(T) = p_1T^2 + p_2T + p_3$			
	$p_1\ (J/g°C^3)$	$p_2\ (J/g°C^2)$	$p_3\ (J/g°C)$
$C_p^{bT_g}\ (J/g°C)$	$-2.908 \cdot 10^{-6}$	$3.207 \cdot 10^{-3}$	$9.499 \cdot 10^{-1}$
$C_p^{aT_g}\ (J/g°C)$	$-1.571 \cdot 10^{-6}$	$2.726 \cdot 10^{-3}$	1.158
$S(T) = 1/(1 + e^{(-(T-C_1)/C_2)})$			
C_1	200.777		
C_2	1.893		

Thermal Conductivity

The thermal conductivity was characterized in the three principal material directions for the CF-PESU via the laser flash method as described in the section Thermal Conductivity. The characterization was requested to TPRL from the room temperature to the material processing temperature of 335 $°C$. However, the measurements were only reliable up to 200 $°C$ since the sample was significantly deformed at around the T_g (~222 $°C$). Figure 106 shows the thermal conductivity as a function of temperature in the three principal material directions for the CF-PESU.

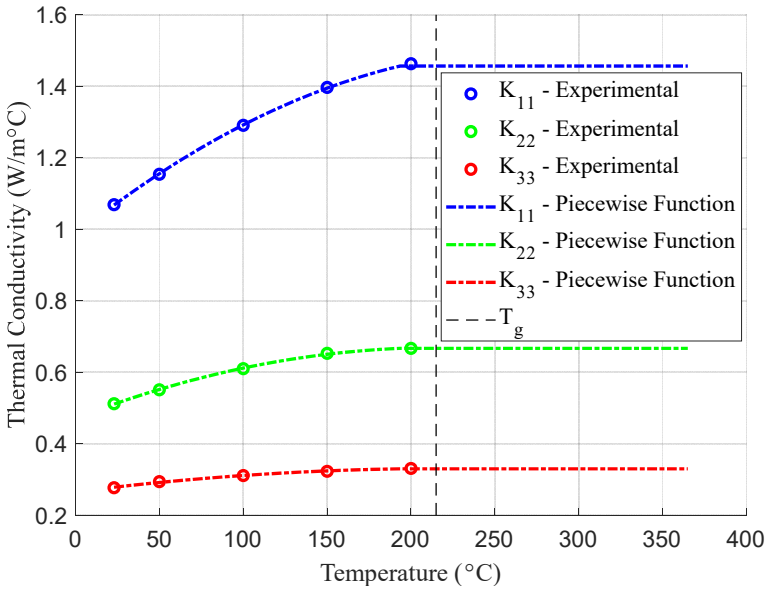

Figure 106. Thermal conductivity as a function of temperature for CF-PESU.

A piecewise function was used to describe the evolution of the thermal conductivity as a function of temperature in the heat transfer analysis of the process simulations. A quadratic function was used to describe the thermal conductivity from the room temperature to the T_g $(222.8\ °C)$ whereas a constant value was assumed beyond that temperature. Table 31 lists the parameters of the piecewise functions used to describe the thermal conductivities of CF-PSU as a function of temperature.

Table 31. Parameters of piecewise functions used to describe thermal conductivities of CF-PESU as a function of temperature.

$K_{ii}(T) = p_1T^2 + p_2T + p_3$			
$T < T_g$	$p_1\ (W/m°C^3)$	$p_2\ (W/m°C^2)$	$p_3\ (W/m°C)$
$K_{11}\ (W/m°C)$	$-6.742 \cdot 10^{-6}$	$3.742 \cdot 10^{-3}$	$9.853 \cdot 10^{-1}$
$K_{22}\ (W/m°C)$	$-4.204 \cdot 10^{-6}$	$1.825 \cdot 10^{-3}$	$4.712 \cdot 10^{-1}$
$K_{33}\ (W/m°C)$	$-1.323 \cdot 10^{-6}$	$5.886 \cdot 10^{-4}$	$2.656 \cdot 10^{-1}$
$T > T_g$			
$K_{11}\ (W/m°C)$	1.45		
$K_{22}\ (W/m°C)$	$6.67 \cdot 10^{-1}$		

$K_{33}\ (W/m°C)$	$3.29 \cdot 10^{-1}$

Thermomechanical Properties

One CTE specimen in the plane 1-2 and one CTE specimen in the plane 2-3 printed with CF-PESU in the LSAM were tested according to the methods discussed in the experimental section. Only the heating cycle of the CTE experiment was considered in the characterization due to warpage of the sample developed at temperatures above the T_g. Specimens in the 1-2 and 2-3 planes produced one data set for characterizing the CTE in the 1-direction, 2 data sets for the CTE in the 2-direction, and one data set for the CTE in the 3-direction. Figure 107 plots the thermal strain in the 1 and 3 directions as a function of the temperature recoded by the heated stage while the sample was heated from the ambient temperature to past the T_g. A linear regression was carried out for the data below the T_g of the PESU to determine the CTE in the 1 and 3 directions.

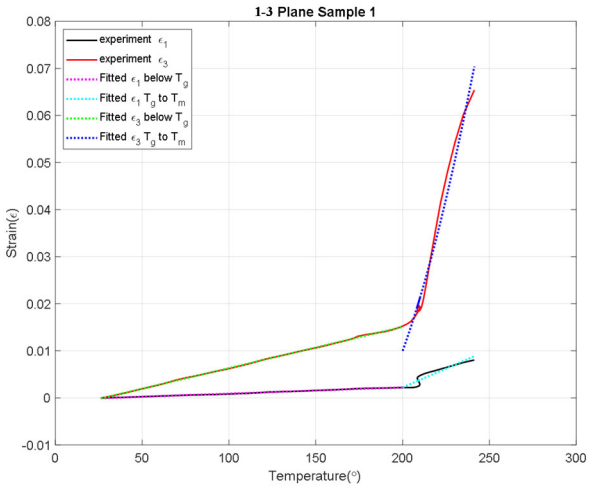

Figure 107. Thermal strains vs temperature in the 1 and 2 directions characterized for CF-PESU.

Figure 108 plots the thermal strain in the 2 and 3 directions as a function of the temperature recoded by the heated stage while the sample was heated from the ambient temperature to past the T_g. A linear regression was carried out for the data below the T_g of the PESU to determine the CTE in the 2 and 3 directions. The CTEs characterized as the slope of the linear regression are summarized in

Table 32.

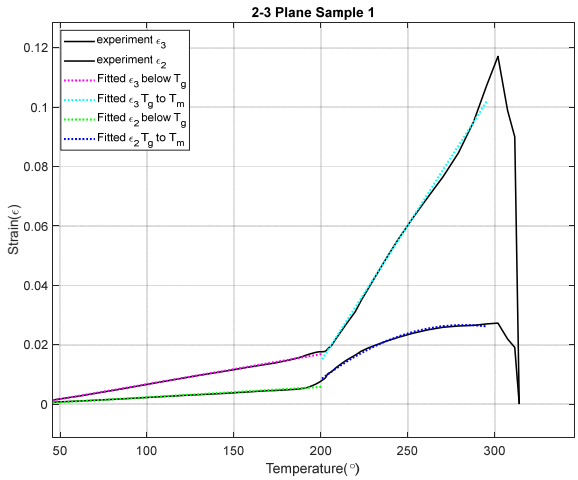

Figure 108. Thermal strains vs temperature in the 2 and 3 directions characterized for CF-PESU.

Table 32. Coefficients of thermal expansion for CF-PESU.

25% CF-PESU Coefficient of Thermal Expansion			
	CTE 1-Direction, α_1 $[\mu\epsilon/°C\ ]$	CTE 2-Direction, α_2 $[\mu\epsilon/°C\ ]$	CTE 3-Direction, α_3 $[\mu\epsilon/°C\ ]$
Below T_g	13.3	34.6	87.6

Thermoviscoelastic Properties

Stress relaxation experiments were carried out with samples of CF-PESU in a DMA model Q800 from TA Instruments© and in a temperature range from $30\ °C$ to $220\ °C$. Figure 109 shows the stress relaxation experiments carried out in the 1-direction (A) and in the 2-direction for sample of CF-PESU printed in the LSAM system.

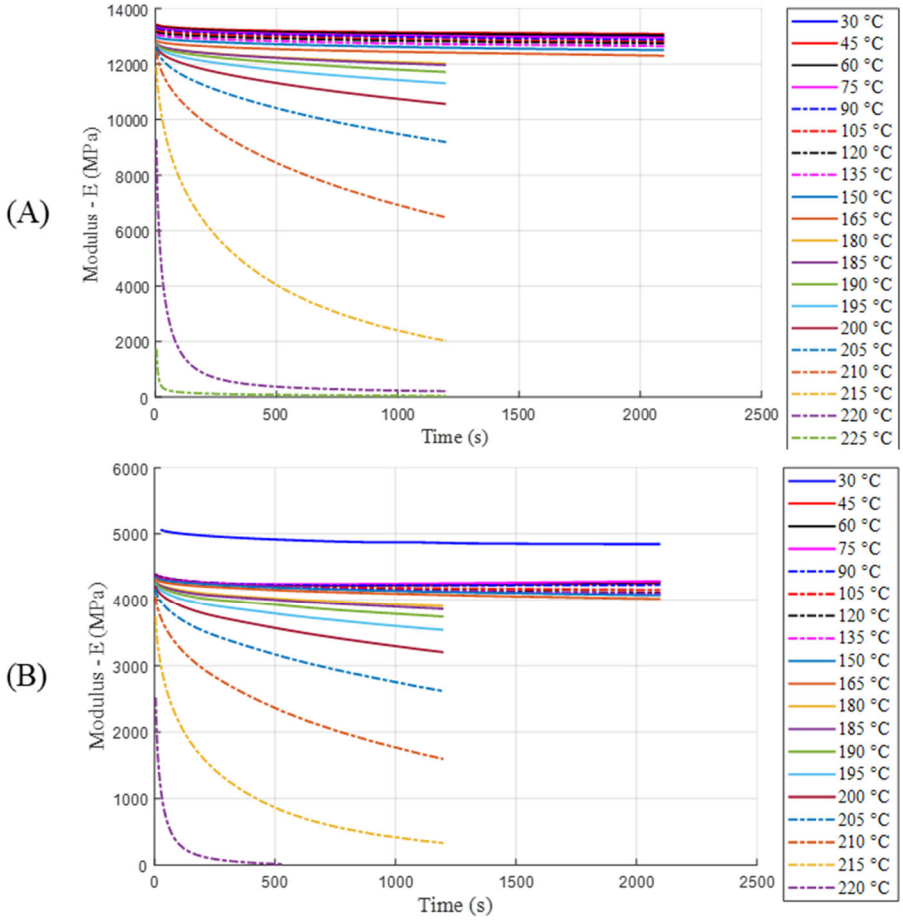

Figure 109: Stress relaxation experiments carried for CF-PESU at multiple temperatures. A) Stress relaxation behavior in the 1-Direction. B) Stress relaxation behavior in the 2-direction.

After characterizing the stress relaxation behavior at different temperatures, master curves were generated by shifting the stress relaxation curves as described in the section Thermoviscoelastic Behavior. Figure 110 A and B shows the master curves generated from the stress relaxation response characterized in the 1 and 2 directions, respectively. Prony series with 14 Maxwell elements were used to fit the master curves in both directions as shown in Figure 110. As a result, the relaxation times were predefined in increments of one decade as discussed in the section Thermoviscoelastic Behavior.

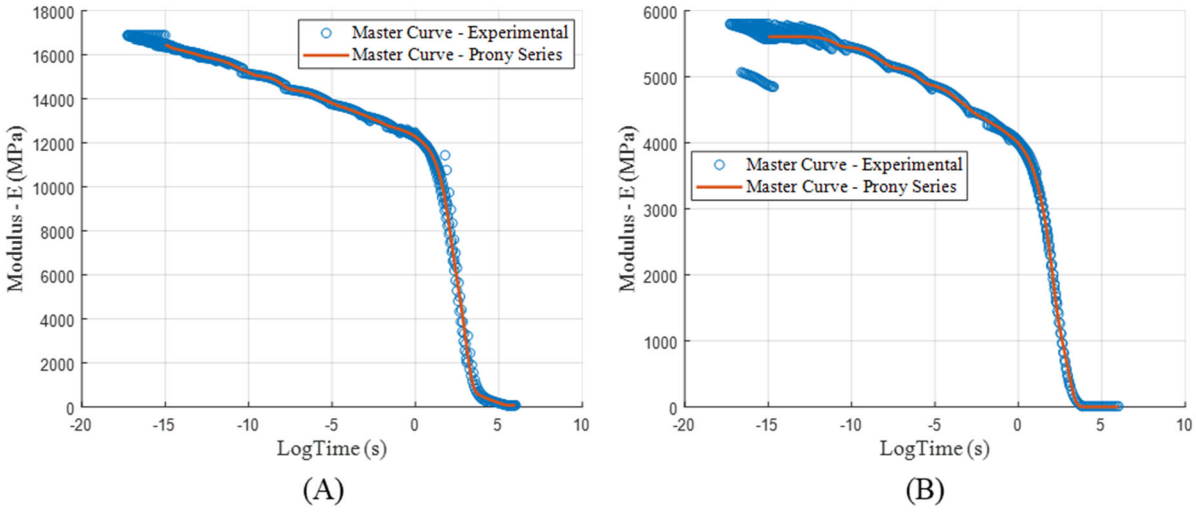

Figure 110: Master curves characterized for the CF-PESU in (A) 1-direction and (B) 2-direction.

The regular and modified WLF equations were used to model the shift factor as a function of temperature. Figure 111 shows the shift factors obtained experimentally and the fit of the WLF equations to the experiments [21].

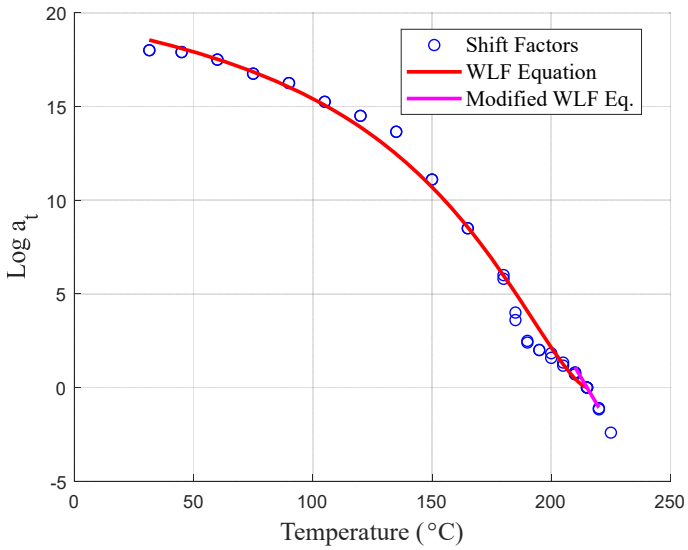

Figure 111. Shift factors and shift factor function characterized for the CF-PESU.

After generating master curves for the fiber dominated material direction (1-direction) and the matrix dominated direction (2-direction), the relaxation functions described through Prony series were normalized. The nine components of the stiffness matrix described through Prony series were generated as described in the section Thermoviscoelastic Behavior. Figure 112 shows the stiffness

components of the stiffness matrix described through Prony series for the CF-PESU printed in the LSAM system.

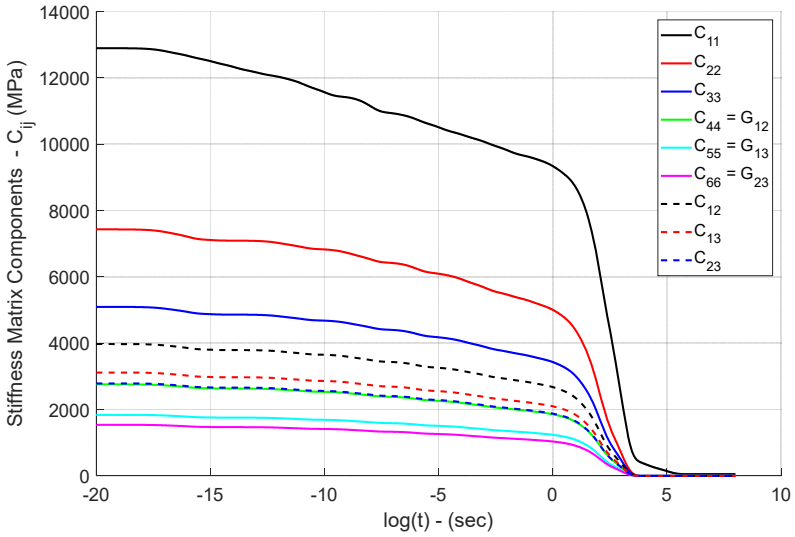

Figure 112. Components of stiffness matrix described through Prony series for the CF-PESU.

Micromechanical Prediction of Material Properties

Once the experimental measurements are carried out, they are used to calibrate a micromechanics model that can predict all the elastic constants of the orthotropic material printed. The calibrated values are given in Table 33. The micromechanics model requires inputs which are not calibrated including the fiber properties and fiber length. The constituent fiber properties were taken from [25] and the fiber aspect ratio was calculated by measuring the fiber length. The fiber length was measured using optical microscopy as described in the section Fiber Length Distribution [26].

Table 33. Reverse engineered values.

Property	Value
Elastic Modulus of Polymer (GPa)	1.80
Poisson's Ratio of Polymer	0.38
$\boldsymbol{a_{11}}$	0.58
$\boldsymbol{a_{22}}$	0.29

Once the properties of the polymer and the microstructure descriptors are determined, the

micromechanics model can be used to predict elastic properties of the composite that were not measured experimentally. The elastic properties predicted from the micromechanics model are given in Table 34.

Table 34. Micromechanics predictions of the elastic constants of the composite.

Composite Elastic Property	Value
$E_1(GPa)$	10.55
$E_2(GPa)$	5.52
$E_3(GPa)$	3.84
$G_{12}(GPa)$	2.75
$G_{13}(GPa)$	1.84
$G_{23}(GPa)$	1.54
ν_{12}	0.38
ν_{13}	0.40
ν_{23}	0.44

Additive Manufacturing Process Simulations

This section presents experimental validation of simulation predictions with ADDITIVE3D© for the three material cards generated in this program, namely CF-PPS, CF-PSU, and CF-PESU. Two geometries were used for validating simulation predictions against experimental measurements. Simulations with material cards for CF-PPS and CF-PSU were validated in the CAMRI system at Purdue, whereas the CF-PESU was validated in the LSAM at Thermwood Corporation.

Geometries for Validating Process Simulation

Two geometries were designed, printed, and measured for validating predictions of the time-temperature history and deformation made with ADDITIVE3D©. Material cards developed for the CF-PPS and CF-PSU were validated with geometries printed in the CAMRI system, whereas the material card for CF-PESU was validated with geometries printed in the Thermwood LSAM.

The geometries were designed with the following considerations. A flat plate with an antisymmetric print orientation was designed to develop significant out-of-plane deformation due to stresses induced by the anisotropy of the printed material and by the temperature gradients developed during the printing process. Further, geometries with flat surfaces are preferred since these are less susceptible to error in the measurement of deformation. In other words, the scalloped surface introduced with the rounded ends of the printed beads can obscure the measurements of

deformation, which is circumvented by using a simple flat plate. A second geometry called 'curved wedge' was designed with a vertical wall to facilitate monitoring the temperature-time history with a thermal camera throughout and posterior to the printing process.

For the flat plate and curved wedge printed in the CAMRI, a substrate made from aluminum with a layer of thermosensitive adhesive (contact adhesive) was used as a printing substrate, whereas a beadboard [27] was used for printing with CF-PESU in the LSAM. A thermal camera FLIR® A655SC was used for monitoring the temperature evolution during the print. The thermal camera is calibrated for two different ranges of temperature, namely from $-40\,°C$ to $150\,°C$ and from $150\,°C$ to $650\,°C$. Thus, the temperature calibration was changed as the printed geometries cooled down to below $150\,°C$. Cameras were used for recording a video of the printing process. Beads with dimensions of 6.15 by 1.5 mm were printed in the CAMRI system whereas beads with dimensions of 20.32 by 5.08 mm were printed in the LSAM.

Flat Plate

The first geometry is a flat plate with a layup (layer stack) consisting of two layers oriented at 0° followed by two layers oriented at 90°, $[0_2 90_2]$. The unsymmetrical and unbalanced configuration of this layup leads to bending-twisting coupling in the response of the plate to deformation. The chosen layup produces an anticlastic curvature that depends on the mismatch in CTE of the printed material along the directions parallel and transverse to the print. Further, thermal stresses resulting from temperature gradients developed in the plane of printing also affect the anticlastic curvature developed in the plate. Hence, the flat plate is a suitable geometry for validating the predictions for deformation since deformation occurs on flat surfaces that can be readily measured with a laser scanner.

Figure 113 shows the CAD geometry of the flat plate printed with four layers. The dimensions of the plate printed in CAMRI were 150 mm, 150 mm, and 6 mm in width, length, and thickness, respectively. Similarly, the dimensions of the plate printed in the LSAM were 508 mm, 508 mm, and 20.32 mm in width, length, and thickness, respectively.

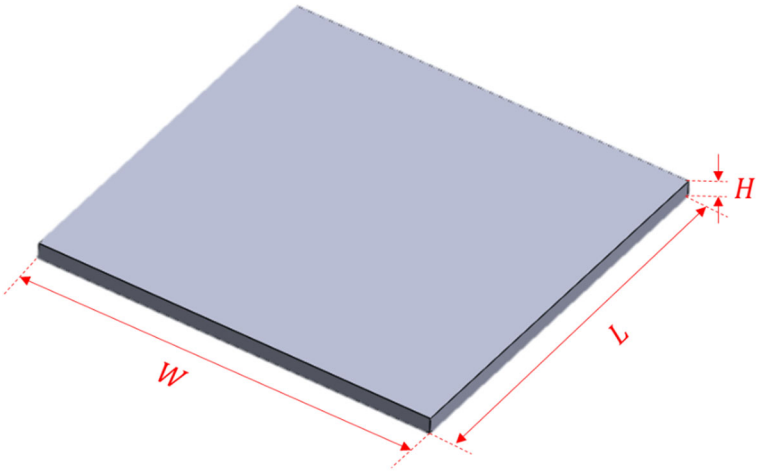

Figure 113. CAD geometry of the four-layer plate.

Figure 114 shows the second and third layers generated after slicing the plate with the commercial slicer Simplify3D©. The four layers share the same starting point.

Table 35 summarizes the process conditions used for printing the plate geometry. It should be noted that the automatic layer time control was used in the LSAM with a target layer time of two minutes. As result, the print speed was automatically adjusted around the value shown in

Table 35 by the LSAM controller. Furthermore, the part printed in the LSAM was removed from the bead board after cooling down to the ambient temperature (~after around 60 min).

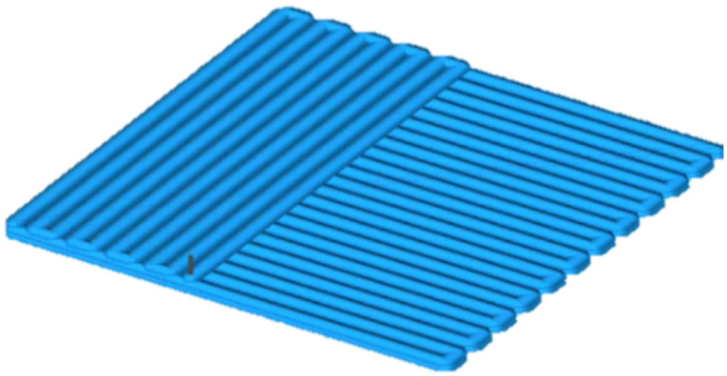

Figure 114. Flat plate slicing of layer 3 with Simplify 3D.

Table 35. Process conditions used for printing plate in CAMRI.

Process Conditions	50% wt. CF-PPS	25% wt. CF-PSU	25% wt. CF-PESU
Print Speed ($\boldsymbol{mm/min}$)	6000	6000	11350*
Extrusion Temperature ($°\boldsymbol{C}$)	317	366	361
Melt Pump Temperature ($°\boldsymbol{C}$)	314	370	390
Nozzle Temperature ($°\boldsymbol{C}$)	320	370	395
Time for cooling after printing part ($\boldsymbol{min}$)	5	5	60
AM System	CAMRI	CAMRI	LSAM

Figure 115 shows the experimental setup in the CAMRI which includes a thermal camera and a video camera (not shown in the figure). The thermal camera was configured to record the temperature of the top surface of the part at 10 Hz and was located at approximately $0.6\ m$ from the plate. Finally, the video camera recorded the entire printing process of the part. A similar setup was implemented in the LSAM to record the temperature history during the printing process of the plate.

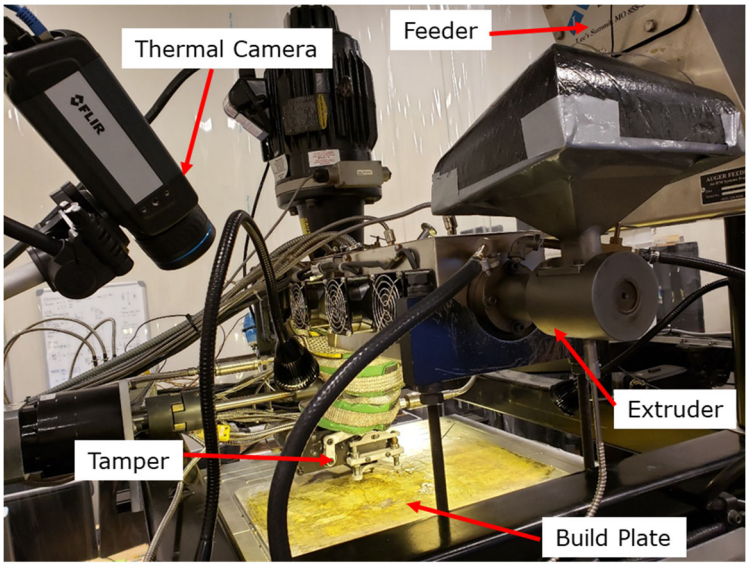

Figure 115: Experimental setup used in the printing experiment of the plate in CAMRI.

As the plate was printed, residual stresses developed due to temperature gradients developed through the thickness and across the plate and to the anisotropy of the printed material, thereby giving rise to gradually debonding of the printed plate from the build sheet. The removal of the part from the substrate allowed the deformation of the printed plate. The top surface of the printed plate was scanned using a laser Faro® arm after the part was cooled to the room temperature and the maximum deformation was developed. The top surface was chosen since it is the smoothest surface. The bottom surface is generally rougher because of the adhesive coatings on the aluminum build plate and the pellets used in the beadboard. Figure 116 shows an example of a point cloud scanned from the bottom surface of a printed plate.

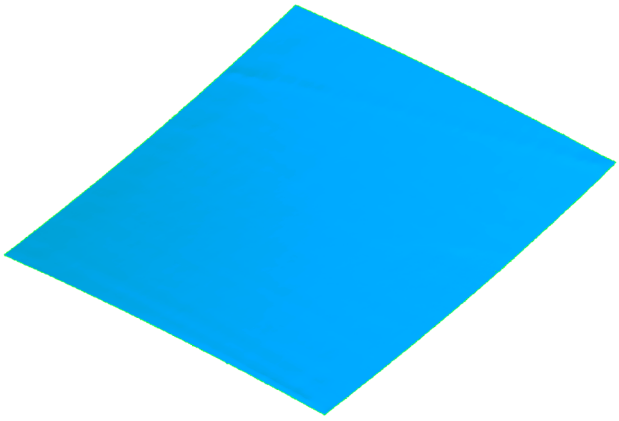

Figure 116. Example of point cloud scanned from the top surface of the printed plate.

Inputs for Additive Process Simulation of Flat Plate

A voxel FE mesh was generated based on the event series of the flat plate. Thus, elements are only present where the print head deposits material. Beads were discretized with two elements in the width and two in the height which led to elements with dimensions of 3.075 mm in width and 0.75 mm in height for the plates printed in CAMRI. Similarly, beads printed in the LSAM were discretized with two elements in the width and two in the height which led to elements with dimensions of 10.51 mm in width and 2.54 mm in height. Linear brick elements type DC3D8 and C3D8 were used in the heat transfer and mechanical analysis respectively [28].

A total of 16,192 and 23,760 finite elements were used to represent the geometry of the plate printed in the CAMRI and LSAM, respectively. To capture the failure process of the thermosensitive adhesive bonding the plate to the aluminum substrate in CAMRI, a cohesive contact was defined between the bottom surface of the printed part and the substrate. The substrate was included only in the mechanical analysis and was modeled as an analytical rigid surface. This approach considers debonding of the part from the substrate. Figure 117-A shows the FE mesh generated for the plate and the analytical rigid surface for the substrate. To capture the interaction of the plate with the beadboard in the LSAM process, the bead board was modeled explicitly, and a cohesive contact was defined between the bottom surface of the printed part and the substrate. Figure 117-B shows the FE mesh generated for the plate and the bead board.

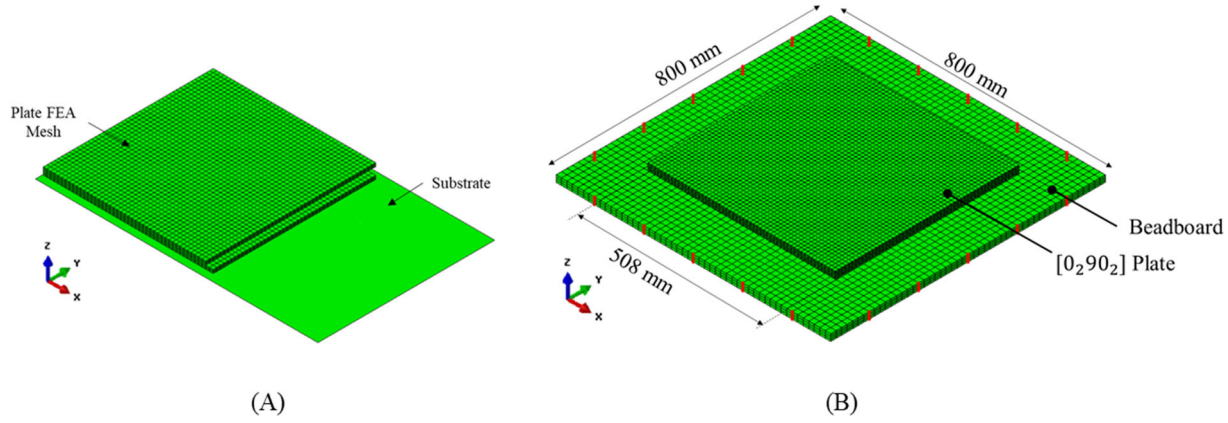

Figure 117: Voxel FEA mesh generated for the plate geometry. A) Plate printed in the CAMRI system. B) Plate printed in the LSAM and on top of beadboard.

The material properties reported in the section Material Characterization were used in the simulation of the EDAM process. To simulate the material in the molten state prior to deposition, the temperature of the nodes in the FEA mesh were initialized to the melt temperature. The bottom

surface of the plate is set to the temperature of the build plate for CAMRI, whereas an adiabatic boundary condition was considered at the bottom of the beadboard. The convection conditions developed at the surface of the plate were governed by a correlation equation that provides a local convection coefficient [3]. The heat removed with the compacter was measured experimentally [3]. Finally, the emissivity and the ambient temperature for radiation were calibrated based on the printing experiments. Similarly, the emissivity of the material can be determined using a black body cavity printed with the same material [3]. The constitutive behavior of the cohesive contact defined between the bottom surface of the printed part and the substrate was also informed based on previous investigations [29]. The substrate was assumed to fail dominantly under mode-I loading. Thus, a maximum stress failure initiation criterion and a displacement-based damage evolution law were used to describe the initiation and evolution of the debonding process, respectively. Table 36 lists the parameters related to the process and to the material used in the simulation of the EDAM process of the plate.

Table 36. Parameters of the process and material used in the simulation of the printing process of the plate.

Parameter	50% wt. CF-PPS	25% wt. CF-PSU	25% wt. CF-PESU
Extrusion Temperature ($°C$)	317	366	360
Deposition speed (mm/min)	6000	6000	11350
Build Plate Temperature ($°C$)	145	145	-
Ambient Temperature Convection ($°C$)	35	50	35
Ambient Temperature Radiation ($°C$)	200	115	35
Heat Removed with compacter (W)	8.0	8.0	80
Emissivity - ε	0.83	0.96	0.98
Cohesive Stiffness (MPa/mm)	0.125	0.125	0.25

Cohesive Strength (***MPa***)	0.05	0.05	5.0
Separation to Failure (***mm***)	5.0	5.0	5.0

Curved Wedge

The second geometry is referred to as "Curved Wedge" and consist of a quadrilateral shape with a curved side. Figure 118 shows the CAD geometry of the curved wedge. The dimensions of the curved wedge printed in the CAMRI system are 450 mm, 200 mm, and 66 mm in length, width, and height, respectively. Similarly, the dimensions of the curved wedge printed in the LSAM system are 2200 mm, 950 mm, and 330 mm in length, width, and height, respectively.

This geometry was designed to promote deformation by two different mechanisms. First, the curved section was designed to introduce stresses in the radial and hoop direction which can lead to spring-in deformation. Stresses develop due to the difference in CTE in the radial and hoop direction, thus the larger the mismatch in CTE the higher the stresses developed. Second, the tapered regions were designed to promote warpage at the ends of the part. The warpage introduced at the ends results from the competing effect of thermal stresses developed as layers of molten material are deposited on top of previously deposited layers that are at a relatively lower temperature against the development of out-of-plane bending stiffness with the addition of new layers (bending stiffness scales with the cube of the height). Therefore, one of the ends is tapered to promote the warpage by reducing the bending stiffness in the region.

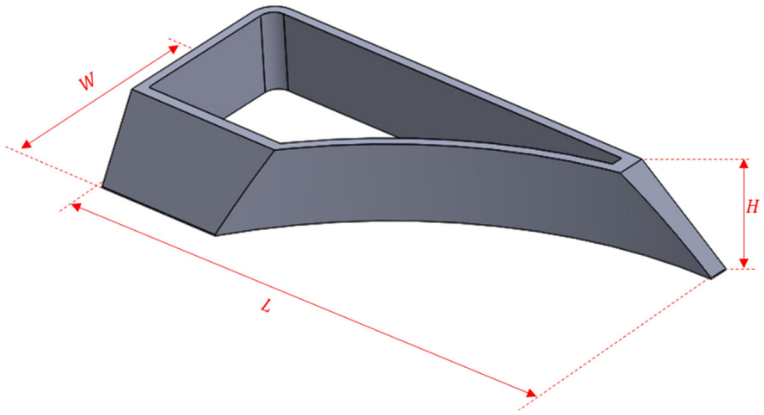

Figure 118: CAD geometry of the curved wedge.

The curved wedge was sliced with two beads across the width of the wall as illustrated in Figure 119. The beads were deposited from the inside to the outside and transitioned between layers at the front left corner as indicated in Figure 119.

Table 37 summarizes the process conditions used for printing the curved wedge. It should be noted

that the automatic layer time control was used in the LSAM with a target layer time of two minutes. As result, the print speed was automatically adjusted around the value shown in Table 37 by the LSAM controller. Furthermore, the part printed in the LSAM was removed from the bead board after cooling down to the ambient temperature (~after around 60 min).

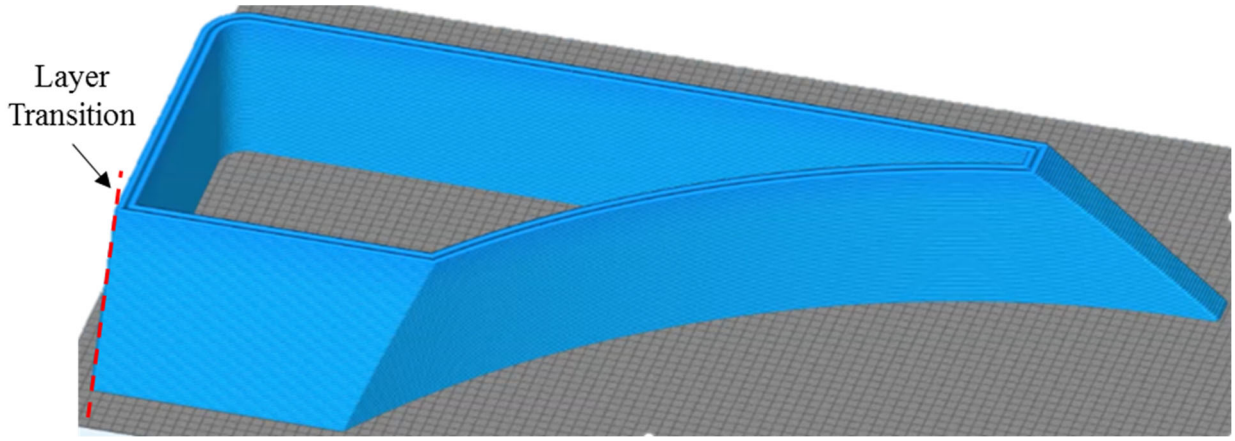

Figure 119. Slicing of the curved wedge geometry.

Table 37. Process conditions used for printing the curved wedge in the CAMRI.

Curved Wedge	50% wt. CF-PPS	25% wt. CF-PSU	25% wt. CF-PESU
Print Speed ($\boldsymbol{mm/min}$)	3000	3000	6450
Extrusion Temperature ($°\boldsymbol{C}$)	309	366	361
Melt Pump Temperature ($°\boldsymbol{C}$)	309	370	390
Nozzle Temperature ($°\boldsymbol{C}$)	315	370	395
sTime for cooling after printing part ($\boldsymbol{min}$)	10	10	60
AM System	CAMRI	CAMRI	LSAM

The curved wedge was printed on the same types of substrates used for the plate. The time-temperature history was recorded at the exterior surface of the longest straight wall in the curved wedge. Further, the cooling process of the part after the printing process was recorded for about 10 minutes after the print was completed. Figure 120 shows the experimental set-up of the thermal

camera. The thermal camera was located approximately 0.49 m from the vertical wall in the curved wedge and recorded at 10 frames per second. The video cameras recorded the overall printing to confirm the layer time and the start point of a new layer. A similar experimental setup was used in the LSAM to record the temperature history.

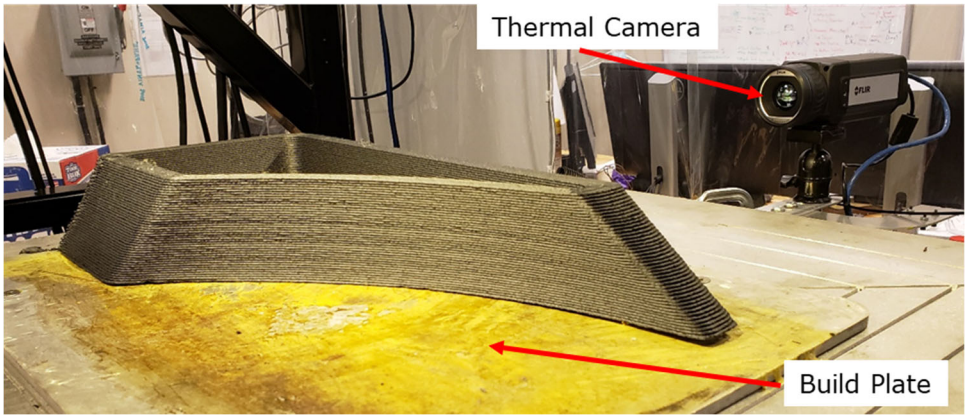

Figure 120. Experimental set-up used in the printing experiment of the curved wedge.

After cooling the curved wedge to room temperature, the top surface of the curved wedge geometry was laser scanned with the Faro® laser scanner. Only the top surface of the curved wedge was considered in the comparison between the shapes measured with the laser scanner and the shape predicted through the process simulations. Which is because the bottom surface is sensitive to the roughness of the adhesive layer and the beadboard, whereas the sides show a scalloped surface that result into significant noise in the point cloud collected with the laser scanner. Figure 121 shows an example of a point cloud captured with the laser scanner for the top surface of the curved wedge.

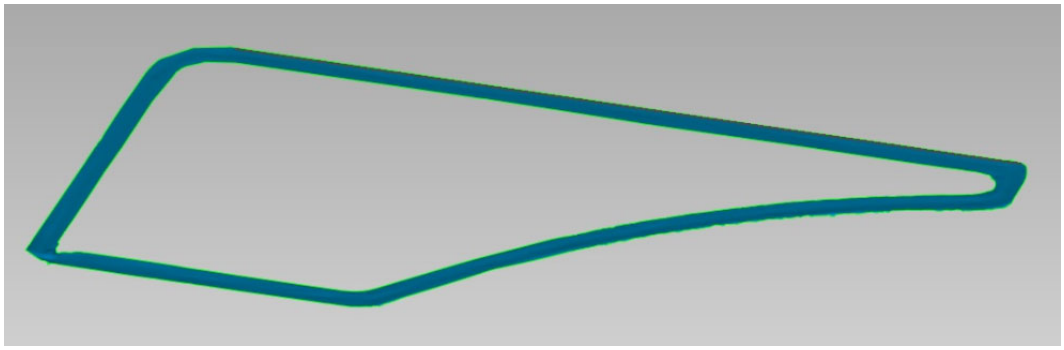

Figure 121. Example of point cloud scanned from the curved wedge printed in the CAMRI.

Inputs for Additive Process Simulation of Curved Wedge

A voxel FE mesh was generated based on the event series of the flat plate. Thus, elements are only

present where the print head deposits material. Beads were discretized with two elements in the width and one in the height which led to elements with dimensions of 3.075 mm in width and 1.5 mm in height for the curved wedge printed in CAMRI. Similarly, beads printed in the LSAM were discretized with two elements in the width and one in the height which led to elements with dimensions of 10.51 mm in width and 5.08 mm in height. Linear brick elements type DC3D8 and C3D8 were used in the heat transfer and mechanical analysis respectively [28].

A total of 58,652 and 145,057 finite elements were used to represent the geometry of the curve wedge printed in the CAMRI and LSAM, respectively. To capture the failure process of the thermosensitive adhesive bonding the curved wedge to the aluminum substrate in CAMRI, a cohesive contact was defined between the bottom surface of the printed part and the substrate. The substrate was included only in the mechanical analysis and was modeled as an analytical rigid surface. This approach considers debonding of the part from the substrate. Figure 122-A shows the FE mesh generated for the curved wedge and the analytical rigid surface for the substrate. To capture the interaction of the plate with the beadboard in the LSAM process, the bead board was modeled explicitly, and a cohesive contact was defined between the bottom surface of the printed part and the substrate. Figure 122-B shows the FE mesh generated for the plate and the bead board.

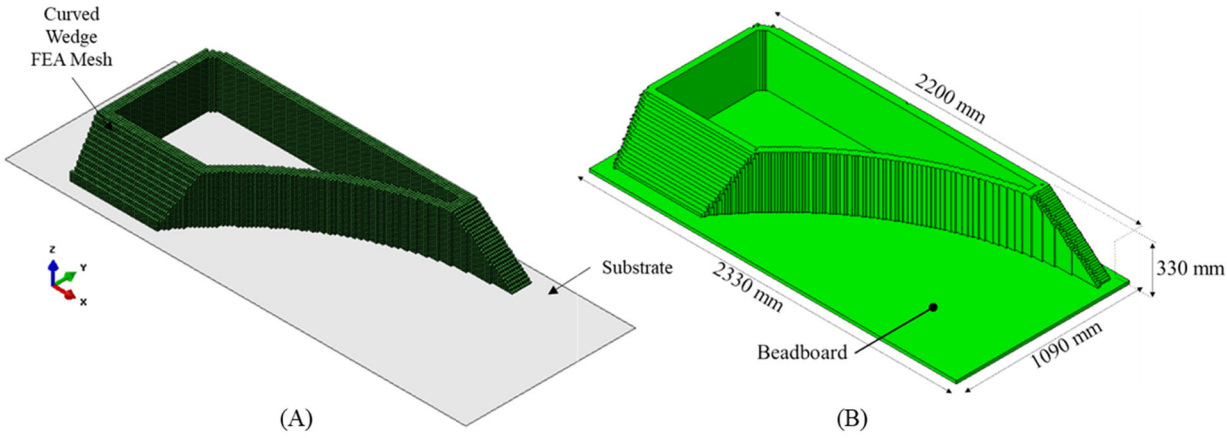

Figure 122: Voxel FEA mesh generated for the curved wedge. A) Curved wedge printed in the CAMRI system. B) Curved wedge printed in the LSAM and on top of beadboard.

The material properties reported in the section Material Characterization were used in the simulation of the EDAM process. To simulate the material in the molten state prior to deposition, the temperature of the nodes in the FEA mesh was initialized to the melt temperature. The bottom surface of the curved wedge is set to the temperature of the build plate for CAMRI, whereas an adiabatic boundary condition was considered at the bottom of the beadboard used in the LSAM.

The convection conditions developed at the surface of the plate were governed by a correlation equation that provides a local convection coefficient [3]. The heat removed with the tamper was measured experimentally [3]. Finally, the emissivity and the ambient temperature for radiation were calibrated based on the printing experiments. Similarly, the emissivity of the material can be determined using a black body cavity printed with the same material [3]. The constitutive behavior of the cohesive contact defined between the bottom surface of the printed part and the substrate was also informed based on previous investigations [29]. The substrate was assumed to fail dominantly under mode-I loading. Thus, a maximum stress failure initiation criterion and a displacement-based damage evolution law were used to describe the initiation and evolution of the debonding process, respectively [29]. Table 38 lists the parameters related to the process and to the material used in the simulation of the EDAM process of the curved wedge.

It should be noted that predictions for stress correspond to the local coordinate system (bead-orientation) whereas the predictions for deformation correspond to the global coordinate system (XYZ).

Table 38: Parameters of the process and material used in the simulation of the printing process of the curved wedge.

Parameter	50% wt. CF-PPS	25% wt. CF-PSU	25% wt. CF-PESU
Extrusion Temperature ($°\boldsymbol{C}$)	309	366	360
Deposition speed ($\boldsymbol{mm/min}$)	3000	3000	6450
Build Plate Temperature ($°\boldsymbol{C}$)	145	145	-
Ambient Temperature Convection ($°\boldsymbol{C}$)	35	50	35
Ambient Temperature Radiation ($°\boldsymbol{C}$)	72.5	102	35
Heat Removed with Compacter ($\boldsymbol{W}$)	8.0	8.0	80
Emissivity - $\boldsymbol{\varepsilon}$	0.95	0.96	0.98
Cohesive Stiffness ($\boldsymbol{MPa/mm}$)	0.125	0.125	0.25
Cohesive Strength ($\boldsymbol{MPa}$)	0.05	0.05	5.0

Displacement to Failure ($\boldsymbol{mm}$)	5.0	5.0	5.0

Validation of Simulation Predictions for CF-PPS

Experimental validation of the simulation predictions is of paramount importance to provide confidence on the simulation results and to verify that the most relevant phenomena developed in the printing process are captured correctly. Therefore, experimental validation of the temperature fields, time-temperature history, degree of crystallinity, and deformation was carried out for the two geometries investigated in this program. This also validates the digital material card generated for the CF-PPS.

Flat Plate

Figure 123 shows a qualitative comparison between the temperature fields captured with the thermal camera (top) and the temperature field predicted in the process simulations (bottom) after printing the second layer, the fourth layer, and after cooling for 2 minutes while attached on the CAMRI build plate. The temperature gradient in both the experimental and simulation fields is on the same scale. Overall, temperature fields characterized experimentally and predicted through the EDAM process simulations are in good agreement. The predicted temperature field is slightly colder than the one observed experimentally (noticeable after the cooling process).

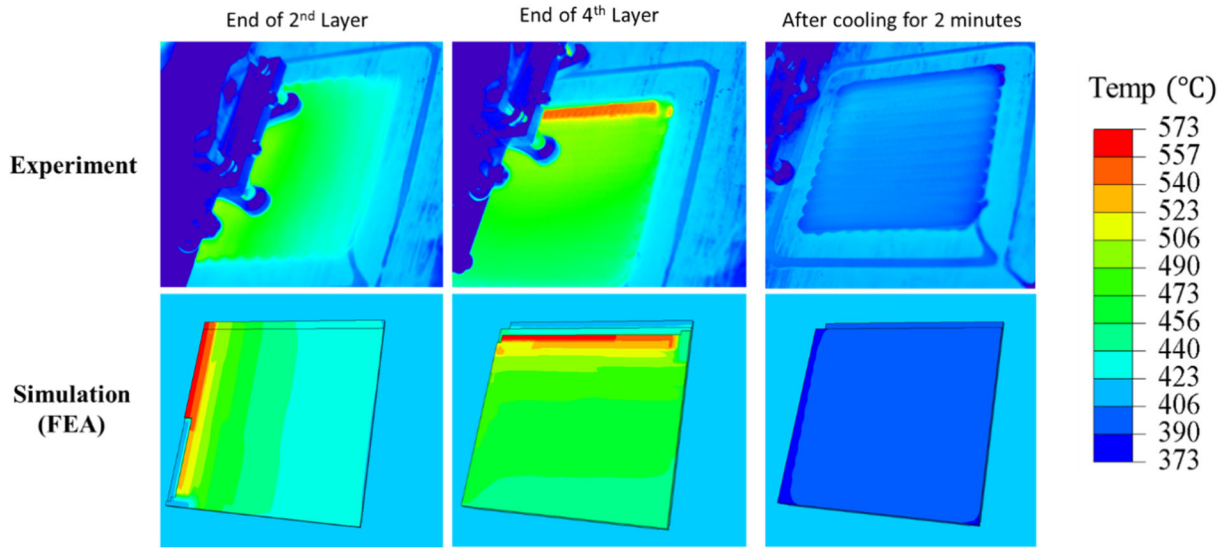

Figure 123. Comparison of temperature fields measured experimentally and predicted with process simulation at different instants of the printing process of the plate.

Figure 124 shows a quantitative comparison of the temperature profile developed along the width of the printed plate (red + marks) with the predictions of the process simulations (blue dashed line).

The temperature was extracted along the black dashed line at the end of the printing process of the third and the fourth layers. In general, temperature profile characterized experimentally and predicted through the EDAM process simulations are in good agreement and within $\pm 15\ ^{\circ}C$.

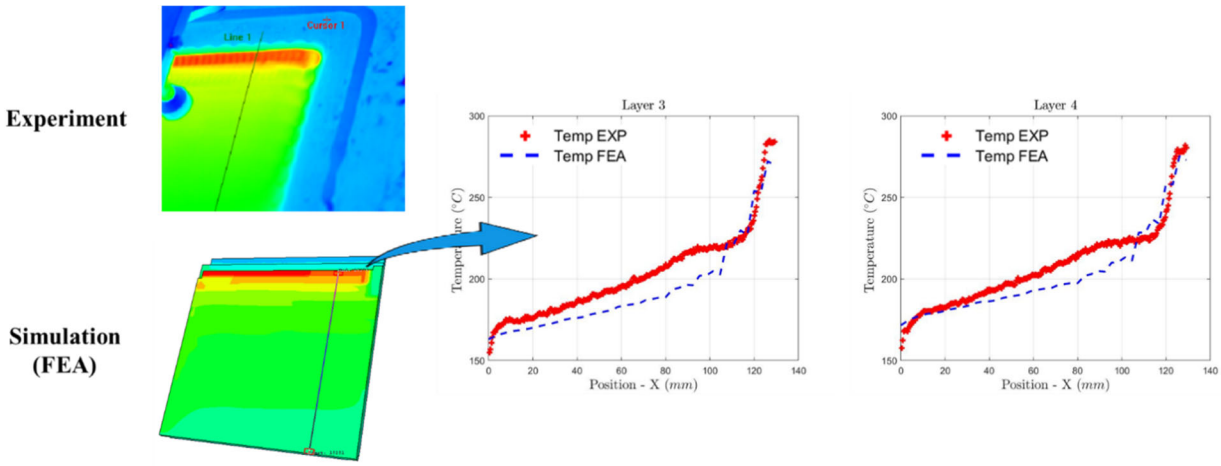

Figure 124. Comparison of temperature profile across the plate measured experimentally and predicted with process simulation after third and fourth-layer completion.

PPS is a semi-crystalline polymer and therefore, the degree of crystallinity was also predicted in the process simulations. Further, the degree of crystallinity is strongly coupled with the heat transfer analysis, with the material shrinkage, and with the stress relaxation behavior [1]. Figure 125 shows the degree of crystallinity predicted for the plate at the end of the printing process (A), after cooling for five minutes on the substrate (B), and after releasing from the substrate and cooling to the room temperature (C). The gradient in crystallinity shown at the end of the printing process of the plate along the X-direction (Figure 125 – A) is controlled by the temperature gradients shown in Figure 123. Further, the simulations results show that the maximum degree of crystallinity possible for this material system (0.66) was achieved at the end of the printing process of the plate.

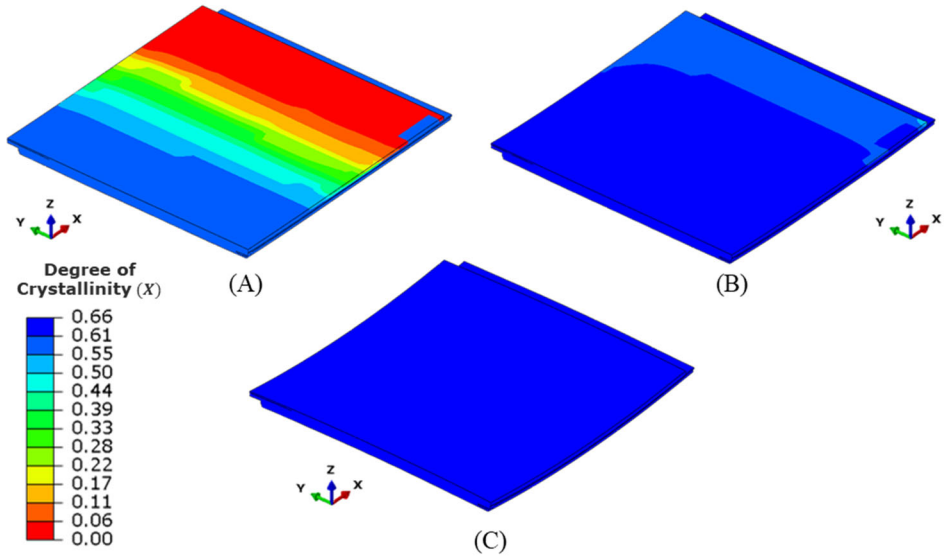

Figure 125. Degree of crystallinity predicted for plate printed with CF-PPS. A) At the end of the printing process. B) After cooling for five minutes on the build plate. C) After releasing from the build plate and cooled to the room temperature.

The crystallinity predicted with the process simulations was also verified against experimental measurements through DSC experiments. To verify the predictions for the degree of crystallinity shown in Figure 125, a small sample for DSC was extracted at the surface of the printed plate. A DSC experiment at a constant heating rate of $60\ °C/min$ verified that the crystallinity was fully developed as predicted by the process simulations (Figure 125– C). Figure 126 compares the heat flow measured from the sample extracted from the printed plate against the heat flow measured from a sample of polymer in the amorphous state or where crystallinity was not fully developed. The sample extracted from the printed plate only shows an endothermic transition around the glass transition temperature (Figure 126– A) and thus verifies that crystallinity was fully developed in the plate. In contrast, the sample of polymer in the amorphous state shows an exothermic reaction due to crystallization at temperatures above the glass transition temperature. Cold crystallization occurs upon heating above the glass transition temperature in semi-crystalline polymers when crystallization was precluded by rapid cooling of the polymer from the melt state [14].

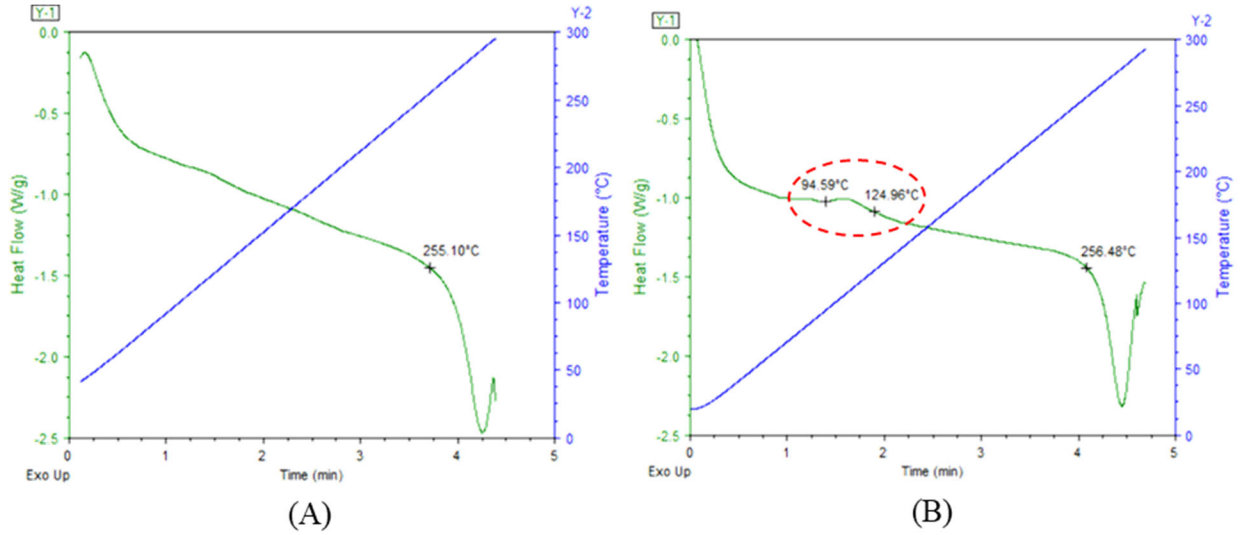

Figure 126. Verification of degree of crystallinity through DSC experiments. A) DSC experiment of sample extracted from printed plate that confirms the maximum crystallinity was developed. B) Reference DSC experiment where cold crystallization develops.

The evolution of residual stresses and deformation developed during the printing process of the plate geometry was also predicted in the process simulations. Figure 127 shows the stress transverse to the print direction (2 direction in the local material orientation) developed at the end of the printing process (A), after cooling of the printed plate for five minutes on the build plate (B), and once the plate was removed from the build plate and cooled to the room temperature (C). Removing the constraint at the bottom surface of the plate imposed by the adhesive allows deformation of the printed plate as the internal stresses re-equilibrate. Figure 127 B and C show a reduction in tensile stress at the center of the plate resulting from removing the plate from the substrate. It should be noted though, the stress state shown in Figure 127 C is when the plate has been released from the build plate and cooled to the room temperature.

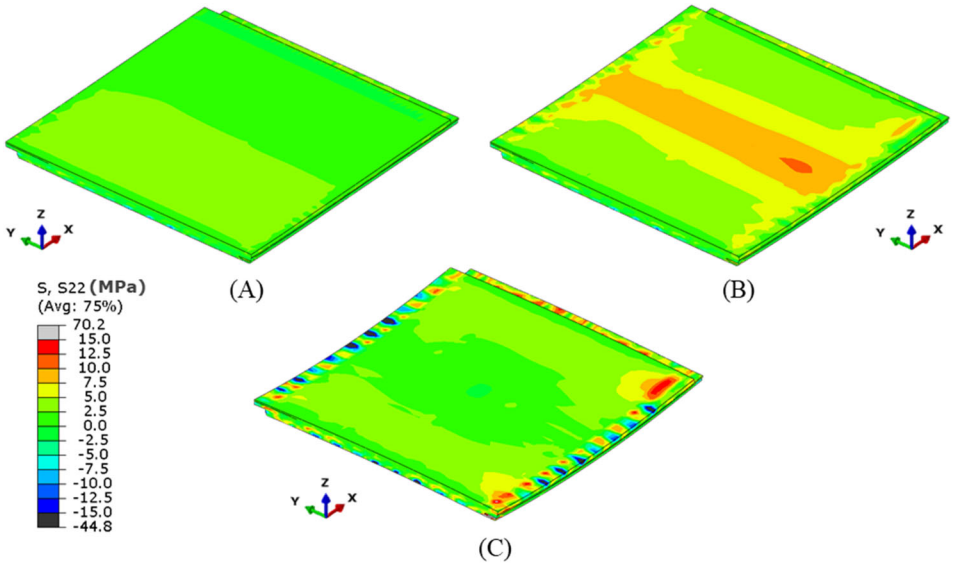

Figure 127. Stress transverse to the print direction (2-direction) predicted for plate printed with CF-PPS. A) At the end of the printing process. B) After cooling for five minutes on the build plate. C) After releasing from the build plate and cooled to the room temperature. It should be noted that predictions for stress correspond to the local coordinate system (bead-orientation) whereas the predictions for deformation correspond to the global coordinate system (XYZ).

Figure 128 shows the displacement in the layer stacking direction (3-direction) developed at the end of the printing process (A), after cooling of the printed plate for five minutes on the build plate (B), and after the plate was removed from the plate and cooled down to the room temperature. A hyperbolic paraboloid with radii of curvature of similar magnitude but opposite direction is generally expected for a plate with an antisymmetric layup. Nevertheless, the hyperbolic paraboloid developed by the printed plate shows a significantly different radius of curvature along the X-direction than the Y-direction. Such a difference in radii of curvature results from the thermal residual stresses developed during the printing process, and from the initiation of debonding of the part from the build plate at the edges of the part parallel to the Y-direction towards the end of the printing process of the part (Figure 128-A). The failure of the adhesive at the edges parallel to the Y-direction allows the part to curve up along the X-direction, thereby increasing the bending stiffness of the plate in the transverse direction (Y-direction). Once the plate is released from the substrate, the plate continues to deform as it cools to the room temperature. Hence, the final shape of the plate shown in Figure 128-C is strongly influenced not only by the material properties but also by the manufacturing history as explained before. The reader is referred to the work of Barocio et al. [29] for a more detailed discussion on the influence of the substrate characteristics on the final deformation of a printed part.

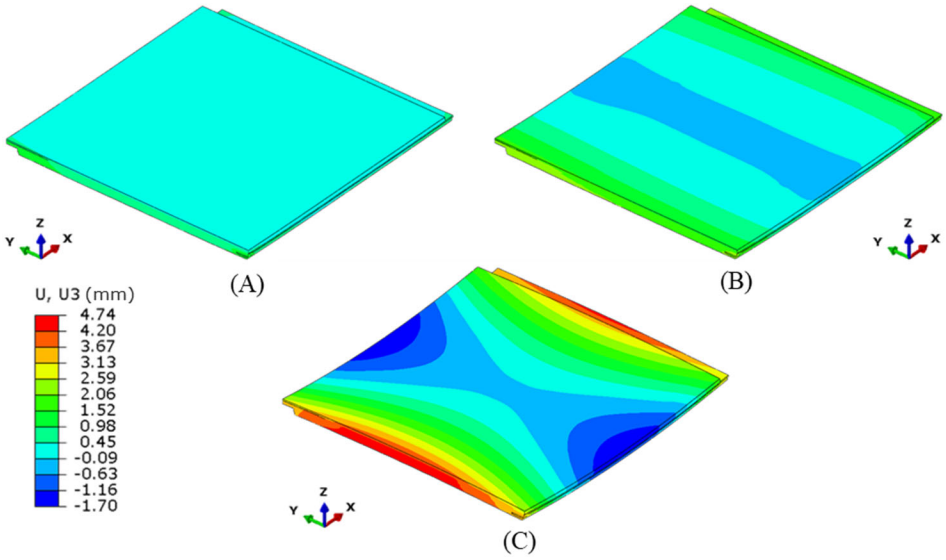

Figure 128. Displacement in the layer stacking direction (3-direction) predicted for plate printed with CF-PPS. A) At the end of the printing process. B) After cooling for five minutes on the build plate. C) After releasing from the build plate and cooled to the room temperature.

The next validation is for the shape predictions of the printed plate. A quantitative comparison was carried out for the shape predicted with the process simulations and the shape measured with the laser scanner. The deformed shape predicted through the process simulations was extracted at the top surface of the plate and imported into the software Geomagic Wrap©. The laser scan measurements (point cloud) of the top surface of the deformed printed part was also imported into the software Geomagic Wrap©. The deformed shape measured experimentally was set as the reference or baseline in Geomagic Wrap©, and an automatic best fit alignment of the predicted shape to the reference was carried out while enforcing the correct relative orientation of the deformed shapes. In other words, the relative orientation of the plate known based on the print history was enforced during the best fit alignment. After the best fit alignment of the two shapes, a deviation analysis with respect to the reference (experimental measurement) was carried out. Figure 129 shows the deviation of the shape predicted through the process simulation with respect to the experimental measurement. The deviation is computed as the normal distance between a point in the predicted shape to the reference shape. The deviations between the two shapes are well within ± 0.36 mm which represents less than 8% of the maximum deformation developed in the 3-direction (Figure 128). Finally, these results show a great correlation between the experimental measurements and the predictions of the process simulations.

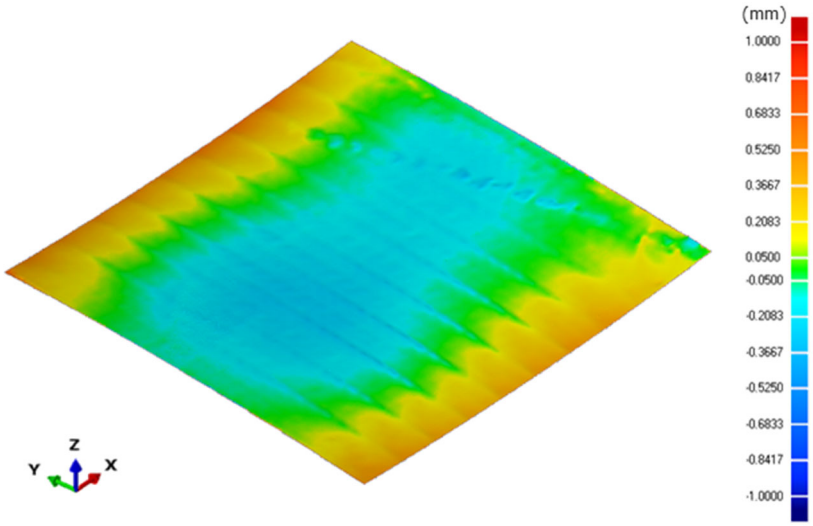

Figure 129. Deviation of the shape predicted through the process simulation with respect to the experimental measurement for CF-PPS.

Curved Wedge

Figure 130 shows a qualitative comparison between the temperature field captured with the thermal camera (left) and the temperature field predicted in the process simulations (right) after printing 10 layers, 20 layers, and 40 layers. Further, the scales in both temperature fields are in the same temperature range to provide a direct comparison of the experimental and predicted temperature fields. In general, a close correspondence between the temperature fields characterized experimentally and predicted through the EDAM process simulations was attained. However, the temperature fields predicted in the curved regions of the model were slightly cooler ($10 - 15\ °C$) than the experimental observations. Which is caused by overestimating the exposed area in the FE mesh resulting from the discretization of the curved wedge with a voxel mesh. In other words, the exposed area subjected to convective and radiative heat losses in the curved regions of the model is slightly larger than in the actual geometry.

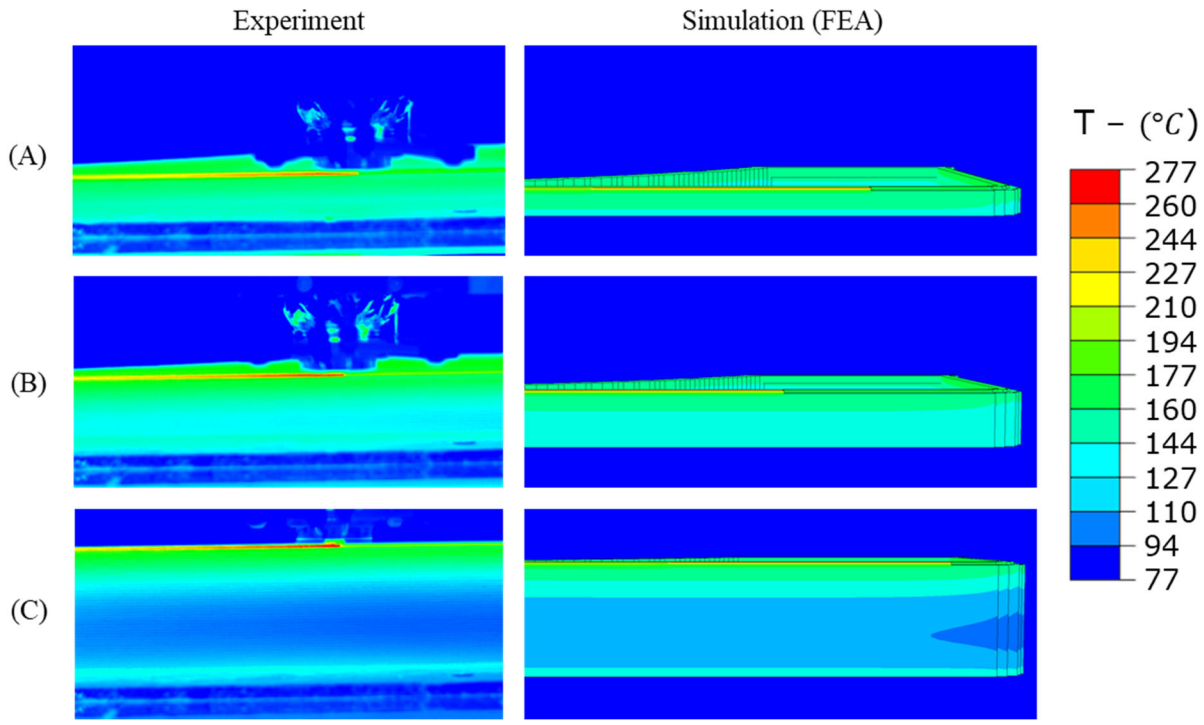

Figure 130. Verification of temperature fields characterized experimentally (left) and predicted in the EDAM process simulation (right). A) Temperature field at layer 10. B) Temperature field at layer 20. C) Temperature field at layer 40.

To provide a quantitative validation of the temperature predictions, a comparison of the transient temperature evolution measured experimentally and predicted through the process simulation was carried out for multiple layers. The time-temperature history was extracted at seven different layer locations starting at layer 10 and increasing in an interval of five layers until layer 40 and including the final 44th layer. Figure 131 shows approximately the layer locations for data extraction in both the experiments and the simulation predictions. The time-temperature history was extracted at the middle of the bead in the experimental measurements whereas the same information was extracted at a node located at the top of the printed bead in the process simulations. It should be noted that one element was used across the thickness of the bead for the FE model of the curved wedge. The time-temperature data was postprocess in Matlab© for visualization.

Figure 131. Layer locations in the curved wedge used to extract time-temperature history.

Figure 132 compares the experimental and predicted transient temperature evolution at eight different layers. The predictions of the transient temperature evolution are within $\pm 10\ ^{\circ}C$ of the experimental measurements. The great agreement between the simulation predictions and the experimental measurements demonstrate that the relevant heat transfer mechanisms are captured in the EDAM process simulation and the accuracy of the material card generated for the CF-PPS.

The process simulation correctly captures the rapid cooling developed at the surface of the printed beads upon deposition. Such a cooling behavior is caused primarily by the heat lost through radiation and through conduction with the material surrounding the bead as well as with the compacter. Subsequent spikes in the temperature history develop as beads of molten material are deposited on top of the bead observed. This observation applies for the first seven time-temperature histories shown in Figure 132 whereas the last layer cools down relatively faster than the previous layers due to the additional area exposed to convection and radiation at the top of the bead.

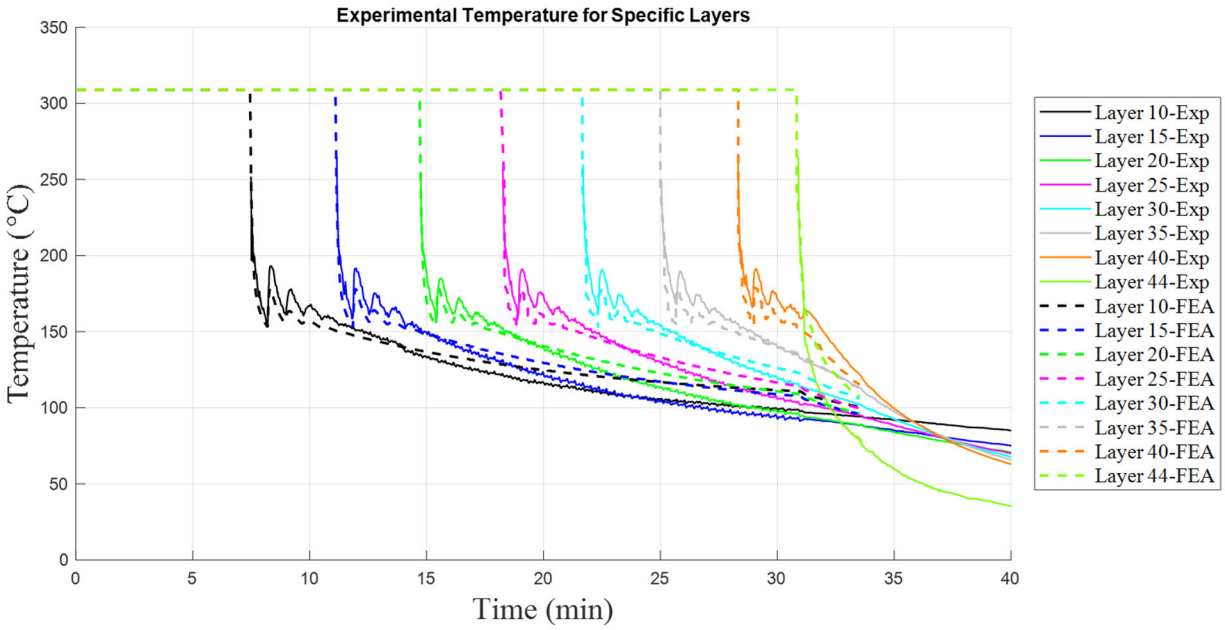

Figure 132. Comparison of time-temperature history measured experimentally and predicted with process simulation for different layers in the curved wedge.

The development of temperature gradients along the height of the curved wedge drives the crystallinity to develop from the bottom of the part and to progress in the vertical direction as the part was built layer by layer. Figure shows the evolution of the degree of crystallinity X predicted in the EDAM process simulation of the curved wedge at layer 10, at the end of deposition process, and after the part was at the room temperature. A degree of crystallinity of 0.66 was achieved in the entire part which corresponds to the maximum degree of crystallinity attained in this material

system. Achieving the maximum degree of crystallinity is important since it provides thermal stability to the printed material. Furthermore, the crystallinity also affects the thermoviscoelastic behavior of the printed material and the process of crystallization leads to shrinkage.

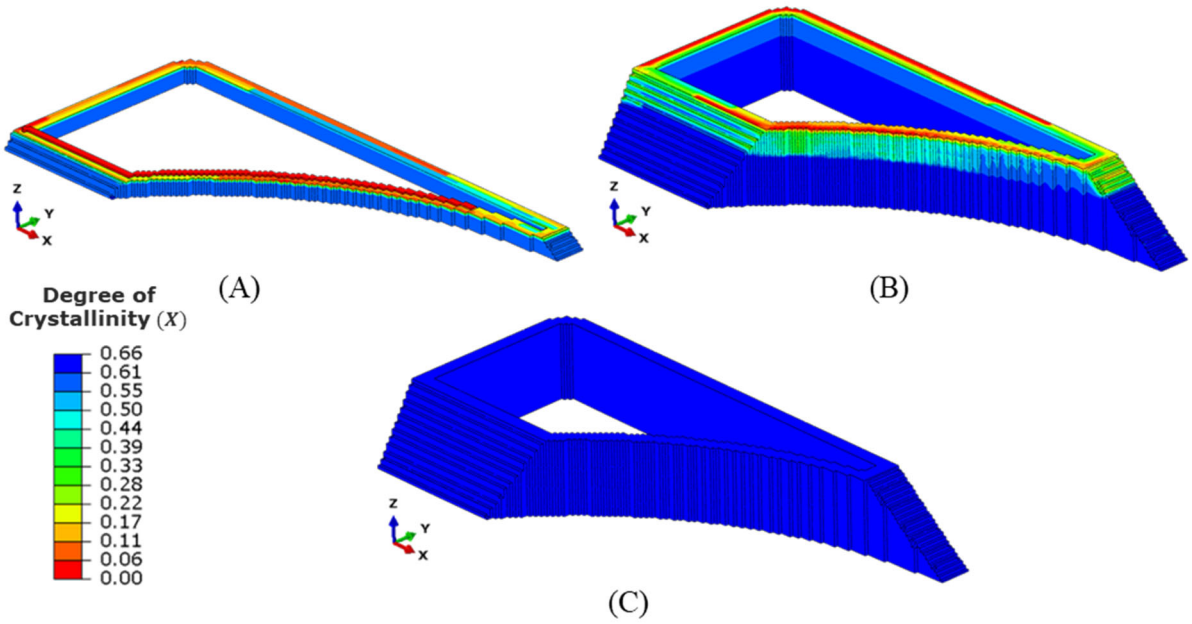

Figure 133. Degree of crystallinity predicted for curved wedge printed with CF-PPS. A) At layer 10. B) At the end of the printing process. C) After releasing from the build plate and cooled to the room temperature.

To verify the predictions for the degree of crystallinity shown in Figure 133, a small sample for DSC was extracted at the surface of the curved wedge. A DSC experiment at a constant heating rate of $60\ °C/min$ served to verify that crystallinity was fully developed in the curved wedge as predicted by the process simulations (Figure 133– C). Figure 134 compares the heat flow measured from the sample extracted from the curved wedge against the heat flow measured from a sample of polymer in the amorphous state or where crystallinity was not fully developed. The sample extracted from the curved wedge only shows an endothermic transition due to the glass transition temperature (Figure 134– A) and thus verifies that crystallinity was fully developed in the curved wedge. In contrast, the sample of polymer in the amorphous state shows an exothermic reaction due to crystallization at temperatures above the glass transition temperature (Figure 134– B). Cold crystallization occurs upon heating above the glass transition temperature in semi-crystalline polymers when crystallization was precluded by rapid cooling of the polymer from the melt state [14].

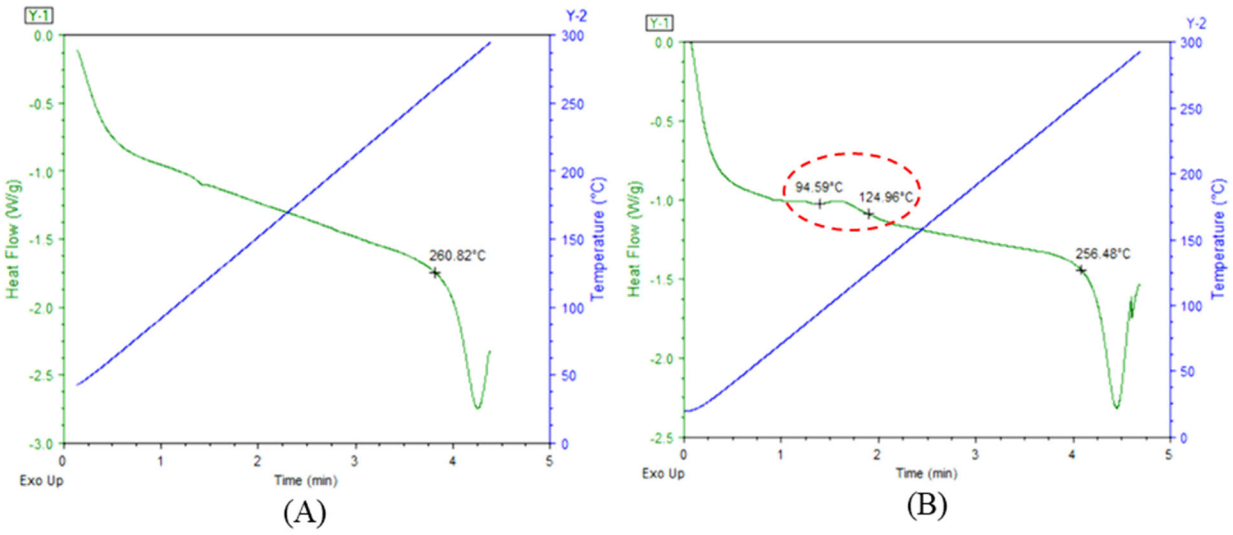

Figure 134. Verification of degree of crystallinity through DSC experiments. A) DSC experiment of sample extracted from curved wedge that confirms the maximum crystallinity was developed. B) Reference DSC experiment where cold crystallization develops.

The evolution of residual stresses and deformation developed during the printing process of the curved wedge was also predicted in the process simulations. Figure 135 shows the stress transverse to the print direction (2 direction in the local material orientation) developed after printing ten layers (A), after cooling of the curved wedge for five minutes on the build plate (B), and once the curved wedge was removed from the build plate and cooled to the room temperature (C). Removing the constraint at the bottom surface of the curved wedge imposed by the adhesive allows deformation of the curved wedge as the internal stresses re-equilibrate.

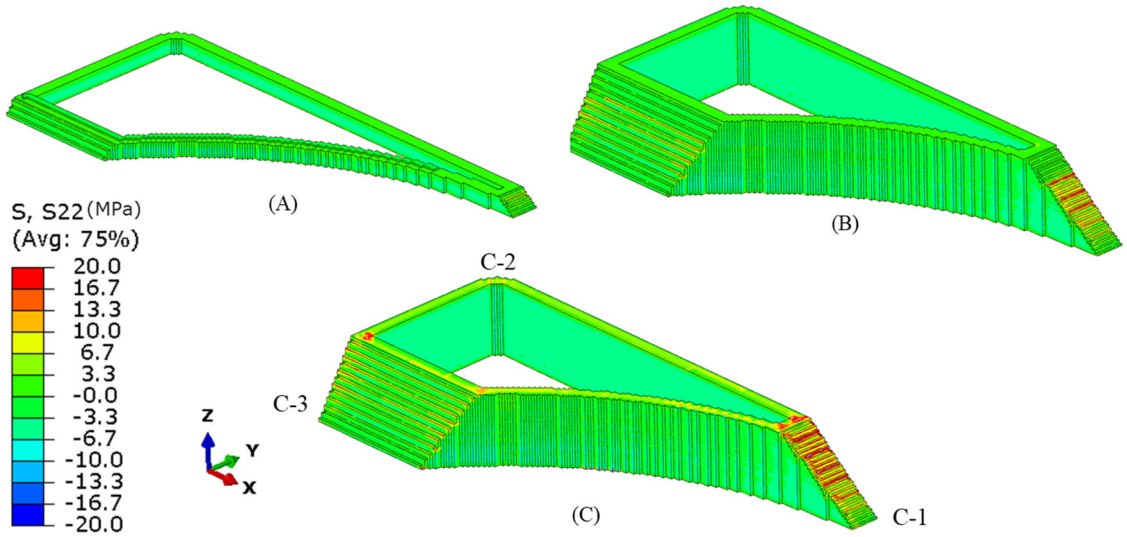

Figure 135. Stress transverse to the print direction (2-direction) predicted for curved wedge printed with CF-PPS. A) After printing ten layers. B) After cooling for five minutes on the build plate. C) After releasing from the build plate and cooled to the room temperature. It should be noted that predictions for stress correspond to the local coordinate system (bead-orientation).

The deformation of the curved wedge throughout the printing process and after cooling was also predicted in the process simulation. The curved wedge was initially bonded to the build plate with a layer of adhesive that constrains the deformation at the bottom of the printed geometry. However, the adhesive can fail due to the stresses resulting from constraining the material shrinkage and the thermal stresses developed during the printing process of the part, thereby allowing the part to freely deform in the regions where the adhesive fails. Figure 136 shows the evolution of the displacement in the layer stacking direction (3-direction) at different instants of the printing process of the curved wedge. All the corners of the curved wedge started to curve up at around layer 20. The “Corner 1” of the curved wedge (indicated as C-1 in Figure 136) curve up the most of all corners.

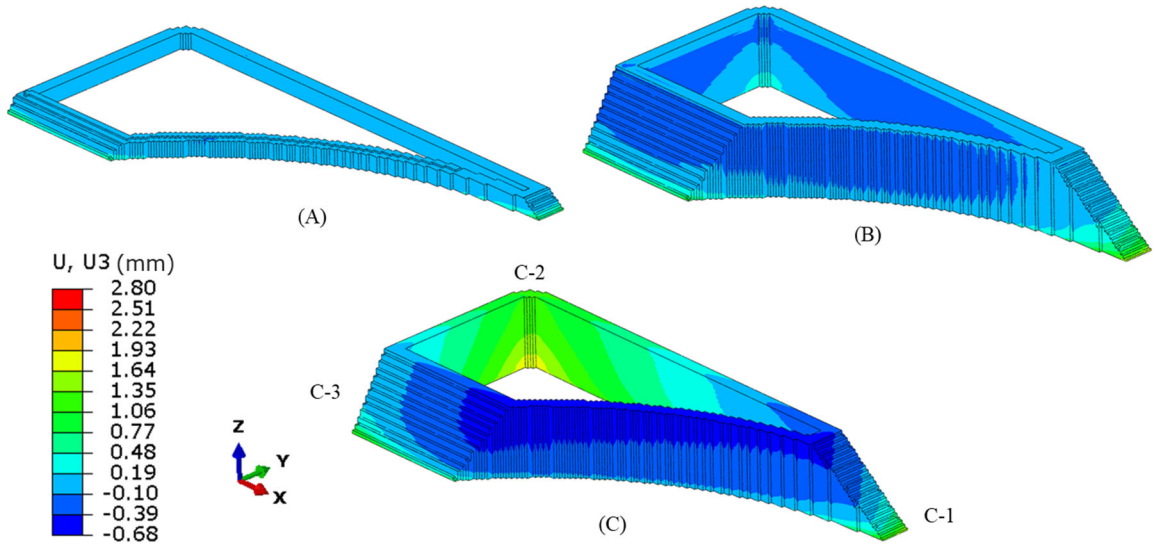

Figure 136. Displacement in the layer stacking direction (3-direction) predicted for the curved wedge printed with CF-PPS. A) After printing ten layers. B) After cooling for five minutes on the build plate. C) After releasing from the build plate and cooled to the room temperature.

To validate the predictions for deformation, a deviation analysis was carried out for the top surface of the curved wedge. The deformed shape predicted through the process simulations was extracted at the top surface of the curved wedge and imported into the software Geomagic Wrap©. The laser scan measurements (point cloud) of the top surface of the deformed curved wedge was also imported into the software Geomagic Wrap©. The deformed shape measured experimentally was set as the reference or baseline in Geomagic Wrap©, and an automatic best fit alignment of the predicted shape to the reference was carried out. After the best fit alignment of the two shapes, a deviation analysis with respect to the reference (experimental measurement) was carried out. Figure 137 shows the deviation of the shape predicted through the process simulation with respect to the experimental measurement. The deviation is computed as the normal distance between a point in the predicted shape to the reference shape. The deviations between the two shapes are well within ± 0.2 mm which represents around 7.2% of the maximum deformation developed in the 3-direction. It should be noted that the large deviation (~ 0.5 mm) observed at corner C3 is the result of the transition between layers that occurs at that location. Finally, these results show a great correlation between the experimental measurements and the predictions of the process simulations.

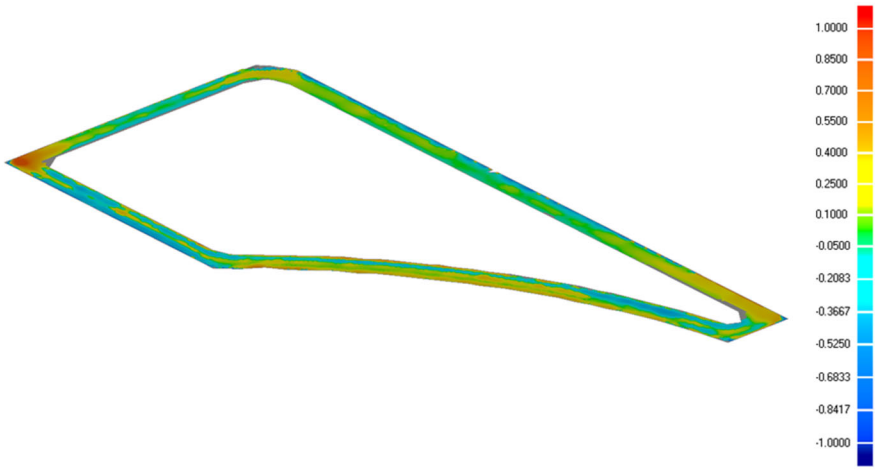

Figure 137. Deviation between the shape measured experimentally and predicted through the process simulation for the top surface of the curved wedge printed with CF-PPS.

Validation of Simulation Predictions for CF-PSU

Experimental validation of the simulation predictions is of paramount importance to provide confidence on the simulation results and to verify that the most relevant phenomena developed in the printing process are captured correctly. Therefore, experimental validation of the temperature fields, time-time history, and deformation was carried out for the two geometries investigated in this program. This also validates the digital material card generated for the material 25% CF-PSU.

Flat Plate

Figure 138 below shows a qualitative comparison between the temperature fields captured with the thermal camera (top) and the temperature field predicted in the process simulations (bottom) after printing the second, the fourth, and after cooling for 5 minutes while attached on the CAMRI build plate. The temperature gradient in both temperature fields is on the same scale. Overall, temperature fields characterized experimentally and predicted through the EDAM process simulations are in good agreement.

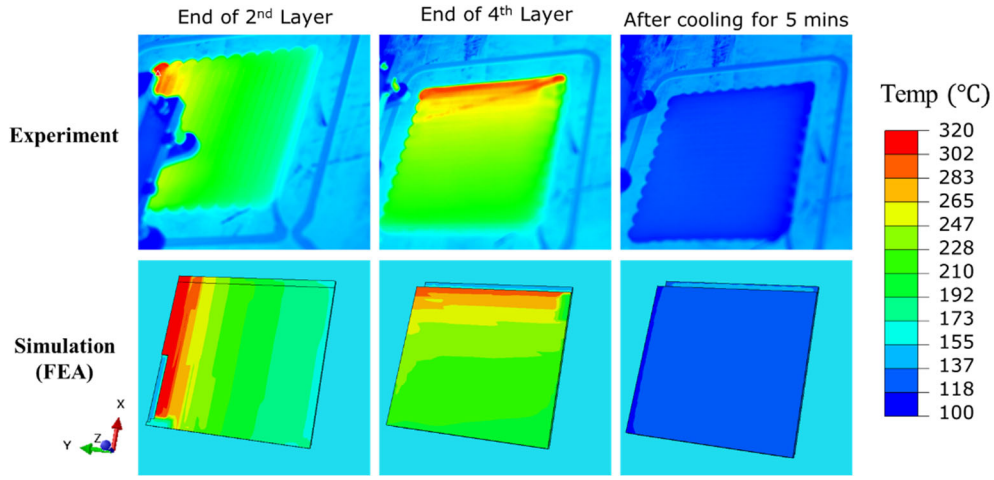

Figure 138. Comparison of temperature fields measured experimentally and predicted with process simulation at different instants of the printing process of the plate.

Figure 139 shows a quantitative comparison between the temperature along the width of the printed plate represented in red, with the process simulation predictions shown in blue. The temperature was extracted at the black dashed line at the end of third- and fourth-layer deposition. Overall, temperature fields characterized experimentally and predicted through the EDAM process simulations are in good agreement. The predicted temperature field is slightly higher at first, then at approximately 20 mm, the predicted temperature becomes slightly colder than the one observed experimentally, and the maximum difference is around 20°C.

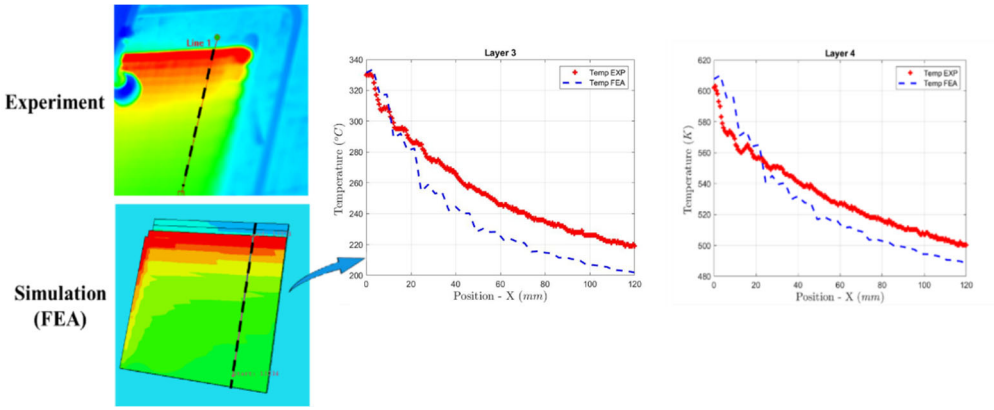

Figure 139. Comparison of temperature variation across the plate measured experimentally and predicted with process simulation after third- and fourth-layer completion.

The evolution of residual stresses and deformation developed during the printing process of the plate geometry was also predicted in the process simulations. Figure 140 shows the stress transverse to the print direction (2 direction in the local material orientation) developed at the end

of the printing process (A), after cooling of the printed plate for five minutes on the build plate (B), and once the plate was removed from the build plate and cooled to the room temperature (C). Removing the constraint at the bottom surface of the plate imposed by the adhesive allows deformation of the printed plate as the internal stresses re-equilibrate. Figure 140 C shows a reduction in tensile stress at the center of the plate resulting from removing the plate from the substrate.

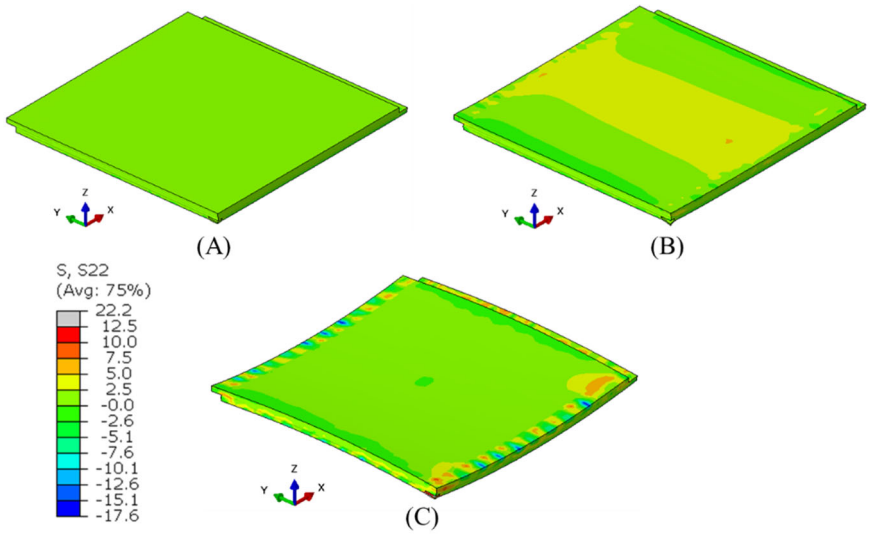

Figure 140. Stress transverse to the print direction (2-direction) predicted for plate printed with CF-PSU. A) At the end of the printing process. B) After cooling for five minutes on the build plate. C) After releasing from the build plate and cooled to the room temperature. It should be noted that predictions for stress correspond to the local coordinate system (bead-orientation).

Figure 141 shows the displacement in the layer stacking direction (3-direction) developed at the end of the printing process (A), after cooling of the printed plate for five minutes on the build plate (B), and after the plate was removed from the plate and cooled down to the room temperature. A hyperbolic paraboloid with radii of curvature of similar magnitude but opposite direction is generally expected for a plate with an antisymmetric layup. Nevertheless, the hyperbolic paraboloid developed by the printed plate shows a significantly different radius of curvature along the X-direction than the Y-direction. Such a difference in radii of curvature results from the thermal residual stresses developed during the printing process, and from the initiation of debonding of the part from the build plate at the edges of the part parallel to the Y-direction and towards the end of the printing process of the part (Figure 141-A). The failure of the adhesive at the edges parallel to the Y-direction allows the part to curve up along the X-direction, thereby increasing the bending stiffness of the plate in the transverse direction (Y-direction). Once the plate is released from the substrate, the plate continues to deform as it cools to the room temperature. Hence, the final shape

of the plate shown in Figure 141-C is strongly influenced not only by the material properties but also by the manufacturing history as explained before. As indicated, the maximum and minimum deformation in stacking direction is 2.1 mm and -1.5 mm respectively. The reader is referred to the work of Barocio et al. [29] for a more detailed discussion on the influence of the substrate characteristics on the final deformation of a printed part.

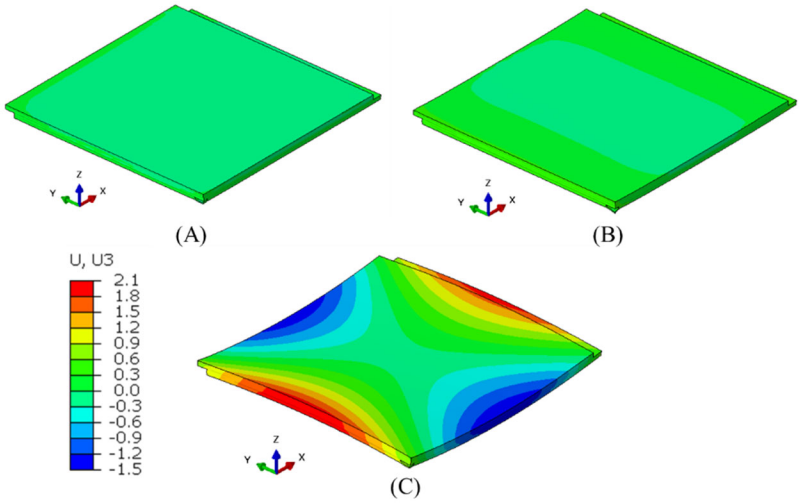

Figure 141. Displacement in the layer stacking direction (3-direction) predicted for plate printed with CF-PSU. A) At the end of the printing process. B) After cooling for five minutes on the build plate. C) After releasing from the build plate and cooled to the room temperature.

A comparison of the deformation measured in the stacking direction was carried out for the plate. For process simulation deformation, a set of spatial positions of all the nodes of the top surface of the plate was extracted and imported into Geomagic Wrap© software. The surface of the plate was recreated in the Geomagic Wrap© by connecting the x, y, and z position of all the nodes. The CAMRI printed plate deformation was obtained by laser scanning only the top surface. The laser scan data was also imported and post process in Geomagic Wrap©.

Figure 142 compares the deformation in the stacking direction measured experimentally against the deformation predicted with the simulations. The experimental deformation was set as the baseline. As indicated in the Figure 142, most of the deviation is within 1 mm of the experimentally measured deviation. The deviations between the two shapes are well within ± 0.25 mm which represents around 11% of the maximum deformation developed in the 3-direction (Figure 141).

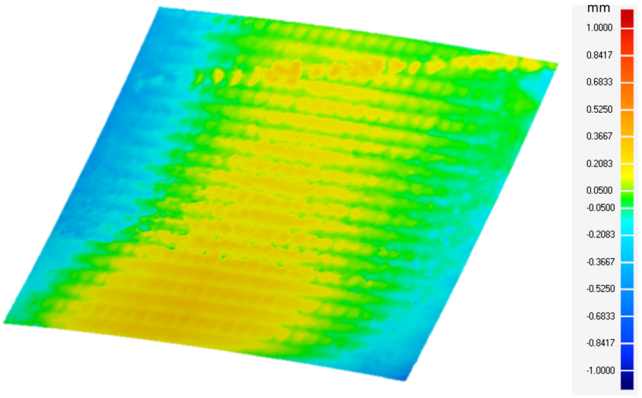

Figure 142. Deviation of the shape predicted through the process simulation with respect to the experimental measurement for CF-PSU.

Curved Wedge

Figure 143 shows a qualitative comparison between the temperature field captured with the thermal camera (left) and the temperature field predicted in the process simulations (right) after printing 10 layers, 20 layers, and 40 layers. Further, the scales in both temperature fields are in the same temperature range to be able to compare side-to-side the experimental and predicted temperature fields. Overall, a close correspondence between the temperature fields characterized experimentally and predicted through the EDAM process simulations is observed.

As the simulation was constructed with voxel FE mesh, the exposed surface in the curvature area is not as smooth as the experimental printed part which leads to an overexposure surface in the curved regions. The overexposed surface results in slightly higher heat losses, thus causing the curved regions to cool down slightly faster than in the experiment.

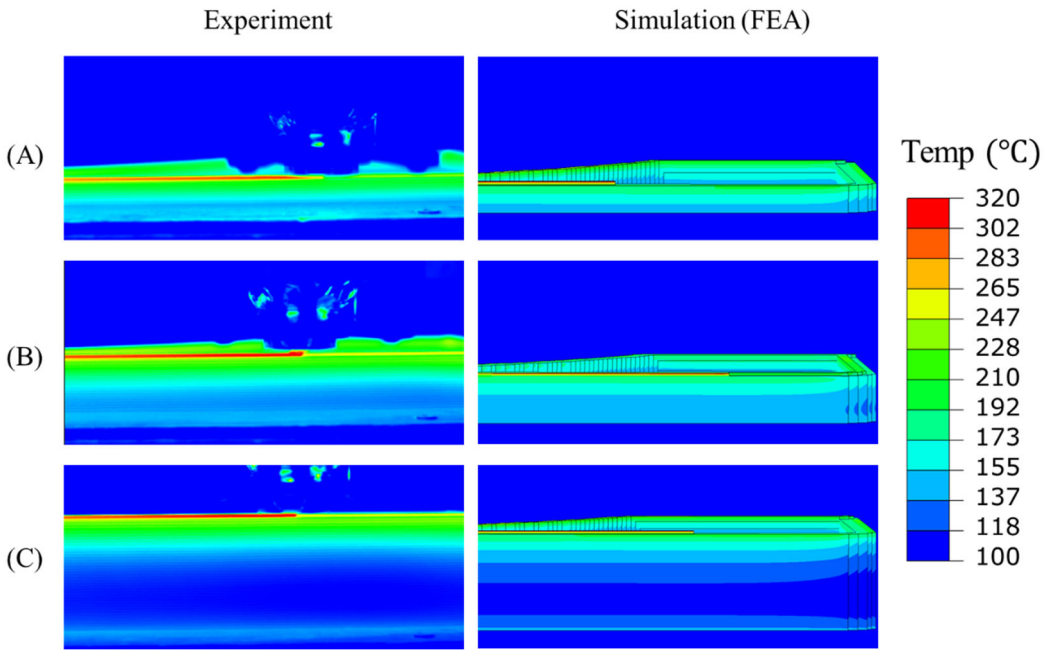

Figure 143. Validation of temperature fields characterized experimentally (left) and predicted (right) in the EDAM process simulation. A) Temperature field at layer 10. B) Temperature field at layer 20. C) Temperature field at layer 40.

The transient temperature evolution during the printing process of the curved wedge was extracted at different layer locations from both the printing experiment and FEA. The goal is to provide a quantitative comparison of the temperature predictions and the experimental measurements. Seven-layer locations were chosen starting at layer 10 and increasing in an interval of five until layer 40, and in addition, the last layer number 44. Figure 144 shows approximately the layer locations from which transient temperature evolution was extracted for both experiment and simulation temperature history. The transient experimental temperature evolution was extracted at the middle of a printed bead right after the material deposited. The simulation temperature of a layer was extracted at the top node of the elements. The temperature history of every 5 layers and the last layer was extracted and imported into Matlab© to plot for visualization.

Figure 144. Layer locations in the curved wedge used for extracting time-temperature history.

Figure 145 compares the experimental and predicted transient temperature evolution at the eight-layer locations. The predictions of the transient temperature evolution are in good agreement with the experimental measurements, thereby demonstrating that the relevant heat transfer mechanisms are captured in the EDAM process simulation. As shown below, most of the predictions are within 20℃ of the experimentally measured temperature profiles. The plot of the transient temperature evolution shows the relatively rapid cooling the material undergoes at the surface which is primarily due to heat losses through radiation and due to heat removed by the tamper. A local increase in temperature can be also noticed in the first seven transient temperature curves as a new layer of material is deposited on top of the layer observed. A more detailed analysis of the heat transfer mechanisms can be found in the study from Barocio [3].

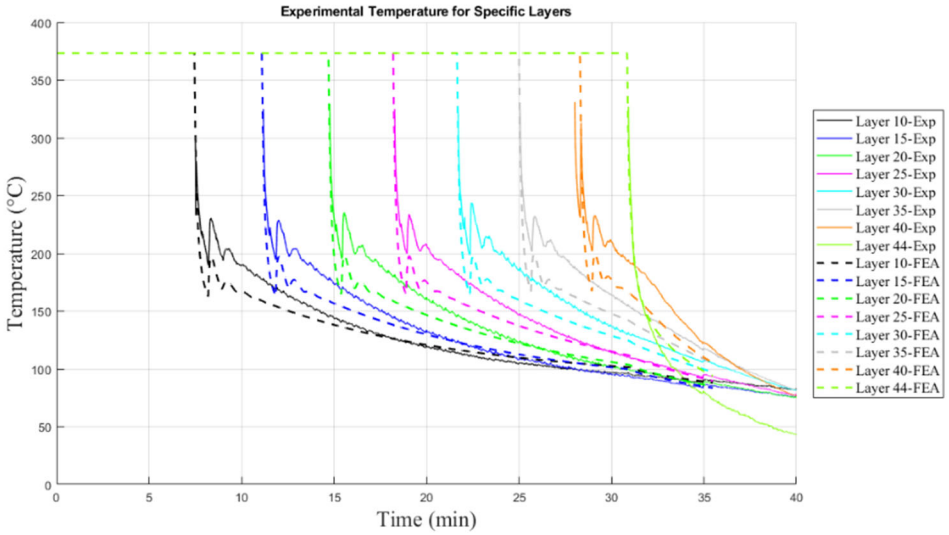

Figure 145. Comparison of time-temperature history measured experimentally and predicted with process simulation for different layers in the curved wedge.

The evolution of residual stresses and deformation developed during the printing process of the curved wedge was also predicted in the process simulations. Figure 146 shows the stress transverse to the print direction (2 direction in the local material orientation) developed after printing ten layers (A), after cooling of the curved wedge for five minutes on the build plate (B), and once the curved wedge was removed from the build plate and cooled to the room temperature (C). Removing the constraint at the bottom surface of the curved wedge imposed by the adhesive allows deformation of the curved wedge as the internal stresses re-equilibrate.

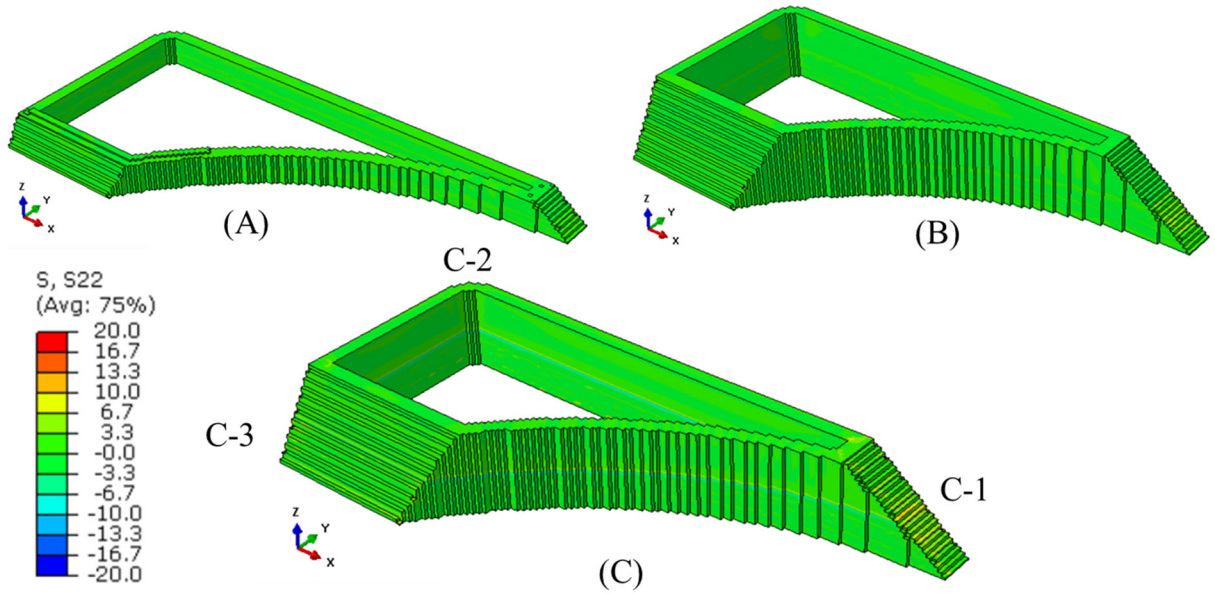

Figure 146: Stress transverse to the print direction (2-direction) predicted for curved wedge printed with CF-PPS. A) After printing ten layers. B) After cooling for five minutes on the build plate. C) After releasing from the build plate and cooled to the room temperature. It should be noted that predictions for stress correspond to the local coordinate system (bead-orientation).

The deformation of the curved wedge throughout the printing process and after cooling was also predicted in the process simulation. The curved wedge was initially bonded to the build plate but it gradually debonded from the build plate as stresses develop in the part, thereby allowing the part to deform in the vertical direction. Figure 147 shows the evolution of the displacement in the layer stacking direction (3-direction) at different instants of the printing process of the curved wedge. The “Corner 1” of the curved wedge (indicated as C) debonded from the substrate and started to curve up at around layer 40. The maximum and minimum deformation in the stacking direction is around 2.47 mm and -1.08 mm, after the part has been removed from the build plate and cooled to room temperature.

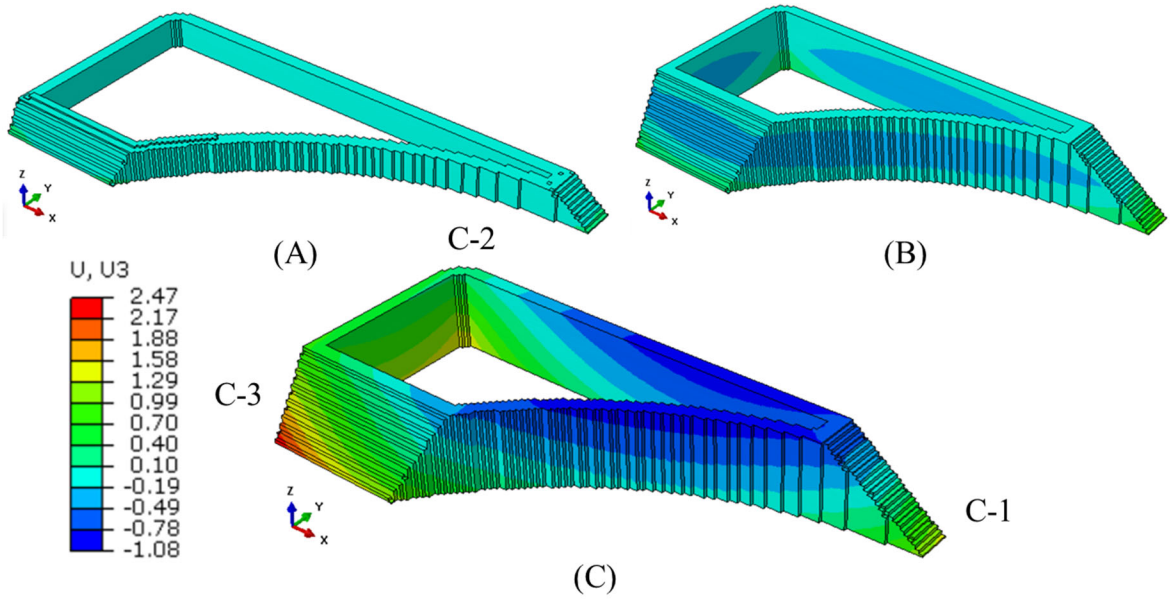

Figure 147. Displacement in the Z-direction predicted for the curved wedge printed with CF-PSU. A) After printing ten layers. B) After cooling for five minutes on the build plate. C) After releasing from the build plate and cooled to the room temperature.

A quantitative comparison of the deformation measured in the stacking direction was carried out for the curved wedge with similar process as the plate. A set of spatial positions of all the nodes of the curved wedge top surface was extracted from FEA and imported into Geomagic Wrap© software. The surface of the plate was recreated in the Geomagic Wrap© and compare with the laser scanned data of the CAMRI printed curved wedge. Figure 148 compares the deformation in the stacking direction measured experimentally against the deformation predicted with the simulations. The experimental deformation was set as the baseline and the color gradient shows the differences between the two surfaces. The deformation predicted overall are in good agreement with the experimental deformation as shown in green color. The corner that has blue color gradient is the start location of the new layer.

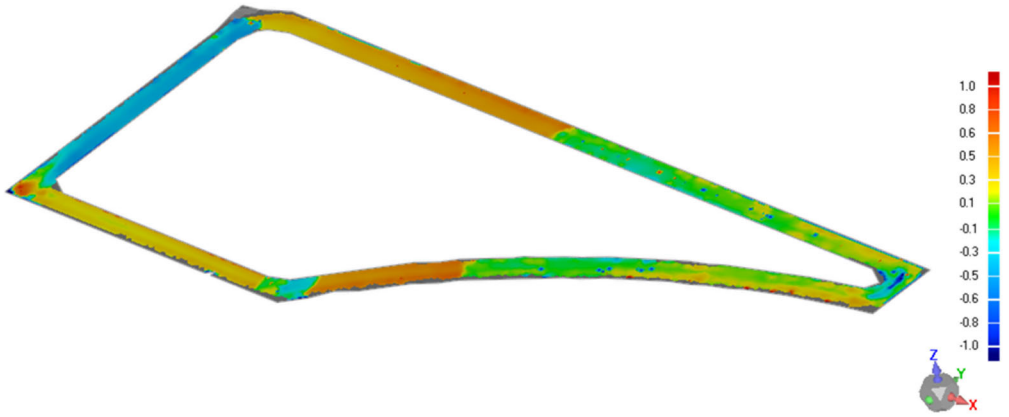

Figure 148. Deviation between the shape measured experimentally and predicted through the process simulation for the top surface of the curved wedge printed with CF-PSU.

Validation of Simulation Predictions for CF-PESU

Experimental validation of the simulation predictions is of paramount importance to provide confidence on the simulation results and to verify that the most relevant phenomena developed in the printing process are captured correctly. Therefore, experimental validation of the temperature fields, time-time history, and deformation was carried out for the two geometries investigated in this program. This also validates the digital material card generated for the material 25% CF-PESU printed in the Thermwood LSAM.

Flat Plate

The substrate used in this study in the LSAM system is the beadboard which is a ¾ inch plywood. On the surface of the plywood is a one layer of ABS pellets which are glued to the plywood as shown in Figure 149. The beadboard is attached to the LSAM print bed by a set of screws around the area of the print. The screws were place approximately 127 mm apart.

Figure 149. Surface of the Beadboard..

Figure 150 shows the mesh and dimension of the $[0_2 90_2]$ plate and the beadboard. The beadboard was modeled as an isotropic elastic material with the elastic modulus of 70 GPa and Poisson's ratio of 0.32 [30]. The model included 25 screws which were modeled by a kinematic boundary condition (constraining all the degree of freedom) at the nodal locations corresponding to the screw positions. The section Inputs for Additive Process Simulation of Flat Plate described the cohesive contact that governs the interaction between the printed part and the beadboard.

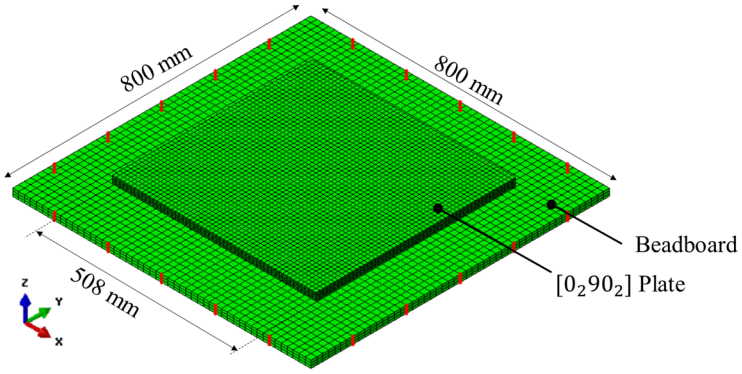

Figure 150. Dimensions and mesh of the plate printed in the LSAM on top of beadboard.

Figure 151 shows a qualitative comparison between the temperature fields captured with the thermal camera (top) and the temperature field predicted in the process simulations (bottom) after printing the second layer, the fourth layer, and after cooling for 5 minutes while attached on the LSAM beadboard. The temperature gradient in both the experimental and simulation fields is on

the same scale. In general, temperature fields characterized experimentally and predicted through the EDAM process simulations are in good agreement.

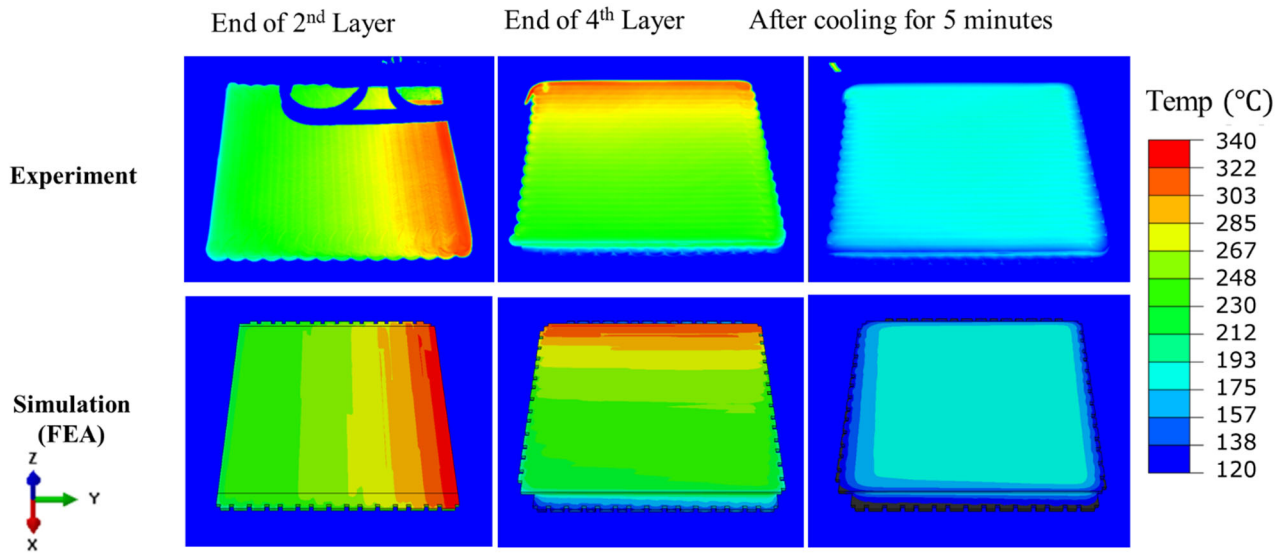

Figure 151. Comparison of temperature fields measured experimentally and predicted with process simulation at different instants of the printing process of the plate.

Figure 152 shows a quantitative comparison of the temperature profile developed along the width of the printed plate (red + marks) with the predictions in the process simulations (blue dashed line). The temperature was extracted along the red line (left) at the end of printing process of the third and fourth layers. In general, temperature profiles characterized experimentally and predicted through the EDAM process simulations are in good agreement and within ±20 °C. A slightly higher variation between the predictions and the measurements is observed in the warmest region of the plate.

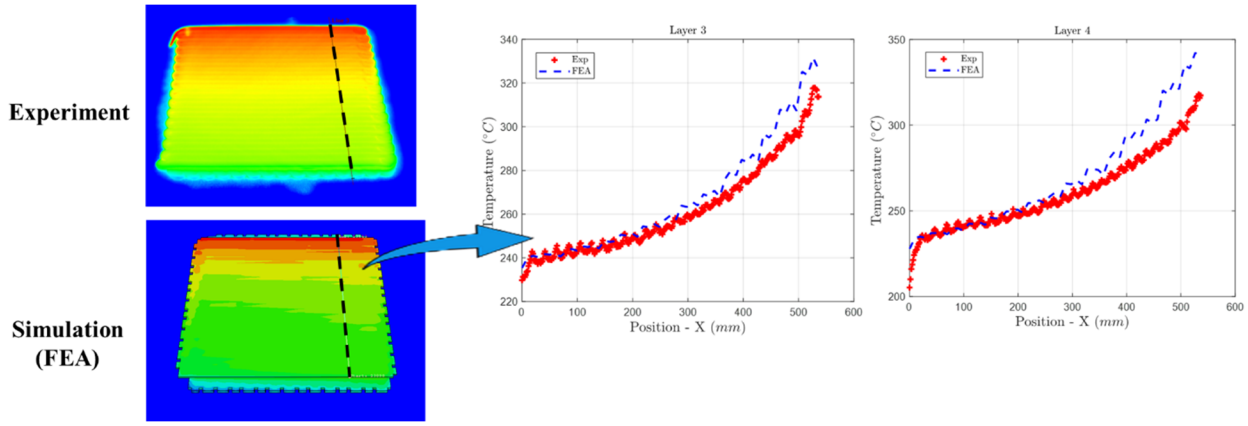

Figure 152. Comparison of temperature profile across the plate measured experimentally and predicted with process simulation after third- and fourth-layer completion.

Figure 153 shows the displacement in the layer stacking direction (3-direction) developed at the end of the printing process (A), after cooling of the printed plate for five minutes on the build plate (B), and after the plate was removed from the plate and cooled down to the room temperature (C). Similar to the earlier plates, a hyperbolic paraboloid develops due to the same mechanisms mentioned previously.

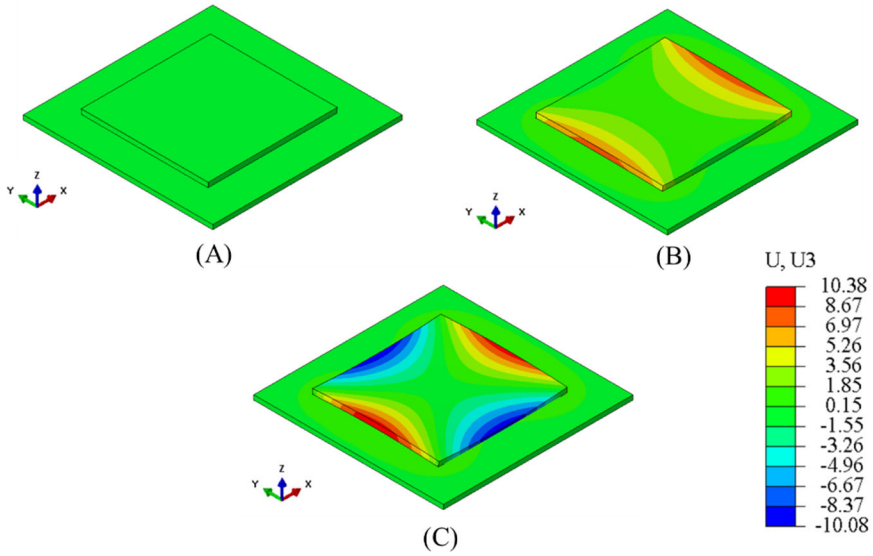

Figure 153. Displacement in the layer stacking direction (3-direction) predicted for plate printed with CF-PESU. A) At the end of the printing process. B) After cooling for five minutes on the beadboard. C) After releasing from the beadboard and cooled to the room temperature.

The experimental deformation was measured using a 3D laser scan. The deformation was taken from FEA and experiment after the plate has cooled to room temperature and taken out from the

beadboard. A comparison of the deformation of CF-PESU was carried out following the same procedure as the CF-PPS and CF-PSU plate. The deformation at the top surface of the plate predicted through the process simulations was laid on top of the experimentally measured deformed shape using the software Geomagic Wrap©. Figure 154 shows the deviation analysis of the shape predicted through the process simulation with respect to the experimental measurement. The deviation is computed as the normal distance between a point in the predicted shape to the reference shape. The deviations between the two shapes are within ±1.5 mm which represents around 14% of the maximum deformation developed in the 3-direction.

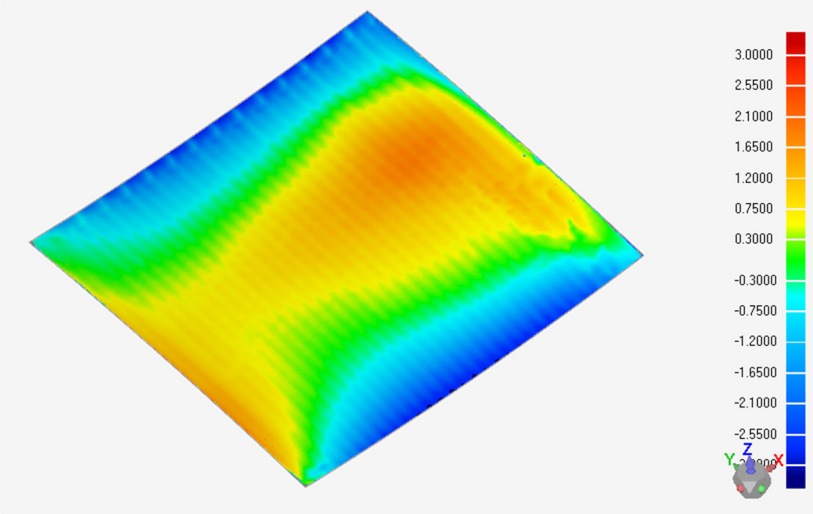

Figure 154. Comparison of deformation measured experimentally and predicted in process simulation.

Curved wedge

Similar to the plate, the curved wedge was printed in a piece of beadboard that was screwed to the table of the LSAM. Figure 155 shows the location of the screws used for fastening the beadboard to the table in the LSAM. Screws were modeled by a kinematic boundary condition (constraining all the degree of freedom) at the nodal locations corresponding to the screw positions. The beadboard was meshed with 100 elements in y-direction, 50 elements in x-direction, and 3 elements in z-direction. The section Inputs for Additive Process Simulation of Curved Wedge described the cohesive contact that governs the interaction between the printed part and the beadboard.

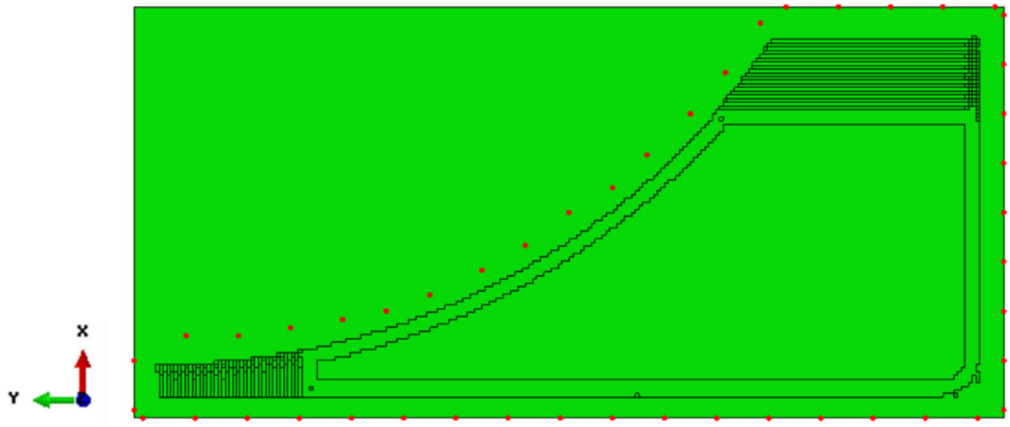

Figure 155. Location of screws used for fastening the beadboard to the table in the LSAM during printing of the curved wedge.

Figure 156 shows a qualitative comparison between the temperature field captured with the thermal camera (left) and the temperature field predicted in the process simulations (right) after printing 20 layers, 40 layers, and 60 layers. Further, the scales in both temperature fields are in the same temperature range to be able to compare side-to-side the experimental and predicted temperature fields. In general, a close correspondence between the temperature fields characterized experimentally and predicted through the EDAM process simulations is observed.

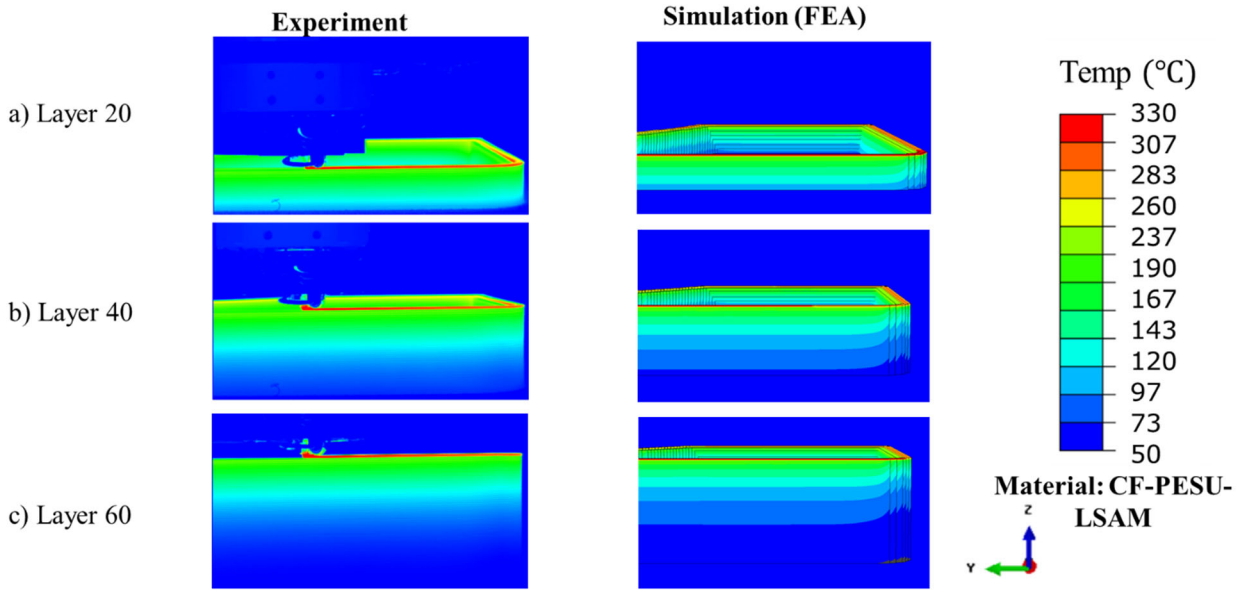

Figure 156. Validation of temperature fields characterized experimentally (left) and predicted (right) in the EDAM process simulation. A) Temperature field at layer 10. B) Temperature field at layer 40. C) Temperature field at layer 60.

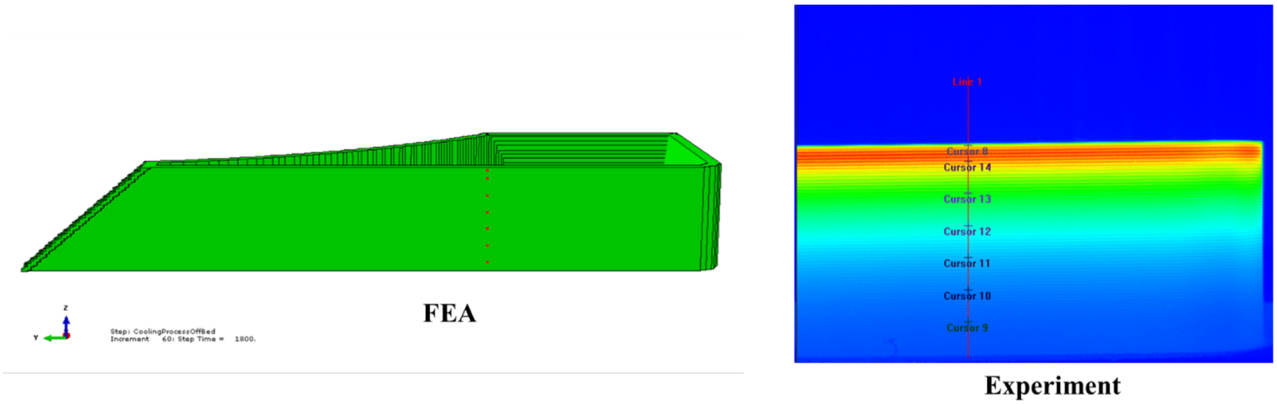

Figure 157. Layer locations in the curved wedge used for extracting time-temperature history.

Figure 158 compares the experimental and predicted time temperature history of the eight layer locations illustrated in Figure 157. The predictions of the transient temperature evolution are in good agreement with the experimental measurements, thereby demonstrating that the relevant heat transfer mechanisms are captured in the EDAM process simulation. The plot of the transient temperature evolution shows the same behavior as the CF-PPS and CF-PSU.

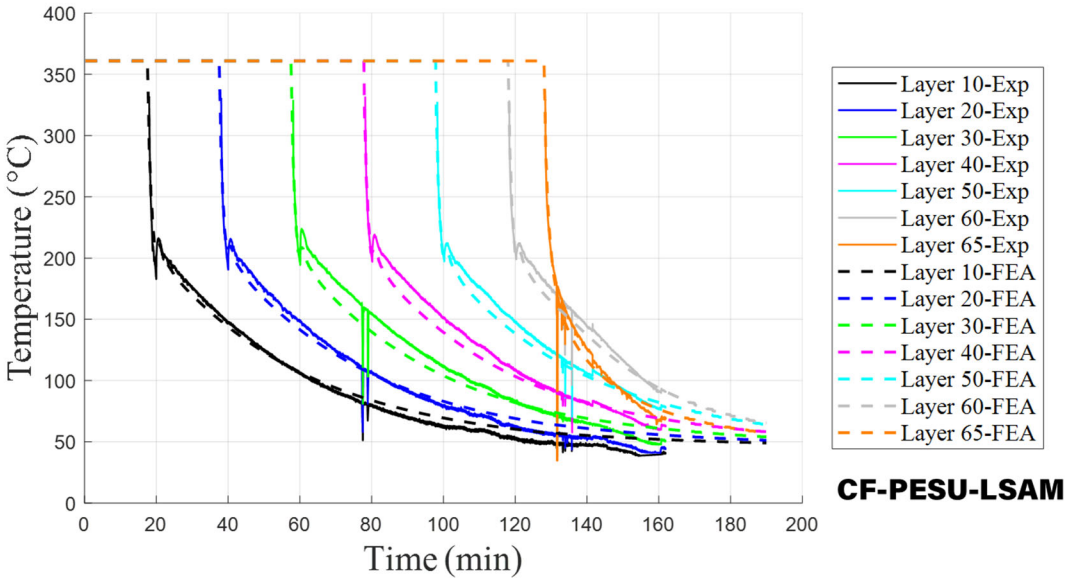

Figure 158. Comparison of time-temperature history measured experimentally and predicted.

The deformation of the curved wedge throughout the printing process and after cooling was also predicted in the process simulation. The curved wedge was initially bonded to the pellets on the beadboard's surface. However, the contact can fail due to the stresses resulting from constraining

the material shrinkage and the thermal stresses developed during the printing process of the part, thereby allowing the part to freely deform in the regions where the contact fails. Figure 159 shows the evolution of the displacement in the layer stacking direction (3-direction) at different instants of the printing process of the curved wedge.

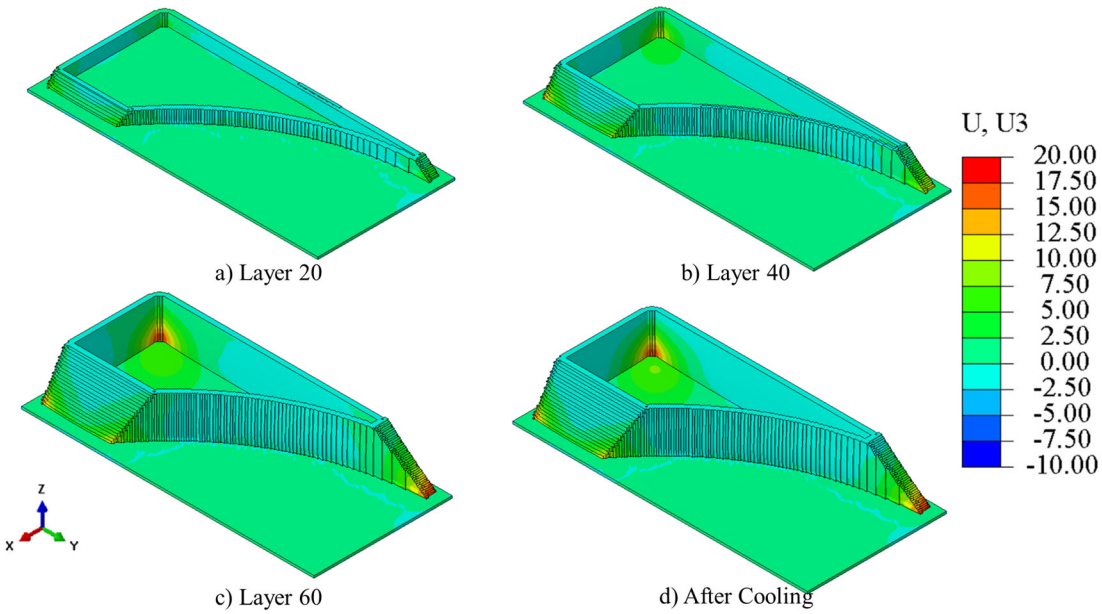

Figure 159. Displacement in the layer stacking direction (3-direction) predicted for the curved wedge printed with CF-PESU. A) After printing 20 layers, b) After printing 40 layers, c) After printing 60 layers, d) After cooled to room temperature while attached to the beadboard.

To validate the predictions for deformation, a deviation analysis was carried out for the top surface of the curved wedge. The deformed shape predicted through the process simulations was extracted at the top surface of the curved wedge and imported into the software Geomagic Wrap©. Figure 160 shows the deviation of the shape predicted through the process simulation with respect to the experimental measurement. The deviation is computed as the normal distance between a point in the predicted shape to the reference shape. The deviations between the two shapes are well within $\pm$3 mm.

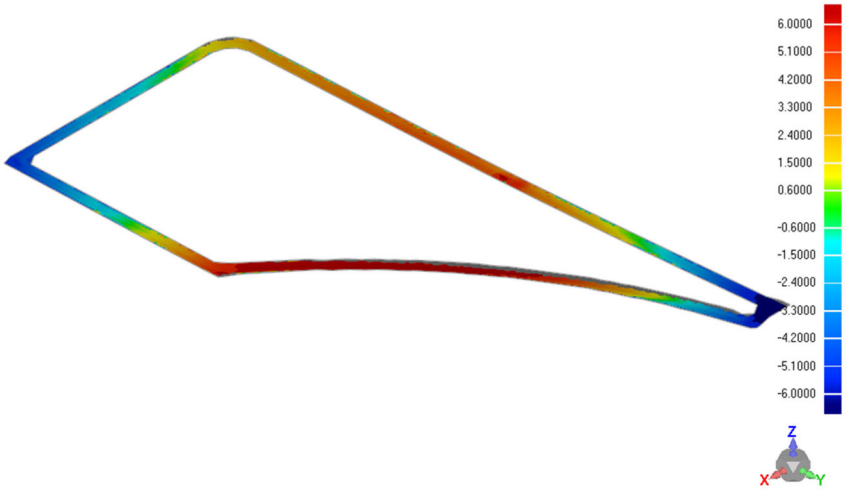

Figure 160. Deviation between the shape measured experimentally and predicted through the process simulation for the top surface of the curved wedge printed with CF-PESU after removal from the beadboard.

6. BENEFITS ASSESSMENT

The adoption of this technology in commercial large-scale EDAM production processes would dramatically reduce the costs associated with producing articles by that process. Many thousands of dollars in materials, energy, and machine time could be saved by utilizing this technology to develop articles rather than iterative printings to arrive at the optimal or correct design. The avoidance of a single failed print has the possibility of saving 10s of thousands of dollars considering that machine time costs are in the hundreds of dollars per hour and material costs are in the $5-$25/lb. range.

7. COMMERCIALIZATION

The developed technology will be promoted to industrial large format EDAM users. Furthermore, the materials used in this program are commercially available. The simulation tools used in this program can be access in a pay per project business model as well as through the Composites Additive Manufacturing and Simulation (CAMS) Consortium. The CAMS consortium provides access to ADDITIVE3D© through a web application that simplifies the process for setting up and conducting an additive manufacturing simulation. The material cards generated in this program enable simulating the printing process for the three materials systems considered, thereby mitigating the empirical process of designing a print strategy or printing process that will produce the desired shape.

8. ACCOMPLISHMENTS

Three material cards were successfully characterized during this program. A non-thesis masters student was supported under this program.

9. CONCLUSIONS

Digital material cards for simulating the EDAM process with three different material formulations were characterized in this program. The material systems considered were PPS reinforced with 50% by weight of carbon fiber, PSU reinforced with 25% by weight of carbon fiber, and PESU reinforced with 25% by weight of carbon fiber. Characterizing these material cards involved extensive experimental and virtual characterization of the printed materials.

To validate the digital material cards, simulations of the printing process were carried out for two geometries that are susceptible to deform: a plate with an antisymmetric print sequence and a

curvilinear shape called curved wedge. Simulation predictions were compared against measurements carried out during and after the printing process carried out in the CAMRI and LSAM systems. Predictions for temperature, degree of crystallinity and deformation was carried out for the three material systems and the two geometries. Predictions for temperature were in great correlation with the experimental measurements for the two geometries printed with the three-material system. The crystallinity level was verified for the only semi-crystalline polymer, CF-PPS. The predictions for part deformation were in good agreement with the experimental measurements. In the best-case, predictions were within 8% of the maximum displacement observed in the 3-direction whereas predictions were within 14% for the worst-case.

The generated material cards enable simulation predictions that can save tens of thousands of dollars in material, machine, and operator's time by anticipating problems related to excessive distortion or stresses developed during the printing process of a part. Hence, this work contributes to enhance the confidence on the EDAM process and materials, and thus to augment its adoption in wider range of applications.

10. RECOMMENDATIONS

Future research work should focus on refining the characterization of the interaction of the printed material with the beadboard substrate as well as on investigating virtually and experimentally the performance of printed components. It should be also recognized that enabling the simulation technology at the fingerprints of the AM users is paramount to increase the confidence on this technology and thus its adoption in a wider range of industries.

11. REFERENCES

[1] Barocio E, Brenken B, Favaloro A, Bogdanor M, Pipes RB. Extrusion Deposition Additive Manufacturing with Fiber-Reinforced Thermoplastic Polymers. In: Friedrich K, Walter R, editors. Struct. Prop. Addit. Manuf. Polym. Components. 1st ed., Woodhead Publishing; 2020, p. 450.

[2] Brenken B, Barocio E, Favaloro A, Kunc V, Pipes RB. Development and validation of extrusion deposition additive manufacturing process simulations. Addit Manuf 2019;25. https://doi.org/10.1016/j.addma.2018.10.041.

[3] Barocio E. Fusion Bonding of Fiber Reinforced Semi-Crystalline Polymers in Extrusion Deposition Additive Manufacturing. Ph.D. Dissertation - Purdue University, 2018.

[4] Thermwood. Thermwood LSAM Additive Printer Brochure. LSAM Addit Print Broch - 82021 2021:4. https://www.thermwood.com/brochures/LSAM_AP_HR.pdf.

[5] Yan J, Demirci E, Ganesan A, Gleadall A. Extrusion Width Critically Affects Fibre Orientation in Short Fibre Reinforced Material Extrusion Additive Manufacturing. Addit Manuf 2021:102496. https://doi.org/10.1016/j.addma.2021.102496.

[6] Wedgewood A, Pibulchinda P, Barocio Vaca E, Hill C, Bogdanor MJ. Materials Development and Advanced Process Simulation for Additive Manufacturing with Fiber-Reinforced Thermoplastics. IACMI The Composite Institute; 2021.

[7] Brenken B. Extrusion Deposition Additive Manufacturing of Fiber Reinforced Semi-crystalline Polymers. Ph.D. Dissertation - Purdue University, 2017.

[8] Pibulchinda P, Barocio E, Pipes RB. Influence of Fiber Orientation on Deformation of Additive Manufactured Composites. Addit Manuf 2021:102483. https://doi.org/10.1016/j.addma.2021.102483.

[9] Brenken B, Favaloro A, Barocio E, Kunc V, Pipes RB. Thermoviscoelasticity in extrusion deposition additive manufacturing process simulations. 32nd Tech. Conf. Am. Soc. Compos. 2017, vol. 1, 2017.

[10] By T, Mechanical D. Standard Test Method for Glass Transition Temperature (DMA Tg) of Polymer Matrix Composites by Dynamic Mechanical Analysis (DMA) 1 2012;i:1–14. https://doi.org/10.1520/D7028-07E01.2.

[11] Wolf HJ. Screw plasticating of discontinuous fiber filled thermoplastic: Mechanisms and prevention of fiber attrition. Polym Compos 1994;15:375–83. https://doi.org/10.1002/pc.750150508.

[12] ASTM. D638 Standard Test Method for Tensile Properties of Plastics. ASTM Int 2016;82:1–15. https://doi.org/10.1520/D0638-14.1.

[13] Method B. ASTM D5379 Standard Test Method for Shear Properties of Composite Materials by the V-Notched. Annu B ASTM Stand 2005:1–13. https://doi.org/10.1520/D5379.

[14] Piorkowska E, Rutledge GC. Handbook of polymer crystallization. John Wiley & Sons;

2013.

[15] Hiemenz PC, Lodge TP. Polymer chemistry. CRC press; 2007.

[16] Velisaris CN, Seferis JC. Crystallization kinetics of polyetheretherketone (peek) matrices. Polym Eng Sci 1986;26:1574–81. https://doi.org/10.1002/pen.760262208.

[17] Young RJ, Lovell PA. Introduction to polymers. CRC press; 2011.

[18] Greco A, Maffezzoli A. Statistical and kinetic approaches for linear low-density polyethylene melting modeling. J Appl Polym Sci 2003;89:289–95. https://doi.org/10.1002/app.12079.

[19] Brinson HF, Brinson LC. Polymer engineering science and viscoelasticity: An introduction, Second edition. 2015. https://doi.org/10.1007/978-1-4899-7485-3.

[20] Marques SPC, Creus GJ. Computational viscoelasticity. SpringerBriefs Appl Sci Technol 2012:iv–v. https://doi.org/10.1007/978-3-642-25311-9.

[21] Fan B, Kazmer DO. Low-temperature modeling of the time-temperature shift factor for polycarbonate. Adv Polym Technol 2005;24:278–87. https://doi.org/https://doi.org/10.1002/adv.20049.

[22] Schapery RA. A method of viscoelastic stress analysis using elastic solutions. J Franklin Inst 1965;279:268–89. https://doi.org/https://doi.org/10.1016/0016-0032(65)90339-X.

[23] Standard A. E1269, 2005,"Standard Test Method for Determining Specific Heat Capacity by Differential Scanning Calorimetry," ASTM International, West Conshohocken, PA n.d.

[24] ASTM. Standard test method for thermal diffusivity of solids by the flash method (E1461-01). Am Soc Test Mater 2001;14:1–13. https://doi.org/10.1520/E1461-13.2.

[25] King TR, Blackketter DM, Walrath DE, Adams DF. Micromechanics Prediction of the Shear Strength of Carbon Fiber/Epoxy Matrix Composites: The Influence of the Matrix and Interface Strengths. J Compos Mater 1992;26:558–73. https://doi.org/10.1177/002199839202600406.

[26] Ramirez MA. In-silico Tensile Testing of Additively Manufactured Short Fiber Composite. Master Thesis - Purdue University, 2018.

[27] Susnjara K, Vaal S. Methods of securing an initial layer during additive manufacturing of thermoplastic material 2020.

[28] Simulia User Assistance 2019. Dassault Syst 2019. http://help.3ds.com/HelpProductsDS.aspx.

[29] Barocio E, Thomas AJ, Pipes RB. Virtual Investigation of Residual Part Deformation Due to Build Plate Support Characteristics in Material Extrusion Additive Manufacturing. CAMX 2020 – Compos. Adv. Mater. Expo, VIRTUAL EXPERIENCE: CAMX 2020; 2020.

[30] Ross RJ. Wood handbook: wood as an engineering material. USDA For Serv For Prod Lab Gen Tech Rep FPL-GTR-190, 2010 509 p 1 V 2010;190.